

**CHARACTERIZATION AND  
APPLICATION OF PHTHALOCYANINE-  
MAGNETIC NANOPARTICLE  
CONJUGATES ANCHORED TO  
ELECTROSPUN POLYAMIDE  
NANOFIBERS**

---

**A thesis submitted in fulfilment of the requirements**

**for the degree of**

**MASTER OF SCIENCE**

**Of**

**RHODES UNIVERSITY**

**By**

**Mpho Ledwaba**

**February 2014**

# **Dedication**

**To my parents:**

**Priscilla and Makgalemele Ledwaba**

**My Siblings:**

**Lerato, Percy and Katlego**

**My nieces and nephew:**

**Makopoli, Tshegofatso and Medupi**

## Acknowledgements

To He who was, is, and is to come...The omniscient and omnipotent God. With You all things are possible and without you none of this would have been possible. I thank you for the courage, the strength, wisdom and persistence you gave me throughout the duration of this degree. All glory and praise is due to You.

I was honoured and privileged enough to have Dr Edith Antunes as my supervisor, and honestly, words are not sufficient enough to express the intensity of my gratitude towards her. The skills and knowledge she has transferred to me, I shall forever cherish. Her words of encouragement and support pulled me through every storm and obstacle. She is a true token of "Ubuntu".

To a woman who makes me proud to say I am a black woman in science, Professor Nyokong. I am humbled by her strength and dedication, she is truly a great inspiration to me and I was privilege to be part of her research group. For the opportunities she made available to me to travel to Belgium and attend conferences enlarging my science knowledge, I say Thank you. "You strike a woman, you strike a rock"

Financial Support from National Research Foundation (NRF) of South Africa is highly appreciated and acknowledged.

My S22 colleagues, you made working enjoyable. You guys are the future. Charmain ngiyakuhlonipha mngani!!!


My parents have been a great system of support and encouragement, they taught me not to give up but to always hope for the best. I am blessed to be your daughter (your gift).

To my twins from another mother Nomasonto and Lwazikazi, I walked not looking back but forward because that is where you always led me. I look up to you guys and I shall forever cherish the lessons you taught me. The middle child loves you Big time.

Legadime, Thank you for embarking on this journey with me.

Big sis, Big bro and lil bro: this is to you, thanks for the hands that held me high.

The Ronins and the Bunny, you were last minutes encouragement and I appreciate your support...mAziwe ke!!!

KGM  #nuffsaid

My computer lenders Lwando and Jumbe, thank you for meeting me at my point of need.

## Abstract

This work presents the syntheses, photophysical and photochemical characterization of zinc tetracarboxyphenoxy phthalocyanine (ZnTCPPc, **3**) and its gadolinium oxide nanoparticle conjugate (**4**). By means of spectroscopic and microscopic characterization, the conjugation of the ZnTCPPc to the silica coated gadolinium oxide nanoparticles (Si-Gd<sub>2</sub>O<sub>3</sub> NPs, **2**) through an amide bond was confirmed. The thermal stability, morphology, nanoparticle sizes and their conjugates with the Pc were studied using ThermoGravimetric Analysis (TGA), Fourier Transform Infrared spectroscopy (FTIR), Transmission Electron Microscopy (TEM) and powder X-ray diffractometry (XRD). Conjugation of ZnTCPPc to the magnetic nanoparticles, proved to have a negligible effect on the photophysical parameters of the phthalocyanine, where a slight decrease in fluorescence and triplet quantum yields and lifetimes was observed. The singlet oxygen quantum yield, however, increased slightly upon conjugation, suggesting that the overall efficiency of the ZnTCPPc as a photosensitizer had improved. Physical mixing of the ZnTCPPc and the silica-coated gadolinium nanoparticles also showed an improvement in the singlet oxygen quantum yield and triplet lifetime, also showing an enhanced efficiency for the photosensitizer and therefore photocatalysis.

ZnTCPPc (**3**) alone and the Pc-gadolinium oxide nanoparticle conjugate (**4**) were therefore electrospun into nanofibers to create a solid support. The fibers were characterized and their diameter sizes and composition was studied confirming the incorporation of the phthalocyanine and gadolinium oxide nanoparticle. Increased singlet oxygen generation resulted in increased Photodegradation of the environmental pollutant Orange G and the fibers were found to be more efficient as photocatalysts compared to the photosensitizer in solution. The nanomaterial may therefore be applied to the photodegradation of Orange G.

# Contents

<b>Title</b>	
<b>Dedication</b>	i
<b>Acknowledgements</b>	ii
<b>Abstract</b>	iv
<b>Table of Contents</b>	v
<b>List of Abbreviations</b>	x
<b>List of Symbols</b>	xii
<b>List of Figures</b>	xiv
<b>List of Schemes</b>	xviii
<b>List of Tables</b>	xix
<b>1. Introduction</b>	
1.1. Photodynamic Therapy (PDT)	2
1.1.1. General overview of photodynamic therapy	2
1.1.2. Photochemistry and photophysics of PDT	3
1.1.2.1. Light delivery	5
1.1.3. Sensitizers in use for PDT	5
1.2. Phthalocyanines	8
1.2.1. Overview of phthalocyanine chemistry	8
1.2.2. Structure of phthalocyanines	10
1.2.3. Synthesis of phthalocyanines	11

1.2.3.1.	Synthesis via tetramerization of a single precursor	11
1.2.4.	Photophysical and photochemical properties of phthalocyanines	13
1.2.4.1.	UV- vis absorption spectra of phthalocyanines	15
1.2.4.2.	Fluorescence quantum yields and lifetimes	16
1.2.4.3.	Triplet quantum yield and lifetimes	17
1.2.4.4.	Singlet oxygen quantum yield	19
1.3.	Hyperthermia	21
1.4.	Magnetic Resonance Imaging (MRI)	23
1.4.1.	Principles of MRI	23
1.4.2.	Classes of Contrast Agents	23
1.4.2.1.	The longitudinal relaxation ( $T_1$ ) agents	24
1.4.2.2.	Gadolinium-based contrast agents	25
1.5	Magnetic nanoparticles	26
1.5.1	Applications of phthalocyanines with magnetic nanoparticles	26
1.5.2	Properties of Gadolinium Nanoparticles	27
1.5.3	Synthesis of Gadolinium contrast agents and nanoparticles	29
1.5.4	Characterisation and applications of Gadolinium Nanoparticles	30
1.6	Electrospinning	32
1.6.1	Electrospinning process parameters	33
1.6.2	Characterization of electrospun fibers	34
1.6.3	Applications of electrospinning	35
1.7	Background on environmental pollutants used in this work	35
1.7.1	Background on Azo dyes	36
1.8	Summary of the aims of this thesis	37
1.9	References	38
<b>2</b>	<b>Experimental</b>	
2.1	Solvents and reagents	50
2.2	Instrumentation	50





2.3 Methods	54
2.3.1 Fluorescence quantum yields and lifetimes	54
2.3.2 Triplet quantum yields and lifetimes	55
2.3.3 Singlet oxygen quantum yields	56
2.4 Synthesis	58
2.4.1 Synthesis of bare gadolinium oxide nanoparticles	58
2.4.2 Silica-coated gadolinium oxide nanoparticles	58
2.4.3 Synthesis of zinc tetracarboxyphenoxy phthalocyanine	59
2.4.4 Synthesis of ZnTCPPc-Si-Gd <sub>2</sub> O <sub>3</sub> conjugate	59
2.4.5 Synthesis of ZnTCPPc-Si-Gd <sub>2</sub> O <sub>3</sub> mix	59
2.5 Electrospinning methods	60
2.5.1 Polyamide fibers	60
2.5.2 Functionized ZnTCPPc conjugate and mixed nanofiber Preparations	61
2.6 References	62

## RESULTS and DISCUSSION

### 3 Synthesis and spectroscopic characterisation

3.1 Synthesis and characterisation of gadolinium oxide nanoparticles	67
3.1.1 Transmission electron spectroscopy	68
3.1.2 Fourier transform infrared spectroscopy	69
3.1.3 Thermogravimetric analysis	71
3.1.4 X-Ray diffraction	72
3.1.5 X-ray photoelectron spectroscopy	74
3.1.6 Electron paramagnetic resonance	77
3.2 Synthesis and characterization of phthalocyanine-MNP conjugates	79
3.2.1 Synthesis and characterization of zinc tetracarboxyphenoxy Phthalocyanine	79
3.2.2 Assembly of phthalocyanine –MNP conjugates	81
3.2.2.1 Synthesis and characterization of the Pc-MNP conjugate	82

3.2.2.2	Transmission electron microscopy	83
3.2.2.3	Fourier transform-infrared	84
3.2.2.4	Thermogravimetric analysis	86
3.2.2.5	X-ray diffraction	87
3.2.2.6	Electron paramagnetic resonance	88
3.3	Photophysical studies	89
3.3.1	Fluorescence quantum yields and lifetimes	89
3.3.2	Triplet quantum yields and lifetimes	93
3.3.3	Singlet oxygen quantum yields	94
3.4	References	97

## 4 Electrospun nanofibers

4.1	Influence of electrospinning conditions on morphology of polymer fiber zinc tetraphenoxycarboxyphthalocyanine	100
4.1.1	Effect of polymer viscosity and conductivity on fiber morphology	100
4.1.2	Effect of polymer concentration on fiber morphology	103
4.1.3	Effect of solvent ratios in polymer solutions	103
4.2	Characterization of electrospun polymer fibers functionalized with the ZnTPCPC and their photochemical behaviour	
	105 4.2.1	Microscopic characterisation
	106 4.2.2	Spectroscopic characterization
	109 4.2.2.1	Energy dispersive X-ray spectroscopy
		109
4.3	Photochemical behaviour of the Pc functionalized fibers: singlet oxygen generating ability	110
4.4	References	114

## 5 Photodegradation studies

5.1	Introduction	116
5.2	Photodegradation of orange G	116



5.2.1 Spectroscopic characterization	116
5.2.2 Kinetic studies for the degradation of orange G	118
5.3 Conclusion	121
5.4 References	122
<b>6 General Conclusions</b>	<b>124</b>

## List of Abbreviations

A	Absorbance
AOP	Advanced Oxidation Processes
ADMA	Anthracene-9, 10-bis-methylmalonate
APTES	3-aminopropyltriethoxysilane
CT	Charge-transfer transitions
DMSO	Dimethylsulphoxide
DCC	N,N'-dicyclohexylcarbodiimide
EDX	Energy dispersive x-ray spectroscopy
ET	Energy transfer
EtOH	Ethanol
F	Fluorescence
Gd <sub>2</sub> O <sub>3</sub> NP	Gadolinium oxide nanoparticle
H <sub>2</sub> Pc	Metal-free phthalocyanine
HOMO	Highest occupied molecular orbital
IC	Internal conversion
IR	Infrared
ISC	Intersystem crossing
L-H	Langmuir-Hinshelwood
LMCT	Ligand-to-metal charge transfer
LUMO	Lowest unoccupied molecular orbital
MLCT	Metal-to-ligand charge transfer
MPc	Metallophthalocyanine
MTCPc	Metallotetracarboxy phthalocyanine
NaOH	Sodium hydroxide
NHS	N-hydroxysuccinimide
OG	Orange-G

PA-6	Polyamide-6
Pc	Phthalocyanine
PDT	Photodynamic therapy
PS	Photosensitizer
RH	Relative humidity
ROS	Reactive oxygen species
SEM	Scanning electron microscopy
TCSPC	Time-correlated single photon counting
TEM	Transmission electron microscopy
TGA	Thermogravimetric analysis
UV/Vis	Ultraviolet/visible
XRD	X-ray diffractometry
ZnTCPPc	zinc tetraphenoxycarboxy phthalocyanine

## List of Symbols

$\Delta A$	Change in absorbance following laser pulse
AA	Acetic acid
$\Delta AS$	Change in singlet state absorbance
$\Delta AT$	Change in triplet state absorbance
I	Intensity of light
I <sub>abs</sub>	Intensity of light absorbed
F	Fluorescence intensity
FA	Formic acid
A	Non-peripheral position
$\beta$	Peripheral position
$\epsilon$	Molar extinction coefficient
$\epsilon_S$	Singlet state extinction coefficient
$\epsilon_T$	Triplet state extinction coefficient
$\theta$	angle
$\lambda$	wavelength
$\lambda_{emi}$	wavelength of emission spectrum maximum
$\lambda_{exci}$	wavelength of excitation spectrum maximum
h $\nu$	Light
n	Refractive index
$\Phi_{\Delta}$	Singlet oxygen quantum yield
$\Phi_F$	Fluorescence quantum yield
$\Phi_T$	Triplet state quantum yield
$\tau_{\Delta}$	Singlet oxygen lifetime
$\tau_F$	Fluorescence lifetime
$\tau_T$	Triplet state lifetime
$\chi^2$	Reduced Chi-squared statistic

$^1\text{O}_2$	Singlet oxygen
$^3\text{O}_2$	Triplet molecular oxygen
$\text{O}_2$	Ground state molecular oxygen
$\text{S}_0$	Ground singlet state
$\text{S}_1$	Excited singlet state
$\text{T}_1$	First excited triplet state
$\text{T}_2$	Second excited triplet state
$k$	Apparent rate constant
$K_{\text{obs}}$	Observed rate constant



## List of Figures

<b>Figure 1.1:</b> PDT therapeutic process in the human body	<b>3</b>
<b>Figure 1.2:</b> Photophysical and photochemical reaction mechanisms in PDT	<b>4</b>
<b>Figure 1.3:</b> Structures of some Photosensitizers	<b>7</b>
<b>Figure 1.4:</b> Structure of the phthalocyanine molecule and sites for substitution	<b>9</b>
<b>Figure 1.5:</b> Jablonski diagram illustrating the electronic states of a molecule and the transitions taking place between the excited states and the ground state	<b>14</b>
<b>Figure 1.6:</b> A typical absorption spectrum of a ZnPc in HPLC grade DMF solvent	<b>15</b>
<b>Figure 1.7:</b> shows a typical fluorescence decay curve for a Pc	<b>17</b>
<b>Figure 1.8:</b> A Typical triplet decay curve obtained for a Pc in DMSO	<b>18</b>
<b>Figure 1.9:</b> Typical singlet oxygen decay signal at 1270 nm for an MPC in DMSO	<b>20</b>
<b>Figure 1.10:</b> A schematic representation of some of the unique advantages magnetic nanomaterials offer in hyperthermia-based therapy and controlled drug delivery	<b>22</b>
<b>Figure 1.11:</b> Graph showing the function of MNPs in the perturbation of the magnetic relaxation processes of the proton	<b>26</b>
<b>Figure 1.12:</b> Crystal structure of the gadolinium nanoparticle	<b>29</b>
<b>Figure 1.13:</b> Schematic drawing of electrospinning technique setup	<b>34</b>
<b>Figure 1.14:</b> Photodegradation of the orange G dye	<b>36</b>
<b>Figure 3.1:</b> TEM image of (i) Gd <sub>2</sub> O <sub>3</sub> NPs (1), (ii) Si-Gd <sub>2</sub> O <sub>3</sub> NPs (2) and (iii) ZnTCPPc-Gd <sub>2</sub> O <sub>3</sub> NPs-conjugate (4)	<b>69</b>
<b>Figure 3.2:</b> FTIR spectra of (A) (i) PEG utilized in the synthesis and the synthesized nanoparticles (ii) Gd <sub>2</sub> O <sub>3</sub> NPs (1) and (ii) Si-Gd <sub>2</sub> O <sub>3</sub> NPs (2)	<b>70</b>

**Figure 3.3:** TGA profiles of (i) Gd(NO<sub>3</sub>)<sub>3</sub>, (ii) PEG, (iii) Gd<sub>2</sub>O<sub>3</sub>NPs (1) and (iv) Si-Gd<sub>2</sub>O<sub>3</sub>NPs (2) **72**

**Figure 3.4:** XRD spectra of (i) Gd(NO<sub>3</sub>)<sub>3</sub>, salt (ii) bare Gd<sub>2</sub>O<sub>3</sub> NPs (bare, 1) and (iii) Si-Gd<sub>2</sub>O<sub>3</sub> NPs (2) **73**

**Figure 3.5:** Wide scan XPS spectra (A) of (i) Gd<sub>2</sub>O<sub>3</sub> NPs (1) and (ii) SiGd<sub>2</sub>O<sub>3</sub> NPs (2). High resolution spectra of: (B) Gd 4d region for (i) Gd(NO<sub>3</sub>)<sub>3</sub> salt and (ii) Gd<sub>2</sub>O<sub>3</sub> NP; and (C) O 1s region for (i) Gd(NO<sub>3</sub>)<sub>3</sub> salt, (ii) Gd<sub>2</sub>O<sub>3</sub> NPs, and (iii) SiGd<sub>2</sub>O<sub>3</sub> NPs. Deconvolution of the O 1s high resolution spectra is given in graphs D – F where: (D) is the Gd(NO<sub>3</sub>)<sub>3</sub> salt (i), (E) is the bare Gd<sub>2</sub>O<sub>3</sub> NP (ii), and (F) is the Si-Gd<sub>2</sub>O<sub>3</sub> NP (iii). **76**

**Figure 3.6:** EPR spectra acquired in the solid state at room temperature for (i) Gd(NO<sub>3</sub>)<sub>3</sub>, (ii) Gd<sub>2</sub>O<sub>3</sub> NPs (1) and (iii) Si-Gd<sub>2</sub>O<sub>3</sub> NPs (2), . Inset: Zoomed in section to show the spectra obtained for the NPs **78**

**Figure 3.7:** UV-vis spectra of ZnTCPPc in DMSO. The Figure illustrates the typical monomeric behaviour of the Pc with a Q-band maximum at 678 nm **80**

**Figure 3.8** Normalized absorption, emission and excitation spectra of ZnTCPPc in DMSO **81**

**Figure 3.9:** UV/vis spectra obtained for the samples in DMSO: (i) Si-Gd<sub>2</sub>O<sub>3</sub> NPs (2), (ii) ZnTCPPc (3), (iii) ZnTCPPc-SiGd<sub>2</sub>O<sub>3</sub> NP (conj) (4) and (iv) ZnTCPPc-SiGd<sub>2</sub>O<sub>3</sub> NP-mix (5) **83**

**Figure 3.10:** FTIR spectra of the synthesized (A) (i) Si-Gd<sub>2</sub>O<sub>3</sub> NPs (2, (ii) ZnTCPPc (3), (iii) ZnTCPPc-SiGd<sub>2</sub>O<sub>3</sub> NP (4) and (iv) the simple mixture ZnTCPPc-SiGd<sub>2</sub>O<sub>3</sub> NP-mix (5). Graph (B) is zoomed into the region 2000 – 600 cm<sup>-1</sup> to highlight the changes observed between (i) ZnTCPPc (3), (ii) ZnTCPPc-SiGd<sub>2</sub>O<sub>3</sub> NPs (4) and ZnTCPPc-SiGd<sub>2</sub>O<sub>3</sub> NPs-mix (5) **85**

<b>Figure 3.11:</b> TGA profiles of (i) Si-Gd <sub>2</sub> O <sub>3</sub> NP (2), (ii) ZnTCPPc (3) and (iii) ZnTCPPc-Gd <sub>2</sub> O <sub>3</sub> -conjugate (4) at a heating rate of 10 °C/min to 500 °C under a nitrogen atmosphere with a gas flow rate of 120 ml/min	<b>87</b>
<b>Figure 3.12:</b> EPR spectra acquired at room temperature in the solid state for (i) ZnTCPPc (3), (ii) ZnTCPPc-SiGd <sub>2</sub> O <sub>3</sub> NP (conj) (4) and (iii) ZnTCPPc-SiGd <sub>2</sub> O <sub>3</sub> NP (mix) (5). Inset: Zoomed in section (3400 – 3600 G) for the ZnTCPPc (i) and the conjugate (ii)	<b>88</b>
<b>Figure 3.13:</b> Normalized absorption, fluorescence emission and excitation spectra of (A) ZnTCPPc-SiGd <sub>2</sub> O <sub>3</sub> NP (conj) and (B) ZnTCPPc-SiGd <sub>2</sub> O <sub>3</sub> NP(mix) in DMSO	<b>90</b>
<b>Figure 3.14:</b> Fluorescence lifetime decay curves of (i) ZnTCPPc (3) alone, (ii) ZnTCPPc - Gd <sub>2</sub> O <sub>3</sub> NPs conjugate (4) and (iii) the mixture in DMSO. Exc. $\lambda$ = 689 nm	<b>92</b>
<b>Figure 3.15:</b> Triplet decay curve of synthesized complexes in DMSO at 490 nm	<b>94</b>
<b>Figure 3.16:</b> Photodegradation of DPBF in the presence of ZnTCPPc in DMSO	<b>96</b>
<b>Figure 4.1:</b> Plot of the changes in viscosity with increasing polymer concentration for the different polymer grades	<b>101</b>
<b>Figure 4.2:</b> Plots showing the effects of varying the acetic acid: formic acid solvent ratio on the viscosity and conductivity of the different polymer grades: where (A) and (C) are the viscosity and conductivity results obtained for the 1:1 FA:AA solvent system respectively; while (B) and (D) are the viscosity and conductivity results obtained for the 3:1 FA:AA solvent system	<b>104</b>

**Figure 4.3:** Scanning electron micrographs of the electrospun fiber mats obtained from solutions of PA-6-24 (A), PA-6-27 (B), PA-6-32 (C) PA-6-36 (D) in 1:1 FA:AA **107**

**Figure 4.4:** SEM images of the nanofibers mats of A) PA-6/ZnTCPPc, B) PA-6/ZnTCPPc-Si-Gd<sub>2</sub>O<sub>3</sub> NPs-conj (4) and C) PA-6/ZnTCPPc-Si-GdNPs (5,mix) **108**

**Figure 4.5:** EDX spectrum of a) PA-6/Si-Gd<sub>2</sub>O<sub>3</sub> NP (conjugate) b) PA -6/ZnTCPPc c) PA -6/ZnTCPPc -SiGd<sub>2</sub>O<sub>3</sub>NPs (conjugate) and d) PA -6/ ZnTCPPc -SiGd<sub>2</sub>O<sub>3</sub>NPs(mix) nanofibers proving the presence of the gadolinium oxide nanoparticles on the fibre **110**

**Figure 4.6:** UV-vis spectral changes observed upon photolysis of 15 mg of PA-6/ ZnTCPPc-nanofibers in the presence of ADMA in unbuffered water for 15 min of photolysis. Starting ADMA concentration =  $3.9 \times 10^{-5} \text{ mol dm}^{-3}$ , irradiation interval = 5 min **112**

**Figure 5.1** Electronic absorption spectral changes of a  $1.93 \times 10^{-5} \text{ mol L}^{-1}$  Orange G solution during visible light photocatalysis using a 10 mg A) ZnTCPPc , B) ZnTCPPc-Si-GdNP (conjugate) and C) ZnTCPPc-Si-GdNP (mix) nanofiber mat. **118**

**Figure 5.2:** First order kinetics plots for the degradation of OG for: (A) PA-6/ ZnTCPPc (B) PA-6/ ZnTCPPc-MNPs (conjugate) and (C) PA-6/ ZnTCPPc -MNPs (mix), nanofiber as a photocatalysts **119**

## List of Schemes

<b>Scheme 1.1:</b> Synthetic routes to metallophthalocyanines (MPcs) from various precursors	<b>12</b>
<b>Scheme 1.2:</b> Photochemical reactions leading to the decay of singlet oxygen in a solution of photosensitizer (MPc) and quencher (DPBF)	<b>20</b>
<b>Scheme 2.1:</b> Schematic diagram for the TCSPC spectrometer	<b>51</b>
<b>Scheme 2.2:</b> Schematic representation of a laser flash photolysis set-up	<b>55</b>
<b>Scheme 2.3</b> Schematic representation of a photochemical set-up	<b>57</b>
<b>Scheme 3.1:</b> Synthetic route for the preparation of the bare Gd <sub>2</sub> O <sub>3</sub> NPs (1) and the silica-coated Gd <sub>2</sub> O <sub>3</sub> NPs (Si-Gd <sub>2</sub> O <sub>3</sub> NPs, 2)	<b>66</b>
<b>Scheme 3.2:</b> Synthetic route showing the conjugation of the ZnTCPPc (3) to the surface of the silica-coated Gd <sub>2</sub> O <sub>3</sub> NPs via an amide bond	<b>66</b>

## List of Tables

**Table 1.1:** Configuration and magnetic moments of some paramagnetic metal ions **25**

**Table 1.2:** Table of magnetic nanoparticles used in combination with metallophthalocyanines for a various applications

**28**

**Table 3.1:** List of the synthesized or functionalized complexes used in this work **67**

**Table 3.2:** Table showing, the size of the NPs, absorbance, photophysical and photochemical results of the Pc components **93**

**Table 4.1:** The effect of polymer solution concentrations (for the different polyamide grades) on the viscosity and conductivity parameters (solvent used: 50:50 (FA:AA) **102**

**Table 4.2:** The effect of solvent ratio (FA:AA), polymer concentration and molecular weight on the fiber diameter (in  $\mu\text{m}$ ) **105**

**Table 4.3:** The effect of functionalization on singlet oxygen quantum yields. Polymer formed from PA-6 (B 32, 14 wt. %) 3:1 (FA:AA) **113**

**Table 5.1:** The initial rate, rate constant ( $k_{obs}$ ) and half-life ( $t_{1/2}$ ) of various initial concentrations of Orange G using the variously functionalized electrospun fibers. Values in square brackets are for nanocomposites not embedded in fiber. **121**

# **Chapter 1**

## **Introduction**

# Introduction

The assembly of nanocomposites into novel hybrid systems allows for the design of a nanomaterial with attractive multifunctional properties. These novel nanomaterials open up a wide spectrum of technological applications. The hybrid nanomaterial in our case will include phthalocyanines which have been shown to be effective as photosensitizers in photodynamic therapy, and gadolinium oxide nanoparticles which have been found to possess excellent magnetic resonance imaging properties and some success in hyperthermia therapy. In addition, nanoparticles have been used successfully as drug delivery agents in preliminary studies in cancer therapy, while the phthalocyanines as photosensitizers have shown excellent photocatalytic effects.

## 1.1 Photodynamic Therapy

### 1.1.1 General overview of Photodynamic therapy

Photodynamic therapy (PDT) is concerned with the administration of a non-toxic drug or a dye known as a photosensitizer (PS) either systemically, locally or topically into a cancer patient [1, 2]. The use of PDT as a form of cancer therapy is particularly attractive because of its fundamental properties, namely specificity and selectivity [3]. Following administration of the sensitizer and an incubation period, the lesion is illuminated with a long wavelength, visible light (620 – 690 nm), which, in the presence of oxygen, leads to the generation of the cytotoxic singlet oxygen species. The singlet oxygen generated effectively leads to cell death and tissue destruction [4]. PDT is achieved due to the fact that the PS concentrates specifically within the harmful tissue such that when the light is directly focused on the lesion, the reactive oxygen species (ROS) are generated resulting in cellular destruction as shown in figure 1.1. Due to this, PDT has been under intense investigation as an effective treatment for various forms of cancer [5-7].



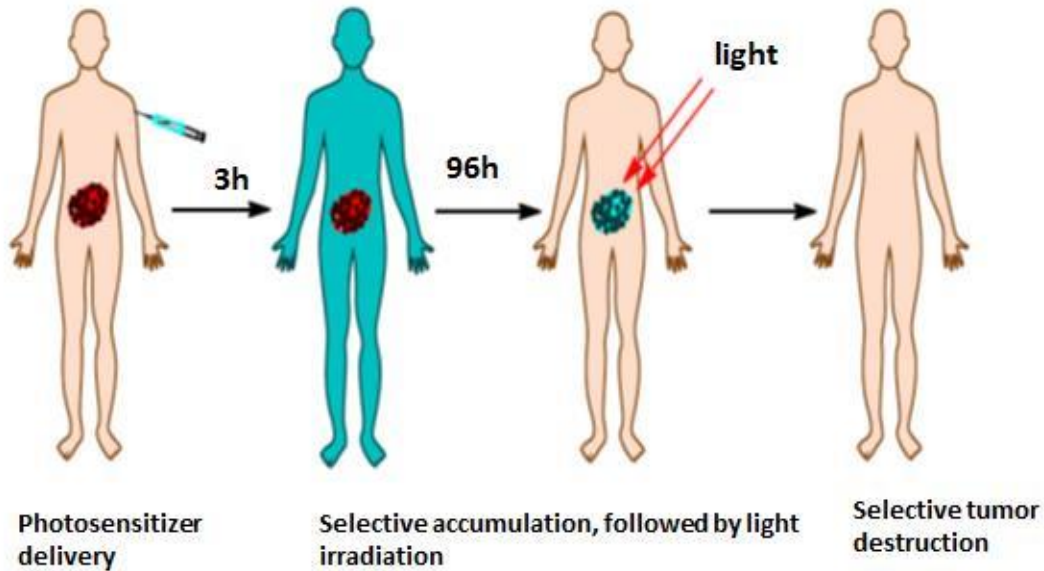


Figure 1.1: PDT therapeutic process in the human body [8].

### 1.1.2 Photochemistry and photophysics of Photodynamic therapy

Two of the most important aspects of PDT involve the processes of light absorption and energy transfer; these are illustrated in Figure 1.2. Generally, a ground state PS comprising two electrons with opposite spins in a low energy molecular orbital (known usually as the singlet state) absorbs light in the form of photons. Upon absorption, one of the electrons is promoted to a higher energy, excited state level, keeping the singlet state spin. This is a **short-lived** state and the energy is lost through the emission of fluorescent light or by internal conversion into heat. The excited singlet state PS may also undergo intersystem crossing, a process whereby the spin of the excited electron inverts, giving rise to a relatively long-lived excited triplet state with electrons in a parallel conformation [9].

This excited, triplet state PS may then undergo two kinds of reactions, i.e. Type 1 and Type 2 reaction mechanisms (Figure 1.2). Firstly, in a Type 1 reaction, the PS reacts directly with a substrate, such as the cell membrane or molecule, where an electron is transferred to form radical anions or cations. These radicals may further react with oxygen, producing reactive oxygen species (ROS) which are responsible for the destruction of harmful tissues. Alternatively, in a Type 2 reaction mechanism, the triplet state PS's excitation energy is transferred to molecular oxygen (itself in a triplet ground state ( $^3\text{O}_2$ )), forming excited singlet state oxygen ( $^1\text{O}_2$ ). Both Type 1 and Type 2 reactions can occur simultaneously, and the ratio between these processes relies upon the nature of PS and the concentrations of substrate and oxygen [10, 11].

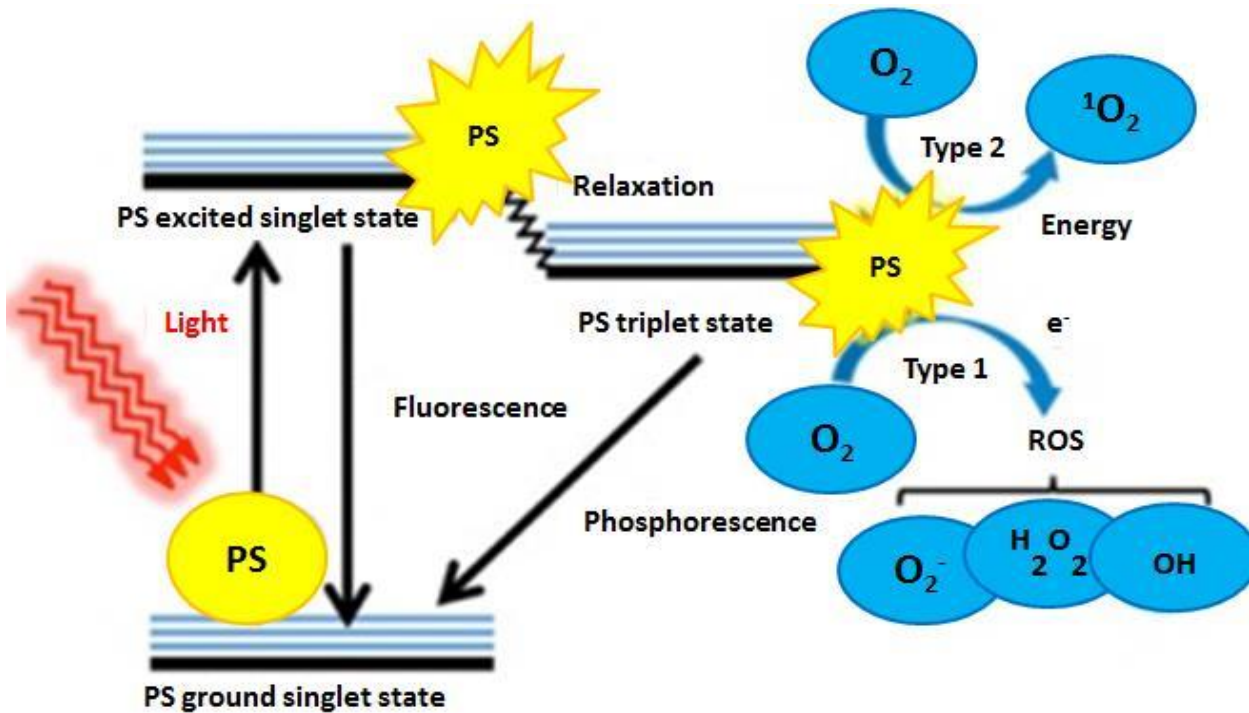


Figure 1.2: Photophysical and photochemical reaction mechanisms in PDT.

### 1.1.2.1 Light delivery

For successful PDT treatment it is essential to be able to predict the spatial distribution of light within the target tissue and to ensure sufficient light reaches all the diseased tissue. Therefore one needs to understand how light travels through the various bodily tissues and the relative effects of absorption and scattering [11]; the degree of which depends on the nature of the tissue and light wavelength employed.

The fact that most photosensitizers are able to fluoresce, a range of optical imaging and monitoring strategies may be combined into the PDT treatment. An often longer wavelength of light is applied to diseased tissue, allowing for an increased penetration depth with minimal light scattering and maximum PS activation [10]. To generate enough  $^1\text{O}_2$  (and other ROS) to produce a cytotoxic effect, the light source for PDT must possess specific and suitable spectral characteristics that correlate with the maximum absorption wavelength range of the PS employed [12]. One important feature for a photosensitizer during PDT is its ability to possess light absorption at a wavelength range where the surrounding biological tissues are transparent. In order for deep penetration of light to be possible into the body the photosensitizer should absorb in the red (visible) region [13].

### 1.1.3 Sensitizers in use for PDT

The requirements for an ideal sensitizer include properties such as chemical purity, selectivity for tumour cells, chemical and physical stability, a short time interval between administration and maximal accumulation within tumour tissues, activation at selected wavelengths with optimal tissue penetration and a rapid clearance from the body [11]. Many photosensitizers have been tested *in vivo* and *in vitro* in PDT experiments, though only a few have revealed ideal properties for this therapy and thus many recent studies have shifted their focus to the development and

efficacy of new, efficient photosensitizers [7]. The four main classes of photosensitizers are porphyrin derivatives, chlorins, phthalocyanines and porphycenes, all of which show different photochemical and photophysical properties in terms of their mechanisms of action and activation of light [14].

A hematoporphyrin derivative, known as Photofrin, was the first PS to be studied in detail. However, since Photofrin is a mixture of isomers, elucidation of its chemical structure and components was found to be highly challenging. The majority of PSs used, both clinically and experimentally, are the aromatic tetrapyrrole derivatives found in many naturally occurring pigments such as heme, chlorophyll and bacteriochlorophyll. Naturally occurring porphyrins are fully conjugated tetrapyrroles and they vary in the number and type of side chain. Porphyrins have a long wavelength absorption band in the region of 630 nm [12, 15].

Another class of potential PS includes the synthetic, highly conjugated pyrrolic ring systems such as the texaphyrins [16], porphycenes [17] and sapphyrins [18]. Some of these compounds have either been approved or are undergoing clinical or advanced pre-clinical testing and are given in Figure 1.3. Another class of widely studied PSs are phthalocyanines (Pcs), the focus of this thesis, which will be discussed later [14].

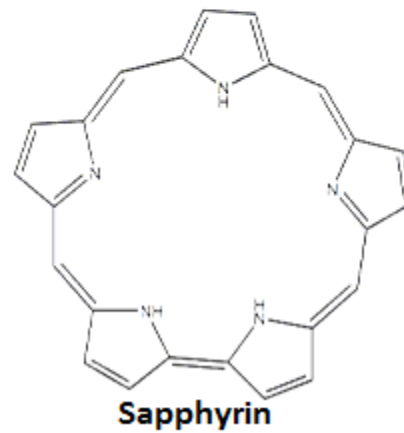
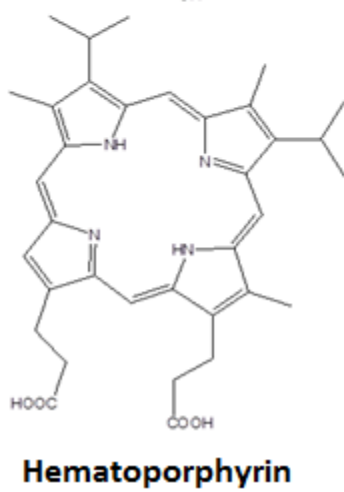
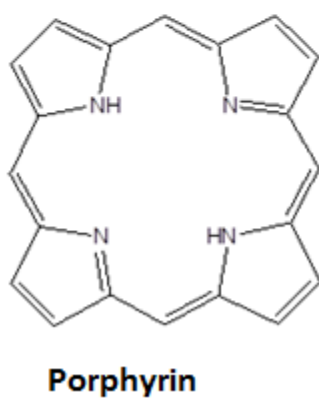
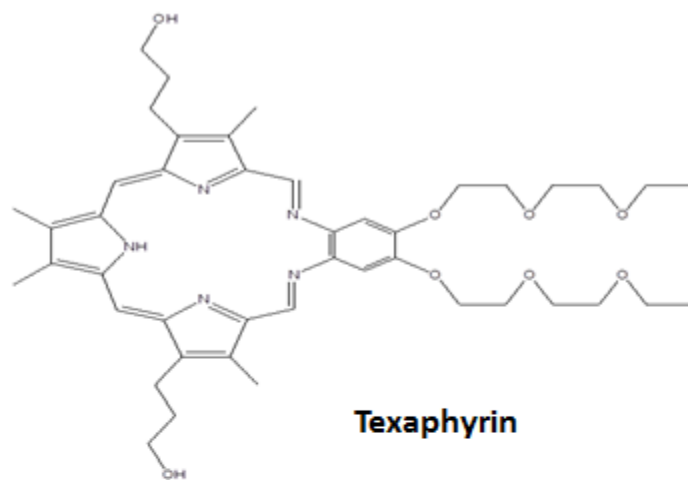
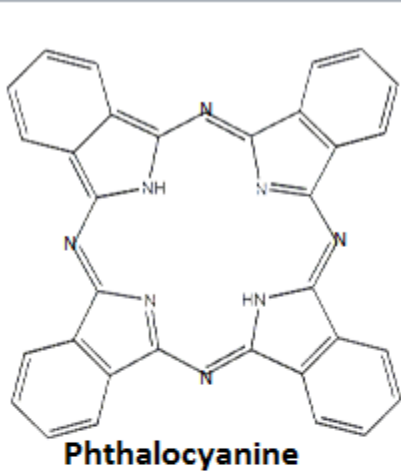


**Figure 1.3: Structures of some Photosensitizers**

## 1.2 Phthalocyanines

### 1.2.1 Overview of phthalocyanine chemistry

Phthalocyanines (Pcs) are a class of synthetic tetrapyrrolic compounds, similar in structure to the naturally occurring porphyrin [19]. The structural differences between the Pc and porphyrin macrocycles are the four extended benzo subunits and four nitrogen atoms at the *meso* position on the macrocycle of Pcs (Figure 1.4); hence Pcs are often referred to as tetra-benzotetraazaporphyrins [20]. The Pcs are a unique set of organic pigments that provide stable and strongly chromatic blue and green colours. Pcs show a strong absorbance at longer wavelengths as compared to porphyrins and they often have improved photophysical and photochemical properties over porphyrins [21].

The first Pc reported was as a dark blue insoluble by-product in the preparation of *o*-cyanobenzamide from phthalimide and acetic acid by Braun and Tcherniac in 1907 [22]. Von der Weid and Diesbach of Fribourg University, twenty years later, unknowingly isolated a Pc, a stable blue compound, in reacting *o*-dibromobenzene with copper cyanide in refluxing pyridine [23].

Since their discovery (in the 1900s), Pcs have been thoroughly studied and used as dyes and pigments in the paint, printing, textile and paper industries, because of their intense blue-green colour [24]. Due to their great stability, enhanced spectroscopic characteristics, diverse coordination properties and flexibility, Pcs have gone beyond porphyrins in finding application in numerous areas [25]. Most recently, Pcs have found high-tech applications in electrophotography, ink-jet printing and as photo-conducting agents in photocopying devices [26]. Additionally, their novelty is rapidly developing in other fields such as chemical sensors, liquid crystals, semiconductors and functional polymers amongst others [27]. Of interest to us, they have also found great success in photodynamic therapy (PDT).

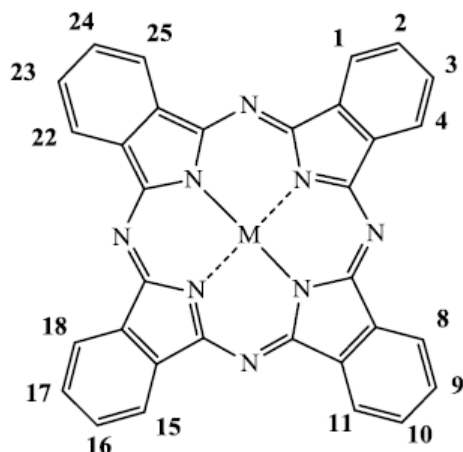


**Figure 1.4: Structure of the phthalocyanine molecule and potential sites for substitution on the Pc ring (numbering used traditionally for Pc nomenclature) [28].**

One of the most prominent recent applications of phthalocyanine (Pc) derivatives is their application in medicine as photosensitizers for the photodynamic therapy (PDT) of cancer. The various aspects of PDT, including the development and study of PSs, are described in detail in numerous reviews [29-33].

Pcs have many advantages over the porphyrin derivatives that are now widely used in clinics (HPD, Photofrin). Firstly, they have a more intense long-wavelength band red-shifted into the so-called ‘therapeutic transparency window’ where the transparency of biological tissues is higher. The increased oxidative stability of Pc molecules allows their use as stable aqueous solutions. Owing to enhanced fluorescence, Pcs can also be used for diagnostic purposes—for the detection of the presence and localization of tumours. Water-soluble sulfo-substituted Pc derivatives, especially chloroaluminium and zinc complexes, are the most studied as PSs for PDT [34-35].

### 1.2.2 Structure of phthalocyanines

The structure, charge and hydrophobicity of a photosensitizer reinforce its interactions with its surrounding, biological environment and thus its cellular uptake, subcellular localization and cytotoxicity may be determined [36]. For example, amphiphilic photosensitizers are more photodynamically active than hydrophobic or hydrophilic photosensitizers [37]. Amphiphilicity, the property of possessing hydrophobic and hydrophilic characteristics in different segments within the same molecule, allows distinct portions to interact differently with their biological surrounding, boosting solubility, enhancing cellular uptake and intracellular **targeting**, and regulating aggregation [38]. All of these issues affect the efficacy of the PS in PDT.

The use of substituted precursors leads to higher purity products in terms of the degree of substitution. Such substitutions can be achieved at any of the 16 available positions of the Pc structure (Figure 1.4). This process is favoured for substitutions to the framework, resulting in Pcs with enhanced properties [23]. The positions 1,4,8,11,15,18,22,25 are known as non-peripheral or  $\alpha$ - positions, while 2,3,9,10,16,17,23,24 are identified as peripheral or  $\beta$ - positions [39]. Functional groups have therefore been substituted onto the Pc framework to increase their efficacy where groups such as alkyl chains, ethers, amines and thiols amongst others, have also been introduced to improve solubility of Pcs [40]. Introducing quaternized or sulfonated groups as substituents also enhances the solubility of the Pc in aqueous media [41, 42], while organic functional groups such as thio ether and aryloxo functionalities allow for solubility in organic solvents [43, 44]. The substituents can be directly attached to the Pc framework or onto the phthalonitrile precursor prior to condensation to form the Pc ring [45].

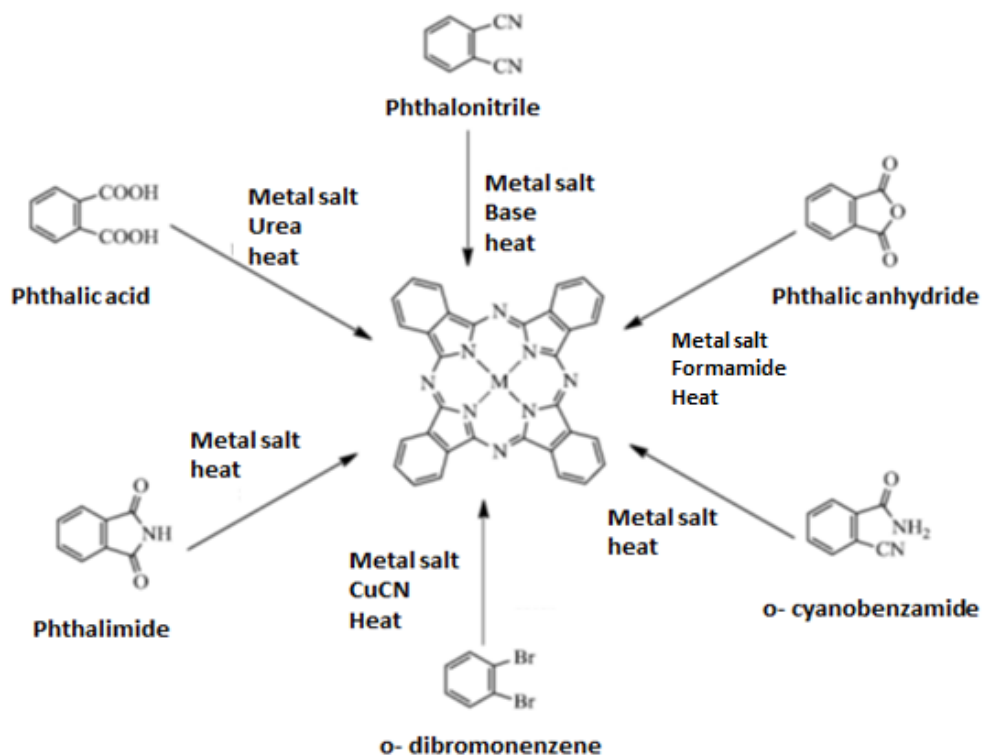


## 1.2.3 Synthesis of phthalocyanines

### 1.2.3.1 Synthesis via tetramerization of a single precursor

Quite a few ortho-substituted benzene derivatives can act as precursors in the synthesis of Pc macrocycles (Scheme 1.1). The precursors include phthalic anhydride, phthalic acid, phthalonitrile, phthalimide, diiminoisoindoline, *o*-cyanobenzamide, *o*-dibromobenzene and cyclohex-1-ene-1,2-dicarboxylic anhydride, amongst others. Phthalonitriles are frequently used in the synthesis of Pcs in the laboratory because they offer better yields, while phthalic anhydride is used in batch production, as it is comparatively cheap [46]. The phthalonitrile precursor method as employed for the purpose of this work; the benefit of using the phthalonitrile precursor is that it readily results in good yields of Pc complexes with most metals apart from mercury and silver, while precursors such as phthalimide and phthalic acid derivatives usually give inconsistent results. For the most part, phthalonitriles require heating with a metal salt in a high boiling point solvent such as quinoline or *N,N*-dimethylaminoethanol (DMAE) to form the Pc [47].

An easy method for the synthesis of Pcs by means of heating a phthalonitrile with a catalytic amount of DBU (1,8-diazabicyclo[5.4.0]undec-7-ene) or DBN (1,5-diazabicyclo[4.3.0]non-5-ene), known as the Tomoda method, was reported in the 1980s [48, 49]. This route may give up to 70% yields for the metal-free and 80% yields for the metallated Pcs. Strong organic bases like DBU and DBN usually enhance the formation of Pcs in higher yields, whereas weaker ones such as triethanolamine (TEA) and pyridine do not support the formation of Pcs. Utilisation enables the reaction to advance under milder conditions by promoting the formation of the alkoxide ion. Unsubstituted metal-free Pcs ( $H_2Pc$ ) can be synthesised following the Linstead method [50] from a phthalonitrile precursor in refluxing lithium, sodium or magnesium alkoxide solutions. The Pc can then be demetallated through the addition of a dilute acid to give the  $H_2Pc$ .



**Scheme 1.1: Synthetic routes to metallophthalocyanines (MPcs) from various precursors [22].**

The process for the condensation of phthalonitriles to form Pcs involves a stepwise polymerization of the precursors or reactive intermediates, preceded by coordination of the central metal ion (in case of MPcs) and finally the closure of the ring forming the macrocycle [51, 52]. The ring closure is facilitated by aromatization, thermodynamic stability and inherent stabilization due to the metal coordination. Metallated Pcs may also be made from metal-free Pcs ( $H_2Pcs$ ) via the addition of a metal salt into a reaction. The only limitation with this method is that it is impossible to add large metal ions into the Pc's central cavity [53]. Therefore, the metal salt has to be added into a refluxing solution of the Pc precursor (e.g. phthalonitrile) for successful addition of the metal ion to the central cavity.

Non-peripherally substituted Pcs (with substituents at the  $\alpha$  position) and peripherally substituted Pcs (with substituents at the  $\beta$  position) have also been synthesized from suitable

precursors. Alkoxy functional groups at the non-peripheral positions cause a large bathochromic shift of the Q-band into the IR region (above 750 nm) [54, 55]. Additionally, octa-substituted non-peripheral Pcs are attractive due to the substituents imparting greater solubility in organic solvents with the Pcs synthesized being single isomers [56, 57]. The octa-substituted peripheral Pcs can be attained by reacting 4,5-di-substituted phthalonitriles. If the two substituents are the same, then regiomericly pure Pcs are formed. Pre-formed Pc reactions may also be utilised to achieve the desired product.

#### 1.2.4 Photophysical and photochemical properties of phthalocyanines

Photophysical activities are the changes taking place in the electronic states of a molecule and they influence its chemical character. The energy transfer process results in a number of physical changes, taking place when light of a specific wavelength is absorbed; however, it leaves the chemical integrity of the molecule unchanged. The sample absorbs light and an electron is excited from a lower (stable state) to a higher energy level (which is unstable with respect to the ground state). The simplified Jablonski diagram shown in Figure 1.5 represents these pathways and the subsequent loss of energy experienced by the PS in returning to the ground state [58-60]. Absorption processes occur from singlet ground state,  $S_0$ , to a vibrationally excited level of the first singlet excited state,  $S_1$ , or to a second, higher energy, electronically excited state,  $S_2$ . Fluorescence is a radiative process, taking place when the excited PS molecules lose energy upon returning to the ground state ( $S_0$ ) directly from the excited  $S_1$  state. During collisions with solvent molecules, vibrational relaxation occurs and the  $S_2$ -excited molecules revert to the first vibration level of  $S_1$ , from which several processes can occur: namely, fluorescence, phosphorescence or heat processes.

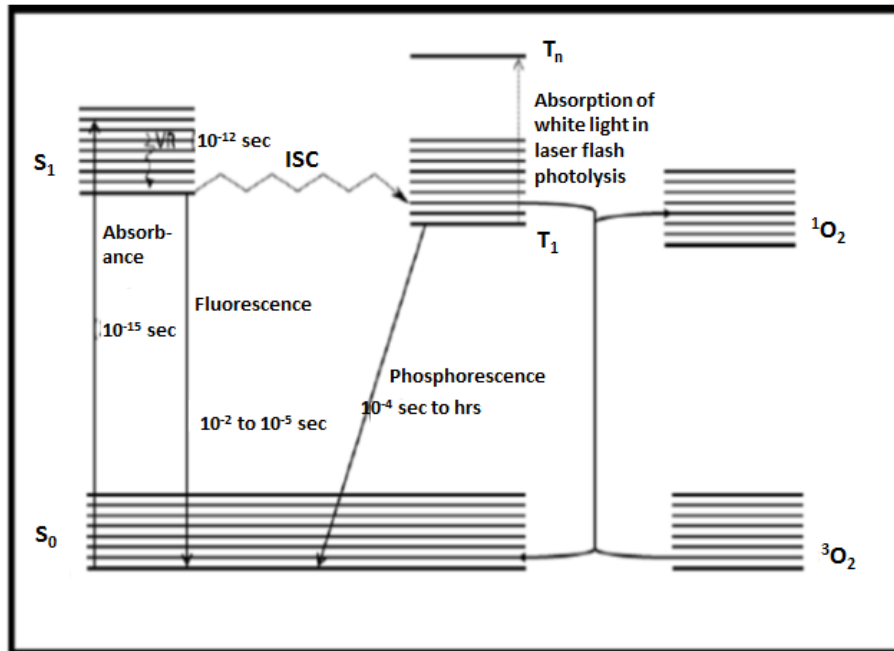


**Figure 1.5: Jablonski diagram illustrating the electronic states of a molecule and the transitions taking place between the excited states and the ground state [61].**

Phosphorescence is a radiative transition between the lowest triplet state and the ground state. As phosphorescence originates from the lowest triplet state, it will have a decay time approximately equal to the lifetime of the triplet state (ca  $10^{-4}$  to 10 sec). The phosphorescence process is preceded by internal conversion (IC) and intersystem crossing (ISC), which are non-radiative processes. Phosphorescence decay is similar to fluorescence, though an electron spin transition into a "forbidden" triplet state ( $T_1$ ), due to spin orbit coupling, takes place instead of to the lowest singlet excited state ( $S_1$ ). The non-radiative transition is known as intersystem crossing. The decay from the  $T_1$  electronic level takes place with lower energy relative to fluorescence (and due to the spin flip required, phosphorescence also has a much longer lifetime). If this transition occurs within body tissues, the excited PS molecules may transfer its energy to ground state molecular oxygen (also in the triplet state), generating singlet oxygen ( $^1O_2$ ). Singlet oxygen is known as one of the reactive oxygen species (ROS) and has the ability to initiate oxidation of the tissue components. Photodynamic therapy (PDT) is based on this feature [62].

### 1.2.4.1 UV-vis absorption spectra of phthalocyanines

All monomeric H<sub>2</sub>Pcs and MPcs display a characteristic UV-vis absorption spectrum, which includes a Soret-band at approximately 350 nm, and a main, strong Q-band in the near-IR region (670 – 750 nm), as shown in Figure 1.6. [63]. The Pcs possessing four substituents at the  $\alpha$ -position typically exhibit a bathochromic shift in their UV-vis absorption spectra [64], with the Q band red-shifted approximately 15 nm and the Soret bands red-shifted 20 nm in comparison to their mono-substituted Pcs. Both the number and position of the substituents on the macrocycle have a huge impact on the absorption spectra of Pcs. Pcs exhibiting narrow and intense Q-bands, obeying the Beer-Lambert law for both the Q-band and Soretband in the concentration range 10<sup>-6</sup> - 10<sup>-4</sup> mol/L, give an indication that no aggregation has occurred within this range [65]. Aggregation is described as the coplanar interactions of rings progressing from monomer to dimer higher order complexes occurring through  $\pi$ - $\pi$  interactions of the pc rings. Aggregation is an unfavourable feature as the aggregates are not photoactive [66].

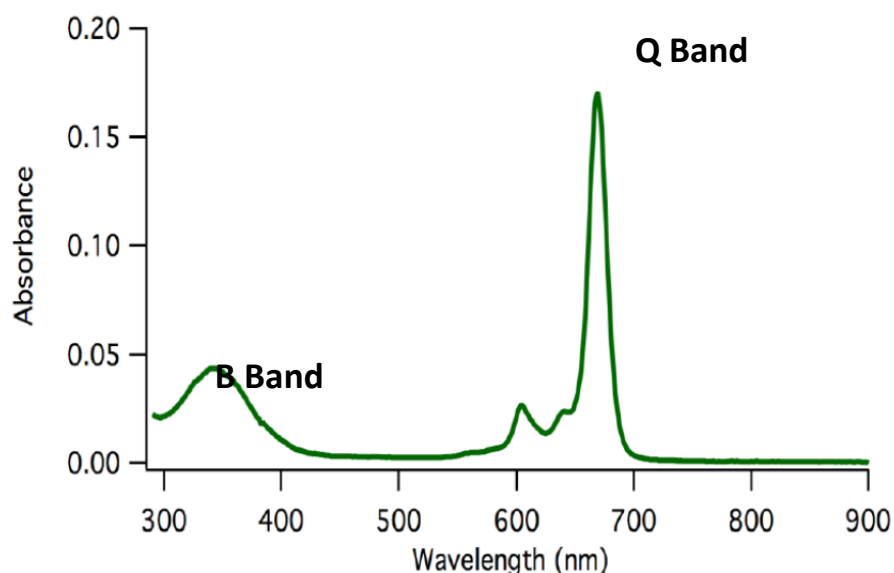


Figure 1.6: A typical absorption spectrum of a ZnPc in HPLC grade DMF solvent [63].

### 1.2.4.2 Fluorescence quantum yields and lifetimes

The fluorescence quantum yield ( $\Phi_F$ ) is defined as the number of photons emitted in relation to the number of photons absorbed. Therefore  $\Phi_F$  may be explained as the ratio of molecules fluorescing to the number of photons absorbed. The  $\Phi_F$  is used to determine and compute the efficiency of emission from the singlet state for a particular fluorophore. The  $\Phi_F$  value is a relative determination [67], utilising known compounds with standard fluorescence quantum yields, for example ZnPc in DMSO ( $\Phi_F$ ) = 0.20 [68], using equation 1.1.

$$\Phi_F = \Phi_{F(std)} \frac{F \cdot A_{std} \cdot n^2}{F_{std} \cdot A \cdot n_{std}^2} \quad (1.1)$$

where F and Fstd are the areas under the fluorescence curves of the sample and the standard respectively. A and Astd are the respective absorbances of the sample and the standard at the excitation wavelength, and n and nstd are the refractive indices of the solvents used for the sample and standard, respectively.

The fluorescence lifetime,  $\tau_F$ , of an excited species is the time needed for the concentration of the species to decrease to 1/e, of its original value [69] as shown in Figure 1.7. The  $\tau_F$  is associated with the radiative lifetime,  $\tau_0$ , as defined by equation 1.2. Fluorescence radiative lifetimes are used to explain the decrease of the lifetime of, for example, a Pc in the presence of nanoparticles. They are directly related to the absorption coefficients and excited lifetimes ( $\tau_F$ ). They are estimated from the fluorescence quantum yield ( $\Phi_F$ ) and lifetimes ( $\tau_F$ ) as shown in equation 1.2. Figure 1.7 shows a typical fluorescence decay curve, obtained using a TCSPC (Time Correlated Single Photon Counting) set-up. The fluorescence lifetimes of MPcs are usually of the order of a few nanoseconds [70].

$$\Phi_F = \tau_F / \tau_0 \quad (1.2)$$

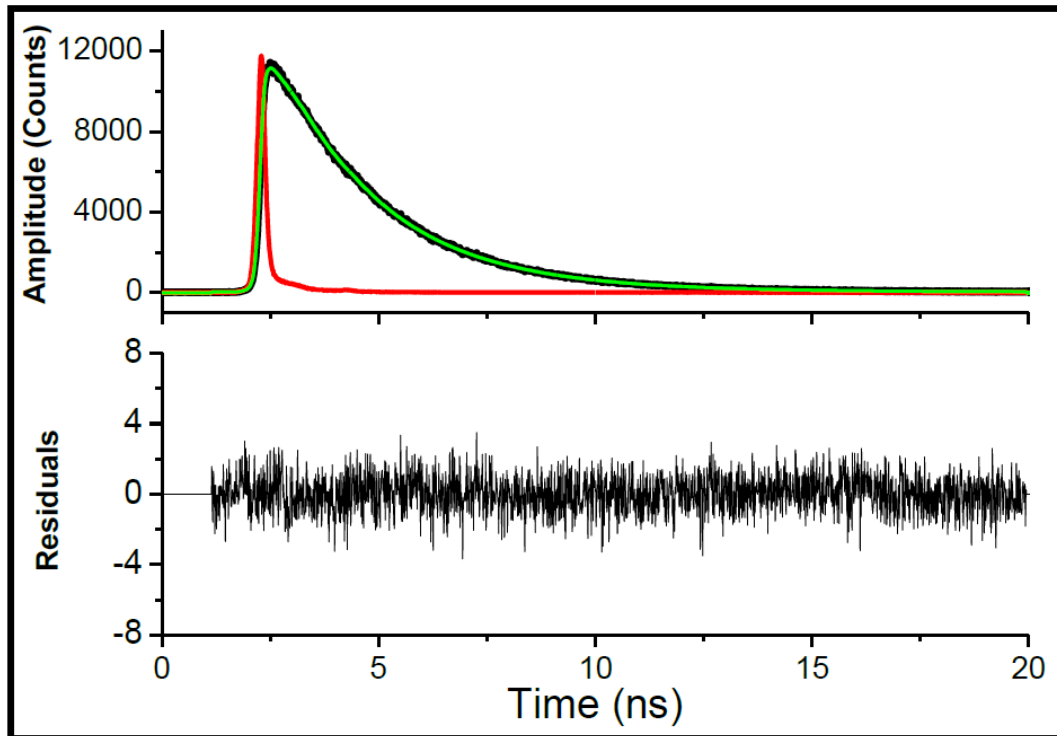


Figure 1.7: A typical fluorescence decay curve for a Zinc phthalocyanine (ZnPc) (red) [69].

#### 1.2.4.3 Triplet quantum yield and lifetimes

The triplet quantum yield ( $\Phi_T$ ) and lifetime ( $\tau_T$ ) are used to measure the efficiency of the phthalocyanine as a photosensitizer. The triplet quantum yield ( $\Phi_T$ ) is the quantity of molecules that undergo ISC from the first excited state,  $S_1$ , to the triplet state  $T_1$ . Phthalocyanine triplet quantum yields ( $\Phi_T$ ) and triplet lifetimes ( $\tau_T$ ) are usually determined using laser flash photolysis. This technique uses a high energy laser light together with a white light to determine and monitor the absorption of the molecule from the excited  $T_1$  state to higher energy states,  $T_n$ . A triplet decay curve of change in absorbance ( $\Delta A$ ) versus time in seconds is achieved from the experiment and from this the triplet lifetime ( $\tau_T$ ) can be computed. A typical decay curve is shown in Figure 1.8. A virtual method using zinc phthalocyanine as a standard is employed for triplet quantum

yields ( $\Phi_T$ ) calculations as shown in equation 1.3. Most Pcs reveal triplet-triplet absorption around the 500 nm region, far from the ground singlet state absorption making it possible to conduct these measurements [71, 72].

$$\ddot{O}_T = \ddot{O}_T^{std} \frac{\ddot{A}_{A_T} \cdot \dot{a}_T^{std}}{\ddot{A}_{A_T}^{std} \cdot \dot{a}_T} \quad (1.3)$$

where  $\Delta A_T$  and  $\Delta A_T$  are the changes in the triplet state absorbance of the sample and standard, respectively.  $\epsilon_T$  and  $\epsilon$  are the triplet state molar extinction coefficients for the sample and standard, respectively [73].

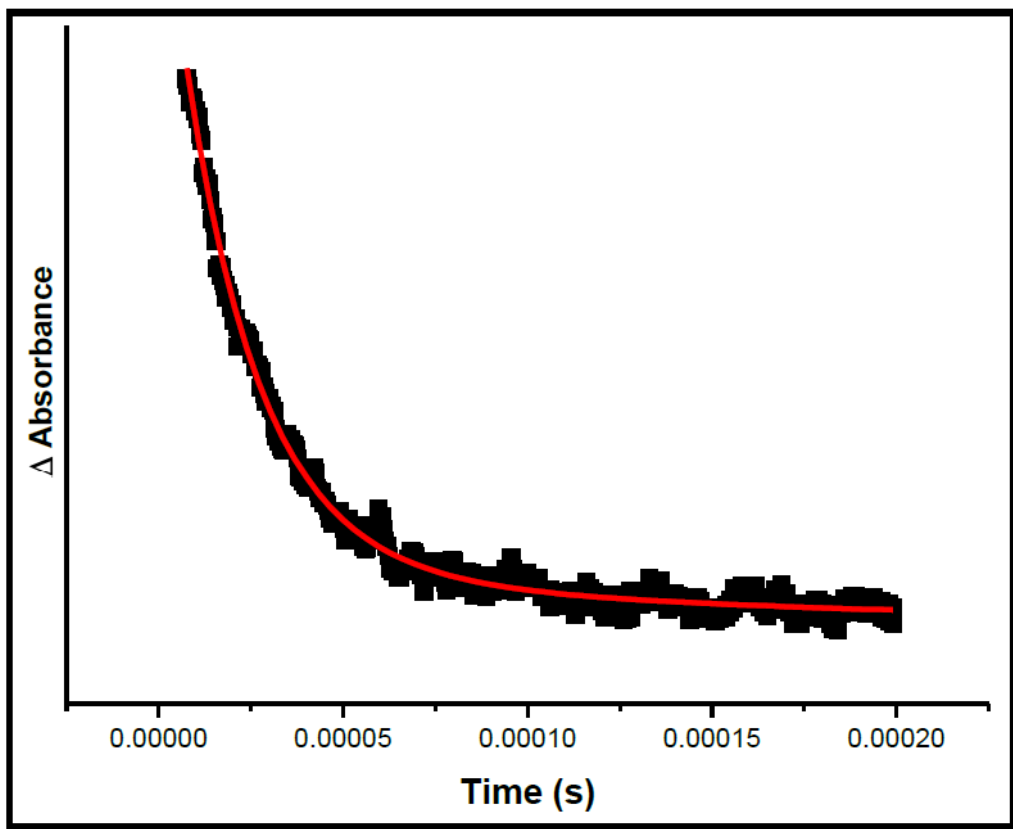


Figure 1.8: A typical triplet decay curve obtained for a Pc in DMSO [74]

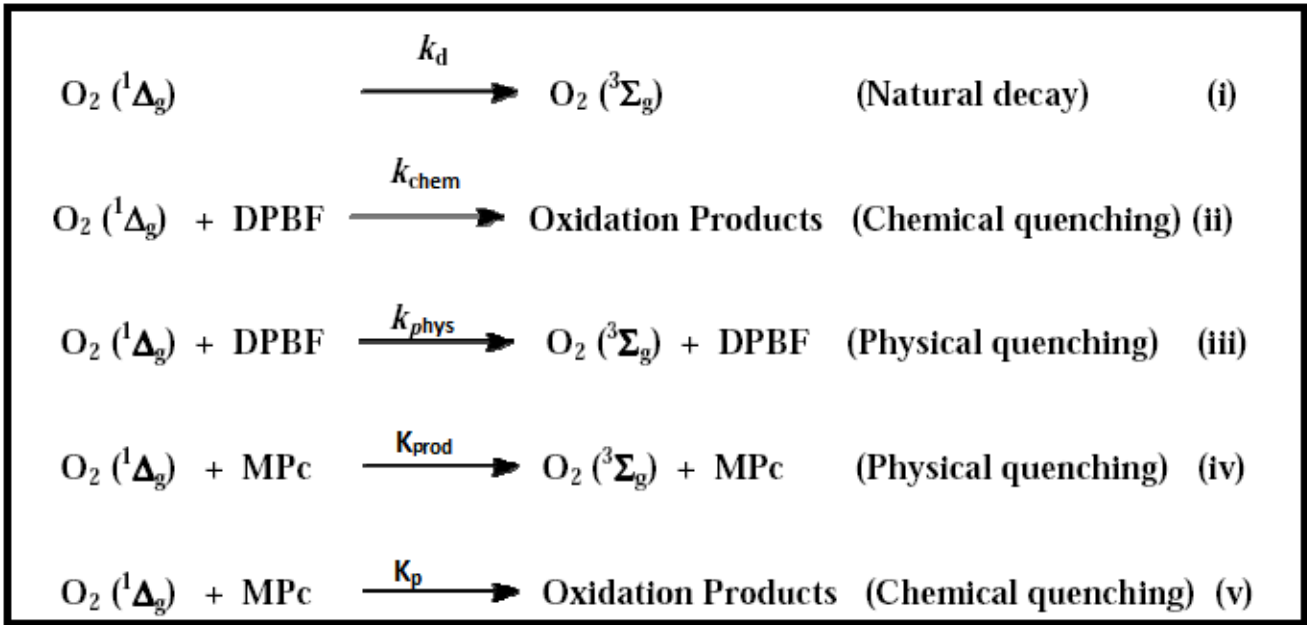


#### 1.2.4.4 Singlet oxygen quantum yield

Singlet oxygen ( $^1\text{O}_2$ ) is an extremely reactive species and is responsible for the light-induced oxidative damage of malignant or bacteria/virus infected tissue.  $^1\text{O}_2$  is generated when oxygen in its triplet ground state ( $^3\text{O}_2$ ) interacts with a sensitizer in a process called photosensitization, (Figure 1.2, Type 2 mechanism). Singlet oxygen is determined by two main methods, using chemical quenchers or by measuring the luminescence of singlet oxygen at 1270 nm [74]. In this work, the singlet oxygen scavengers, 1,3 diphenylisobenzofuran (DPBF) or anthracene-9,10-bis-methylmalonate (ADMA) were employed. Other known singlet oxygen quenchers are 1,4-diazabicyclo-octane (DABCO) and sodium azide ( $\text{NaN}_3$ ); the latter is usually used in aqueous media, while the former is often employed in organic solvents. This chemical method is the most common method used for quantifying singlet oxygen in the laboratory. After the generation of singlet oxygen, it is trapped using a singlet oxygen quencher. The quencher readily reacts with singlet oxygen in a 1:1 ratio without side reactions or decomposition products that may interfere with the detection of singlet oxygen [75]. The disappearance of the quencher is studied spectroscopically and Scheme 1.2 shows the disappearance of DPBF with  $^1\text{O}_2$  generation in the mixture.  $^1\text{O}_2$  in the presence of the DPBF can undergo a series of reactions (Scheme 1.2) [76]. The quantum yield of singlet oxygen ( $\Phi_\Delta$ ) is used to determine the efficiency with which various photosensitizers generate singlet oxygen. The values are determined using equation 1.4. The singlet oxygen quantum yield ( $\Phi_\Delta$ ) determinations for the various phthalocyanine samples were recorded using a set-up as shown in Scheme 2.3 and a singlet oxygen decay curves similar to that shown in Figure 1.9 were be obtained.

$$\Phi_{\Delta} = \Phi_{\Delta}^{std} \frac{R \cdot I_{abs}^{std}}{R^{std} \cdot I_{abs}} \quad (1.4)$$

where  $\Phi_{\Delta}^{std}$  is the singlet oxygen quantum yield for the standard ZnPc.  $R$  and  $R^{std}$  are the photodegradation rates of ADMA or DPBF in the presence of a sensitizer under investigation and the standard, respectively.  $I_{abs}$  and  $I_{abs}^{std}$  are the rates of light absorption by the sensitizer and standard, respectively.



Scheme 1.2: Photochemical reactions leading to the decay of singlet oxygen in a solution of photosensitizer (MPC) and quencher (DPBF);  $k_d$ ,  $k_{\text{chem}}$  and  $k_{\text{phys}}$  refer to the rate constants for first order natural decay, chemical and physical quenching by DPBF respectively;  $k_{\text{prod}}$  and  $k_p$  are the rate constants for chemical and physical quenching of singlet oxygen by the photosensitizer [76].

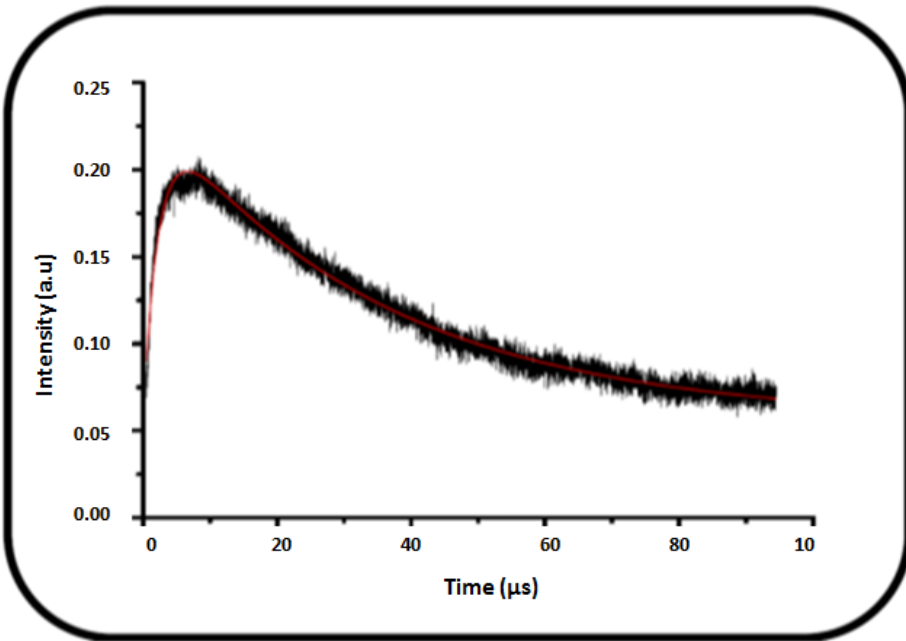


Figure 1.9: Typical singlet oxygen decay signal at 1270 nm for an MPC in DMSO.

### 1.3 Hyperthermia therapy

Hyperthermia therapy involves the generation of heat during cancer therapy; the term implying treatment based on the generation of heat at the tumor site [77]. This treatment process complements the cancer treatments currently available including: chemotherapy, radiation therapy, surgery, gene therapy and immunotherapy for cancer [78]. The approach relies on raising the temperature of **the** tumour environment, resulting in a change in the physiology of diseased cells, thus leading to apoptosis [79]. Based on the degree of temperature increase, hyperthermia treatment can be classified into different types namely, in thermo ablation, where a tumour is subjected to high temperatures  $> 46\text{ }^{\circ}\text{C}$  (up to  $56\text{ }^{\circ}\text{C}$ ) causing cells to undergo direct tissue necrosis, coagulation or carbonization. The level of effectiveness of any hyperthermia treatment largely depends on the temperatures generated at the target site of action, the period of exposure and the type of cancer cells [80].

Hyperthermia is also categorized into local, regional and whole body hyperthermia, depending on the site of disease. Whole body hyperthermia, as the name implies, is applied to treat metastatic cancer cells which are spread all over the body. Regional hyperthermia involves heat subjection to larger areas, for instance the whole tissue and organ, while local hyperthermia refers to the subjection of a small tumour to heat. Of these, local hyperthermia is achieving the most attention because of the generation of intracellular heat. However, the challenge lies **in** heating only the tumor cells without affecting healthy tissues [81].

The application of magnetic materials for hyperthermia treatment of cancer was first proposed in 1957 with the possibility of converting dissipated magnetic energy into thermal energy [82]. Later, the idea developed into a well-researched field as magnetic nanoparticles (MNPs) were introduced. Nanomaterials have generated a great deal of interest due to their larger surface area to volume ratio, small sizes and possibility of surface functionalization.

MNP-based hyperthermia treatment has a significant amount of advantages over conventional hyperthermia treatment. Highlights (in Figure 1.10) include: 1) the frequencies of oscillating

magnetic fields used pass harmlessly through the body generating heat only in tissues containing MNPs, 2) cancer cells that have absorbed MNPs thus have increased hyperthermia efficacy by transferring the therapeutic heat directly to the cells, 3) MNPs can be **functionalized**, using cancer-specific binding **agents**, which allows for a more selective and effective treatment, 4) **owing to their small** size and the capping agent present on the MNPs, they can also effectively cross the blood-brain barrier (BBB) and can therefore be used for treating brain tumors, 5) MNPs are stable and these can therefore be administered via a number of drug delivery routes, 7) MNPs are typically a few nano-meters in size and they can therefore pass easily into several tumours where the pore sizes are generally in the 380 – 780 nm size range, 8) MNP-based heat generation is more efficient and homogeneous in relation to macroscopic implants, 9) MNP-based hyperthermia treatment may also induce anti-tumoral **immunity**, and 10) most importantly, MNP-based hyperthermia can also be utilized for the targeted delivery of drugs [83-91]. These additional qualities open up possibilities for the advancement of multifunctional and multi-therapeutic approaches for treating a number of diseases.

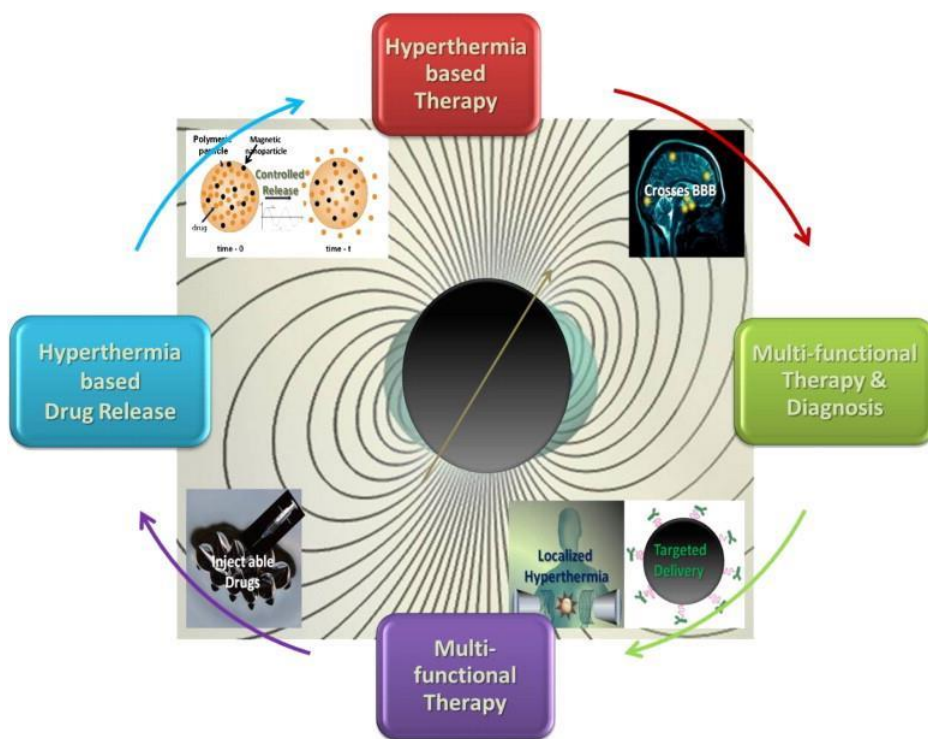


**Figure 1.10: A schematic representation of some of the unique advantages magnetic nanomaterials offer in hyperthermia-based therapy and controlled drug delivery [84].**

## 1.4 Magnetic Resonance imaging (MRI)

### 1.4.1 Principles of Magnetic Resonance Imaging

Magnetic Resonance Imaging (MRI) is the main, non-invasive, diagnostic technique used in medical science. As compared to other imaging modalities, a remarkable advantage of MRI is its superior spatial resolution, however, the limited sensitivity offered by the probes used is a drawback [91,92]. MRI has other numerous advantages which include flexibility, extreme imaging, patient nontoxicity, high-resolution images with exceptional soft tissue contrast between different tissues, and the acquisition of unique clinical information [93-96]. Hydrogen proton nuclei are employed to produce the image, as they are the most abundant nuclei found in the body, with the highest concentrations found in the water and lipid molecules [97]. Recently, attempts have been made to enhance the sensitivity of this technique and facilitate biological and efficient information-rich imaging by making use of MNPs. The emergence of nanotechnology in the 1990s led to the invention of several contrast agent probes [98, 99].

### 1.4.2 Classes of contrast agents








The major drawback of MRI in molecular imaging is its low sensitivity compared with nuclear imaging for example. Presently, about 35% of MRI tests involve the use of contrast agents, but this percentage is expected to further increase following the development of more effective and specific contrast probes. MR contrast agents (MRCAs) operate by shortening longitudinal relaxation time ( $T_1$ ) and transverse relaxation time ( $T_2$ ), which can guarantee several requirements for clinical applications including: ample relaxivity and susceptibility effects, elimination, low toxicity, tolerance, stability, optimal bio-distribution and safety [80].

### 1.4.2.1 Longitudinal relaxation ( $T_1$ ) contrast agents

Longitudinal relaxation (also known as spin-lattice relaxation) reveals a thermal loss from the spin system to its surroundings (lattice). The main advantage of  $T_1$  contrast agents, as compared to  $T_2$  contrast agents, is that an enhancement in the signal results in the acquisition of positive images. Positive contrast agents reduce the  $T_1$  relaxation time, creating a bright contrast. The magnetizations of paramagnetic materials, such as gadolinium complexes, are directly reliant on the number of ions and its unpaired electrons, displaying no magnetization in the absence of an external magnetic field. Table 1.1 displays some of the paramagnetic metal ions available or used as contrast agents [15].

There are other transition metals and lanthanide metals with unpaired spins, but for the metal to be effective as a relaxation agent, the electron spin-relaxation time must match the Larmor frequency of the protons. And this condition is accomplished better with  $Fe^{3+}$ ,  $Mn^{2+}$  and  $Gd^{3+}$  ions. The major problem with paramagnetic heavy metal ions is their toxicity. Both the metal ion and the ligand tend to show substantial toxicity in their free state. Slower clearance from the body is likely to significantly increase the toxicity of any  $Gd^{3+}$  complex. However, the discovery of a less toxic compound, with different metals and paramagnetic properties, is possible [100].

**Table 1.1: Configuration and magnetic moments of some paramagnetic metal ions.**

Ion	Configuration	Magnetic moment
$^{24}\text{Cr}^{3+}$		3.9
$^{25}\text{Mn}^{2+}$		5.9
$^{26}\text{Fe}^{3+}$		5.9
$^{29}\text{Cu}^{2+}$		1.7
$^{63}\text{Eu}^{3+}$		3.4
$^{64}\text{Gd}^{3+}$		7.9
$^{66}\text{Dy}^{3+}$		10.6

### 1.4.2.2 Gadolinium-based contrast agents

The risk associated with toxic Gd ions, the short half-lives and the low relaxivity has limited the application of Gd-based agents. The most frequent **side-effects** are headache, nausea and dizziness for a short time after the injection. This occurs in 1% to 5% of contrast agent based injections. Because of its high availability and chemical stability,  $\text{Gd}^{3+}$  is extensively used **as a MRCA** [101-103]. In comparison to iron oxide,  $\text{Gd}^{3+}$  or  $\text{Mn}^{2+}$  based nanoparticles show relatively stronger paramagnetic properties. They thus enhance the MRI contrast more efficiently and are commonly used in clinical MRI. Angiography scans can be performed by utilising Gd contrast media and the evaluation of many myocardial (heart) abnormalities can only be fully assessed and treated by using gadolinium contrast agents [104]. Figure 1.11 shows the function of MNPs in disrupting the normal magnetic relaxation processes of a proton [105]. From this **Figure** 1.11, it can be seen that the induced magnetic field created by the MNPs agitates the magnetic relaxation processes of the protons in neighbouring water molecules,





resulting in the shortening of the spin–lattice relaxation time of the proton, together with a concomitant enhancement of the signal.

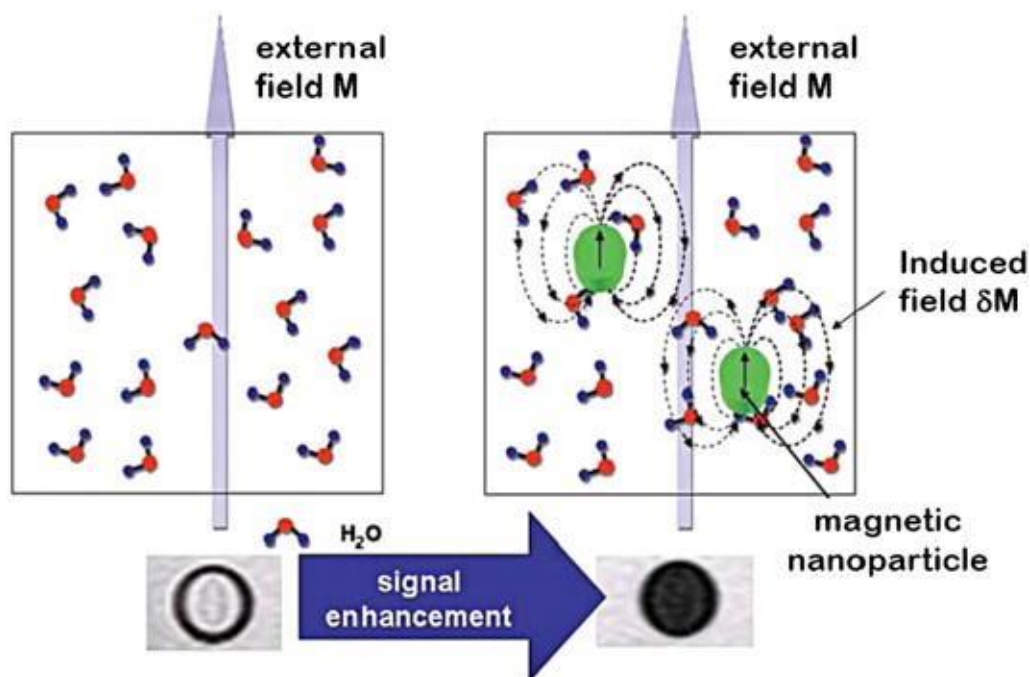


Figure 1.11: **Diagram** showing the function of MNPs in the perturbation of the magnetic relaxation processes of the proton [105].

## 1.5 Magnetic Nanoparticles

### 1.5.1 Application of phthalocyanines with magnetic nanoparticles

Many metallophthalocyanines have been found to have low solubility which is one of **their** significant limitations in biological applications and catalysis. The substitution of the aromatic rings of the phthalocyanines has shown to improve the solubility of the phthalocyanines particularly in aqueous media [106].

Once phthalocyanines are soluble in aqueous media another problem arises; the separation of the phthalocyanine from the aqueous media when they have to be released from the body. It is important that the phthalocyanine be able to be washed out of the body after treatment and therefore the separation process is essential. In addition, in catalysis, separation is important in order to be able to recycle the catalyst [107]. However, MPcs soluble in aqueous media have been shown to aggregate, reducing their catalytic behaviour [108]. Studies have been done where the Pcs are dispersed onto supports to obtain a heterogeneous catalyst. Nanoparticles have emerged as an efficient alternative for the immobilisation of homogeneous catalysts. Again, the recovery of these nanosized particles has been problematic, limiting their wide application [109]. Current interests involve combining magnetic nanoparticles like Fe<sub>3</sub>O<sub>4</sub> with these catalysts for biological and technological applications. The combination of these two nanomaterials brings together the separation power of the magnetic nanoparticles and the catalytic action of the MPcs [110]. Table 1.2 lists some of the magnetic nanoparticles used with Pcs for a variety of applications.

**Table 1.2: Magnetic nanoparticles used in combination with metallophthalocyanines for various applications.**

<b>Magnetic Nanoparticle</b>	<b>Metallophthalocyanine</b>	<b>Application</b>	<b>Ref</b>
NaGdF <sub>4</sub> :Yb, NaGdF <sub>4</sub> @SiO <sub>2</sub>	Aluminium tetracarboxy Pc (AlC <sub>4</sub> Pc)	MRI and PDT	[111]
Iron oxide (Fe <sub>3</sub> O <sub>4</sub> )	Zinc octacarboxy Pc (ZnOCPC)	Catalysis	[112]
Silica nanoparticles (SiNP)	Iron tetracarboxy Pc (FeTCPC)	Catalysis	[113]

### 1.5.2. Properties of Gd<sub>2</sub>O<sub>3</sub> nanoparticles

Nanoparticles with d orbitals (Gd<sub>2</sub>O<sub>3</sub>, GdPO<sub>4</sub>, GdF<sub>3</sub>, NaGdF<sub>4</sub>, etc.) are attractive, potential single phase multifunctional bio-probes revealing a number of magnetic and optical properties within one particle. Studies have been done on Gadolinium oxide (Gd<sub>2</sub>O<sub>3</sub>) nanoparticles as the host matrix for downconversion [114-116] and upconversion [117, 118] luminescence processes due to **their** interesting physical properties, such as high melting points (2320°C), chemical durability, thermal stability and low phonon energy (600 cm<sup>-1</sup>). Among various Gd-based nanoparticles, gadolinium oxide nanoparticles have been accepted as effective T<sub>1</sub> MRI contrast agents [119]. Figure 1.12 shows the structure of the gadolinium oxide nanoparticle.

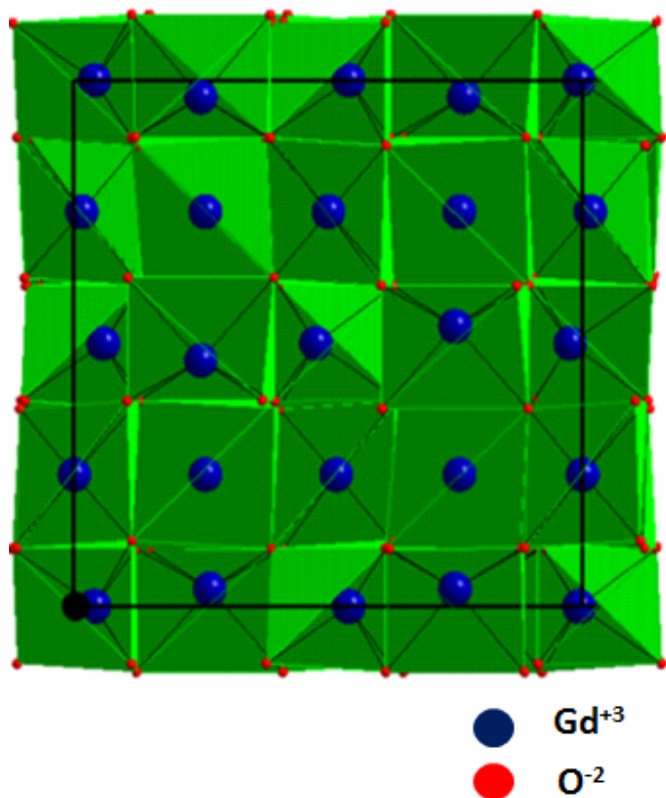


Figure 1.12: Crystal structure of the gadolinium oxide nanoparticle unit cells [114].

### 1.5.3 Synthesis of $\text{Gd}_2\text{O}_3$ contrast agents and nanoparticles

Usually gadolinium-based contrast agents are synthesised by the formation of a chelate, i.e., using a chelating agent to stabilize the metal ion (for example, diethylene triamine pentaacetic acid (DTPA) or 1,4,7,10-tetraazacyclododecane-1,4,7,10-tetraacetic acid (DOTA)) but recently a number of other methods have been proposed. Among these, metallofullerenes where the Gd ions are encapsulated in a fullerene cage [120, 121,122], metal–organic frameworks (MOFs) and nanoscale coordination polymers (NCP) [123] have been used. The latter, however, is quite complex involving several steps. A main limitation of organic systems like MOFs and metallofullerenes is their large particle size (usually 100 nm), and since large molecular species are usually rapidly recognized by phagocytes and excreted by the reticulo-endothelial system

(RES) [124]. The nanoparticles size of the contrast agent is thus a critical parameter and so is its chemical stability.

The best way to collect a large number of Gd ions contained within a small volume is to employ **nanocrystals**, e.g. gadolinium oxide ( $Gd_2O_3$ ) [125-127], gadolinium fluoride ( $GdF_3$ ) or gadolinium phosphate ( $GdPO_4$ ). The crystals are preferably kept as small as possible to provide a large surface to bulk ratio and thus an efficient interaction between Gd(III) and water molecules; i.e. a high-water exchange. Small or ultrasmall  $Gd_2O_3$  nanoparticles synthesized according to the polyol route have been extensively studied; they have been used in this work and others. The yield of the polyol synthesis is, however, low and a severe disadvantage is the necessity for lengthy purification methods to free the nanoparticle solutions from free Gd(III) ions. Furthermore, the as-synthesized polyol-prepared nanoparticles are usually dispersed in diethylene glycol (DEG), which is a toxic chemical known to induce **renal inflammation**, thus not suitable for oral intake or intravenous injection [128].

#### 1.5.4. Characterization and application of gadolinium oxide nanoparticles

Generally, there are a large number of different characterization techniques that can be employed for the characterization of magnetic gadolinium oxide nanoparticles. These include, XRD which can be used to give a fair idea of the crystalline nature and the phase transitions of the nanoparticles. Scanning electron microscopy (SEM) and transmission electron microscopy (TEM) techniques are both particularly useful in understanding and quantifying the nanoparticle morphology. Electron paramagnetic Resonance (EPR), Thermogravimetric analysis (TGA), Ultraviolet-visible (UV/vis) **spectroscopy and Fourier transform infrared (FTIR) spectroscopy**, to name a few are also used to characterize nanoparticles and these were also employed for the characterization of the synthesized gadolinium oxide nanoparticles in this work. **The characterization techniques probe into** the internal structure and properties such as the structure, size, thermal stability, chemical composition, absorption, fluorescence, magnetic ability, amongst others, of the material being analysed.

Magnetic gadolinium oxide nanoparticles have been the subject of intense research for the past 50 years; however, this field of study has only now become one of great focus in modern nanotechnological applications. The property of magnetism opens up a wider facet in the application of the nanomaterials [129]. Gadolinium oxide nanoparticles have been studied and they have been shown to be excellent magnetic resonance imaging (MRI) contrast agents. During MRI, the contrast agents play a role of distinguishing the healthy tissues from the tumour cells [130]. Additionally, when the surface of the nanoparticles is modified with photodynamic therapeutic agents such as photosensitizers, they may show enhanced permeation and retention (EPR), which is a property where these molecules tend to accumulate in tumor tissues more than they do in normal cells [131]. A treatment such as hyperthermia treatment (HPT), where a magnetic field is applied together with magnetic nanoparticles to raise body temperature has shown great promise in terms of increased tumour shrinkage [132] and functionalization of a nanomaterial is an effective approach to modify their surface properties [133]. For certain applications it is essential to tune the surface characteristics of the nanomaterial. Similarly for magnetic nanoparticles, functionalization has been used particularly for nano-applications (biotechnological applications, medicine such as cell separation, drug delivery, hyperthermia, DNA extraction and MRI) [134]. The coating/capping of the nanoparticle is critical in enhancing their solubility in water and in allowing the nanoparticles (NPs) to be used for biological applications. Water soluble NPs are always necessary for biological applications; however, it becomes difficult to isolate these nanoparticles once they become water-soluble [135].

## 1.6 Electrospinning

The assembling of the Pc-MNP conjugate onto polymer nanofibers increases the surface area of the catalytic surface therefore enhancing the catalytic activity of the nanofibers. This is the first time a Pc-Gd<sub>2</sub>O<sub>3</sub>NP conjugate has been incorporated into a polymeric fiber matrix and used for the photocatalytic degradation of orange G. Gold nanoparticles conjugated to phthalocyanines have also been embedded onto nanofibers for catalytic applications [136], while carbon nanofibers loaded with cobalt nanoparticles have been studied in the electrocatalysis of amino acids [137]. The gadolinium oxide nanoparticles used have been shown to possess magnetic behaviour and thus they will be efficient for the recovery of the catalyst, either on their own or within a solid support.

Electrospinning was introduced in the 20th century and the principles of electrospinning were described by Zeleny in 1914 [138]. In 1969 Taylor explained the concept of the Taylor cone and the parameters which would result in achieving the best Taylor cone [139]. Electrospinning is a platform technology for producing novel nanofibrous materials with a high surface to volume ratio, significant fibre interconnectivity and microscale interstitial spaces and it is known as the cheapest and most simple method for the production of ultrafine nanofibers with diameters ranging from 100nm to 1 μm. Electrospun nanofibers give small pore sized fibers with a large surface area and easily functionalised surfaces [139]. Electrospun fibres are of great interest in a diverse range of applications ranging from cell biology and tissue engineering, through filtration to power and optoelectronic devices. Recently, the process of electrospinning has attracted much attention because it can consistently produce polymer fibers that range from 5 to 500 nm in diameter [140,141].

Polyamides have been vastly used in electrospinning, there are different types of polyamides, however, for this research polyamide-6 was employed. Polyamide-6 is an aliphatic polymer made from [NH-(CH<sub>2</sub>)<sub>5</sub>-CO] monomer [141]. This polymer was chosen due to its great flexibility and resistance to chemical degradation and heat damage. Therefore, it can be used in media of any temperature or pH [142].

### 1.6.1 Electrospinning process parameters

The setup of the electrospinning process is very simple and consists of three major components: a high-voltage power source, a syringe with a metal needle connected to a syringe pump and a grounded conductive collector [143], as illustrated in Figure 1.13. In this process, a polymer solution is subject to an electrical field. Initially the polymer solution forms a droplet at the end of the capillary tube. As the voltage increases, a charge is induced on the fluid surface, and the droplet is distorted to form a conical shape known as the Taylor cone. When a critical voltage is reached, a jet is ejected from the apex of the cone. As the jet accelerates and thins in the electric fields, radical charge repulsion results in splitting of the primary jet into multiple filaments by splaying as illustrated in Figure 1.13[144].

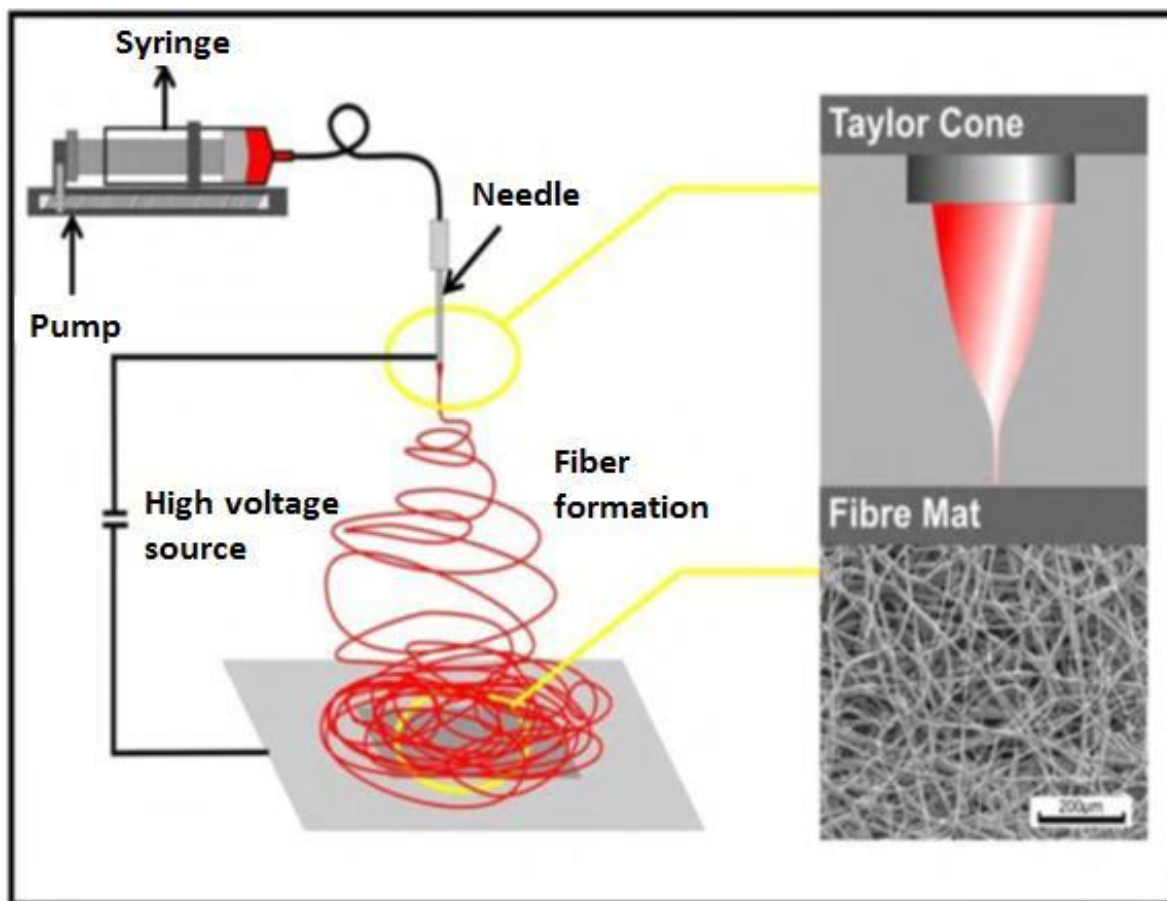


Figure 1.13: Schematic drawing of the electrospinning technique setup [144].



Although the working principle of electrospinning is rather **straight-forward** as described, it is influenced by many parameters which can influence the morphology of the fibers. These governing parameters can be categorized into three main types: 1) solution (e.g. concentration, viscosity, surface tension and conductivity of the polymer solution), 2) process (e.g. applied electrostatic potential, collection distance and feed rate) and 3) ambient parameters (e.g. temperature, relative humidity and velocity of the surrounding air in the spinning chamber) [141, 144]. The concentration of the polymer solution allows for sufficient chain entanglement, uninterrupted and consistent electrospun fibers under the applied electric field [149]. The polymer concentration in solution usually determines **whether it** is electrospinnable and generally has a great effect on the fiber diameter, as well as fiber morphology. High concentrations generally produce fibers of a large average diameter; **however**, the quantitative relationship between the concentrations of the solution and the average fiber diameter is variable depending on the polymer used. At extremely low polymer concentration, fibers do not usually form and the solution simply sputters or sprays out [145].

Environmental factors such as humidity and temperature have an effect on the quality of the fibers formed. The rate of drying of the polymer jet is confirmed by the surrounding conditions and will determine whether the fibers will be fused or not in the fiber mat. The process parameters also include tip to collector distance, flow or pump rate and the voltage applied. All these influence the quality of the fibers obtained in different ways. A good combination of all these parameters generally leads to the appropriate formation of fibers for the desired application.

### **1.6.2 Characterisation of electrospun fibers**

In order to study the morphology, molecular structure and purity of the nanofibers, various techniques were used to characterize the nanofibers. Scanning Electron Microscopy and Transmission Electron Microscopy were used for the determination of the geometric properties

of the fibers. These two techniques give a 2-dimensional representation of the electrospun fibers and by analyzing the images obtained, one can also detect any defects on the fibers.

### 1.6.3 Applications of electrospinning

Photocatalysis is a growing application for phthalocyanine functionalised nanofibers. Studies have been done with other phthalocyanines for various applications. ZnPc has been embedded on a polyurethane polymer nanofiber and used in anti-bacterial applications [146]. Copper tetraaminoPc (CuTAPc) has been used in optoelectronics using a poly(ethylene oxide) polymer [147]. Also in photocatalysis, a Lutetium tetraphenoxy Pc (LuTPPc) on polystyrene nanofibers was applied for the photodegradation of 4-nitrophenol [148]. Electrospinning has also been employed for textile manufacturing [149] and filtration [150].

## 1.7 Background on environmental pollutants used in this work

Phthalocyanine-gadolinium oxide nanoparticle conjugates have excellent properties and can be used for developing functional polymer composites having promising physical, chemical, optical and catalytic properties [112]. The unique properties and the multi-functionality of these polymeric fibers are used in applications such as sensors, optoelectronics, drug delivery and photocatalysis. In this work, the photocatalytic degradation of a common water pollutant Orange G (OG) was used as an example of the application of phthalocyanine-nanoparticle conjugates incorporated into electrospun fibers. Other work where gold or iron oxide nanoparticles were used in different polymers matrices has been done [112].

### 1.7.1 Background on azo dyes

Azo dyes account for approximately 60-70% of all dyes used in food and textile manufacture [151]. They are synthetic colours that contain an azo group, -N=N-, which also imparts the colour, as part of the structure. Azo groups do not occur naturally and most contain only one azo group, but some contain two (*disazo*), three (*trisazo*) or more [152]. Several degradation products of the dyes have been found to be mutagenic or carcinogenic and subsequently wastewaters originating from azo dye production or application industries pose a major threat to the surrounding ecosystems and human beings' health [153-154].

Azo dyes are pH stable, heat stable and do not fade when exposed to light or oxygen [155]. Various physico-chemical techniques have been applied in the removal of azo dyes. These techniques included filtration, coagulation, precipitation, adsorption and ion exchange [156]. However, these methods are not destructive, but only change the dye from one phase to another [157,158]. Recently advanced oxidation processes (AOPs) have been employed in the destruction of hazardous dyes [159]. Examples of these AOPs are the Fenton reaction [160], wet air oxidation [161], ozonation [162], and electrolysis [163], amongst others. These have been widely studied, however, photolysis has been employed more successfully due to its use of easy to handle reagents and it is comparatively inexpensive [164]. In this work orange G dye was used for the Photodegradation studies, the photoproducts represented in Figure 1.14 were found to be non-toxic.

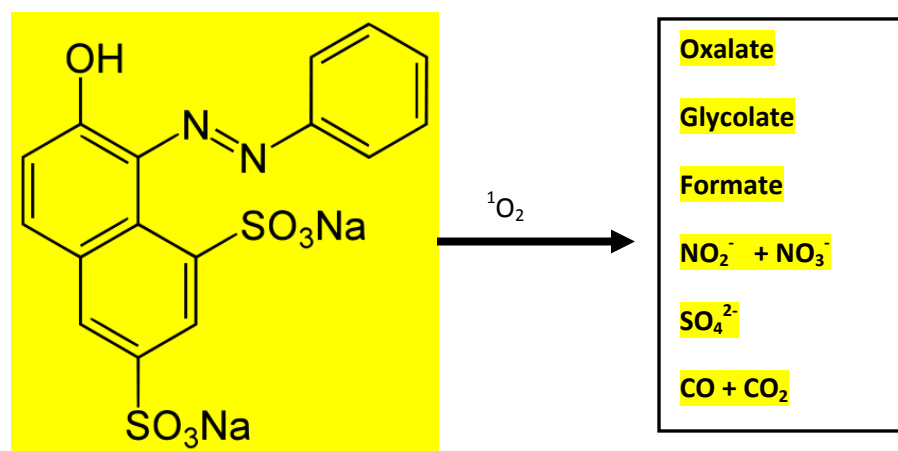


Figure 1.14: Photodegradation of the orange G dye.

## 1.8. Summary of the aims of this thesis

The aim of this work is to create a multifunctional nanocomposite based on phthalocyanine, gadolinium oxide nanoparticles and polymer fibers. This multifunctional nanocomposite/hybrid can then be used as a photocatalyst in the photodegradation of orange G, an organic pollutant.

The aim of this thesis is therefore to:

1. Synthesise and characterize magnetic gadolinium oxide nanoparticles.
2. Synthesise and characterize a zinc tetracarboxyphenoxy phthalocyanine.
3. Synthesise and characterize a phthalocyanine functionalized gadolinium oxide nanoparticle conjugate.
4. Form electrospun nanofibers and study the effect of different parameters on the electrospinning process.
5. Fabricate the electrospun fibers functionalized with phthalocyanine and phthalocyanine-gadolinium oxide nanoparticle conjugates.
6. Characterize the functionalized fibers using various spectroscopic techniques.
7. Investigate of the suitability of the polymer fibers containing the phthalocyanine and the phthalocyanine-gadolinium oxide nanoparticles for the photodegradation of orange-G in aqueous media.

## 1.9 References

1. A.C. Kubler, Photodynamic therapy Med. Laser Appl., 20 (2005), 37–45
2. A. Mitra, G.I. Stables Topical photodynamic therapy for non-cancerous skin conditions. photodiag. Photodyn. Ther., 3 (2006), 116–127
3. M. Alexiades-Armenakas, Laser-mediated photodynamic therapy. Clin. Dermatol., 24 (2006), 16–25
4. J.J. Schuitmaker, P. Bass, H.L.L.M. Van Leengoed, F.W. Van Der Meulen, W.M. Star, N. Zandwijk Photodynamic therapy: a promising new modality for the treatment of cancer. J. Photochem. Photobiol.: B. Biol., 34 (1996), 3–12
5. T.N. Castano, M.R. Demidova, Mechanisms in photodynamic therapy: part two – cellular signalling, cell metabolism and modes of cell death. Photodiag. Photodyn. Ther., 2 (2005), 1–23
6. S.B. Brown, E.A. Brown, I. Walker, The present and future role of photodynamic therapy in cancer treatment. Lancet Oncol., 5 (2004), 497–508
7. F.S. De Rosa, M.V.L.B. Bentley, Photodynamic therapy of skin cancers: sensitizers, clinical studies and future directives. Pharm. Res., 17 (2000), 1447–1455
8. B. W. Henderson, T. Dougherty, Photodynamic therapy. J. Photochem. Photobiol., 55 (1), (1992)145-157.
9. A. Juzeniene, J. Moan, The history of PDT in Norway. Part one – identification of basic mechanisms of general PDT. Photodiag. Photodyn. Ther., 4 (2007), 3–11
10. M. Ochsner, Light scattering of human skin: a comparison between zinc(II)-phthalocyanine and photofrin. II J. Photochem. Photobiol.: B. Biol., 32 (1996), 3–9
11. A.P. Castano, T.N. Demidova, M.R. Hamblin, Mechanisms in photodynamic therapy: Part two – photosensitizers, photochemistry and cellular localization. Photodiag. Photodyn. Ther., 1 (2004), 279–293
12. K. Plaetzer, B. Krammer, J. Berlanda, F. Berr, T. Kiesslich, Photophysics and photochemistry of photodynamic therapy: fundamental aspects Laser. Med. Sci., 1 (2008), 1–15
13. N.V. Kudinova, T.T. Berezov, Photodynamic therapy of cancer. Biochem. (Moscow) Suppl. Series B: Biomed. Chem. 4 (2010) 95.

14. T.J. Dougherty, T.S. Mang, Characterization of intratumoral porphyrin following injection of hematoporphyrin derivative. *Photochem. Photobiol.* 46 (1987) 67.
15. D. Kessel, Probing the structure of HPD by fluorescence spectroscopy. *Photochem Photobiol.* 50 (1989), 345.
16. M.R. Detty, S.L. Gibson, S.J. Wagner, Current clinical and preclinical photosensitizers for use in photodynamic therapy. *J Med Chem*, 47 (2004), 3897.
17. R.M. Szeimies, S. Karrer, C. Abels. 9-Acetoxy-2, 7, 12, 17-tetrakis-(beta-methoxyethyl)-porphycene (ATMPn), a novel photosensitizer for photodynamic therapy: uptake kinetics and intracellular localization. *J Photochem Photobiol B*, 34 (1996), 67.
18. V. Kral, J. Davis, A. Andrievsky. Synthesis and biolocalization of water-soluble sapphyrins. *J Med Chem*, 45 (2002), 1073.
19. C. M Allen, R. Langlois, W. M. Sharman,; C.L. Madeleine, J. E.van, Biological activities of phthalocyanines. *Photochem. Photobiol.*, 76 (2002) 208.
20. C. E. Dent, R. P. Linstead, A. R. J. Lowe, Synthesis of substituted phthalocyanines. *Chem Soc.*, (1934) 1033.
21. C.C.L. Eznoff, A.B.P. Lever, Eds., *Phthalocyanines: Properties and Applications*, VCH Publishing, New York 1996.
22. G. T. Byrne, R. P. Linstead, A. R. J. Lowe, Phthalocyanines. *Chem. Soc.* (1934) 1017-1022.
23. H.de Diesbach, E.von der Weid, Phthalocyanines. *Helv. Chim. Acta*, 10 (1927) 886.
24. W. M. Sharman, J. E.van Lier, Synthesis and photodynamic activity of novel asymmetrically substituted fluorinated phthalocyanines. *Bioconj. Chem.*, 16 (2005) 1166.
25. A. Gelir, Y. J. Yılmaz, Polymer nanocomposites. *Phys. Chem. B*, 111 (2006), 478-484.
26. P. J.Gregory, Porphyr. Synthesis of unsymmetrical carboxyphthalocyanine, 4 (2000) 432.
27. Z. G. Gümüş, I. Gürol, E. Musluoğlu, Z. Z. Öztürk, *Sensors and Actuators* 1601203(2011).
28. N. B. Mckeown, *The Porphyrin Handbook* (Kadish, K. M.; Smith, K. M.; Guillard, R., Eds.), Academic Press: Boston, 15, (2003)61.
29. I.Rosenthal, *Photochem. Photobiol.* 53, (1991)859.
30. D.Phillips, *Prog. React. Kinet.* 22, (1997) 175.
31. D. Woehrle, A.Wendt, A. Weitemeyer, J.Stark, W. Spiller, G. Schneider, S. Mueller,U. Michelsen, H. Kliesch, A. Heuermann and A. Ardeschirpur, *Russ. Chem. Bull.* 2071 (1994)

32. D. Woehrle, A. Hirth, T. Bogdahn-Rai, G. Schnurpfeil and M. Shopova, *Russ. Chem. Bull.* 47, (1998) 807.
33. R. Bonnett, *Chem. Soc. Rev.* 24, (1995) 19.
34. Q. Peng and J. Moan, *Br. J. Cancer* 72, (1995) 565.
35. H. L. Van Leengoed, N. van der Veen, A. A. Versteeg, R. Ouellet, J. E. van Lier and W. M. Star, *Photochem. Photobiol.* 58, (1993) 575.
36. Macdonald, I. J.; Dougherty, T. J. *J. Porphyr. Phthalocyan.*, 5 (2001) 105.
37. Boyle, R. W.; Dolphin, D. *Photochem. Photobiol.*, 64 (1996) 469.
38. Selbo, P. K.; Weyergang, A.; Eng, M. S.; Bostad, M.; Mælandsmo, G. M.; Høgset, A.; Berg, K. *Journal of Controlled Release*, 159(2012) 197.
39. N. B. Mckeown, *The Porphyrin Handbook* (Kadish, K. M.; Smith, K. M.; Guillard, R., Eds.), Academic Press: Boston, 15, (2003) 61.
40. Dumoulin, F.; Durmuş, M.; Ahsen, V.; Nyokong, T. *Coordination Chemistry Reviews*, 254, (2010) 2792.
41. I. Booyen, F. Matemadombo, M. Durmus,; T. Nyokong, *Dyes Pigm.*, 89, (2011) 111.
42. N. Masilela, T. Nyokong, *Dyes Pigm.*, 84, (2010) 242.
43. N. Nombona, T. Nyokong, *Dyes Pigm.*, 80, (2009) 130.
44. D. K. Modibane, T. Nyokong, *Polyhedron*, 28, (2009) 1475.
45. P. W. Causey, I. Dubovyk,; C. C. Leznoff, *Can. J. Chem.*, 84(2006) 1380.
46. P. Yiru,; H. Fenghua,; L. Zhipeng,; C. Naisheng,; H. Jinling,; *Inorg. Chem. Commun.*, 7, (2004) 967.
47. B.D. Bezerin, *Coordination Compounds of Porphyrins and Phthalocyanines*, Wiley, J. & Sons, New York, NY, 1981.
48. H. Tomoda, S. Saito, S. Ogawa, S. Shiraishi, *Chem. Lett.* 1980, 1277.
49. H. Tomoda, S. Saito, S. Shiraishi, *Chem. Lett.* 1983, 313.
50. P. A. Barrett,; R. P. Linstead,; G. A. P. Tuey, *J. Chem. Soc.* 1939, 1809.
51. T. J. Hurley, M.A. Robinson, S. I. Trotz, *Inorg. Chem.* 1967, 6, 389.
52. C. C. Leznoff, *Phthalocyanines: Properties and Applications*. Leznoff, C. C.; Lever, A. B. P. Eds.; VCH Publishers (LSK) Ltd.: Cambridge, 1, (1989) 1.

53. J. Britton, C. Litwinski,; M. Durmuş,; V. Chauke,; T. Nyokong, J. Porphyr. Phthalocyanines, 15, (2011) 1239.
54. M. J. Cook,; M. F. Daniel,; K. J. Harrison,; N. B. Mckeown, ; A. J. Thomson, J. Chem. Soc., Chem. Commun. 1 1987, 1086.
55. N. Kobayashi,; N. Sasaki,; Y. Higashi, ; T. Ossa, Inorg. Chem., 34, (1995) 1636.
56. N. B. Mckeown,; I. Chambrier,; M. J. Cook, J. Chem. Soc., Perkin Trans. 1 (1990) 1169.
57. M. J. Cook,; A. J. Dunn,; S. D. Howe,; A. J. Thomson, K. J. Harrison, J. Chem. Soc., Perkin Trans. 1 (1988) 2453.
58. A. Z. Jablonski, Phys. (Zeitschrift für Physik A Hadrons and Nuclei) 1935, 94 (1), 38-48.
59. P. W. Atkins, Physical Chemistry (Atkins, P. W., 6th Eds) Oxford: Oxford University Press (1998) 17.
60. K. Ishii,; N. Kobayashi, The Porphyrin handbook (Guilard, R.; Smith, K. M., Eds.) New York: Elsevier Science, 16, (2003) 102.
61. B. N. Achar,; P. K. Jayasree, Can. J. Chem., 77, (1999)1690.
62. L. Kaestner, M. Cesson, K. Kassab, T. Christensen, P.D. Edminson, M.J. Cook, T. Chambrier, G. Jori, Photochem. Photobiol. Sci., , 2, (2003) 660
63. J. M. Robertson, J. Chem. Soc. (1936) 1195.
64. Y. Li, T. M. Pritchett, J. Huang, M. Ke, P. Shao, W. Sun, J. Phys. Chem. A., 112 (2008) 7200.
65. M. J. Stillman, T. Nyokong, The Porphyrin handbook (Leznoff, C. C., Lever, A. B. P., Eds.) VCH: New York, 1, (1989) 139.
66. A.W. Snow, In The Porphyrin Handbook, Kadish K. M., Smith K. M., Guilard R., Academic Press: San Diego, 17, (2003), 158.
67. S. Fery-Forgues, D. Lavabre, J. Chem. Ed. 76 (1999) 1260.
68. A. Ogunsipe, J. Chen, T. Nyokong, New. J. Chem. 28 (2004) 822.
69. IUPAC Compedium of Chemical Terminology, 2nd edition, (1997): [www.iupac.org/goldbook/L03515.pdf](http://www.iupac.org/goldbook/L03515.pdf).
70. N. Masilela, T. Nyokong, J. Photochem. Photobiol. A: Chem. 223 (2011) 124.
71. K. Ishii, N. Kobayashi, In The Porphyrin Handbook, K.M. Kadish, K.M. Smith, R. Guilard, (Eds.), Elsevier Science, New York, Vol. 16 (2003) Chapter 102.



72. J. Turro, In *Modern Molecular Photochemistry*, The Benjamin/Cummings Publishing Co., Inc., New York (1978).
73. P. Kubat, J. Mosinger, J. Photochem. Photobiol. A: Chem. 96 (1993) 93.
74. W. Chidawanyika, T. Nyokong, J. Photochem. Photobiol. A: Chem. 206 (2009) 169.
75. P. B. Merkel, D. R. Kearns, J. Am. Chem. Soc. 97 (1989) 833.
76. R. Bonnett, in *Chemical Aspects of Photodynamic Therapy*, D. Phillips (Ed.), Gordon and Breach Science, Canada, (2000).
77. S. Nagarajan, Z. Yong Use of core/shell structured nanoparticles for biomedical applications, 1 (2008) 34.
78. L.S. Goldstein, M.W. Dewhirst, M. Repacholi, L. Kheifets Summary, conclusions and recommendations: adverse temperature levels in the human body *Int. J. Hyperther.*, 19 (2003), 373.
79. G.V. Loo, X. Saelens, M.V. Gulp, M. MacFarlane, S.J. Martin, P. Vandenabeele The role of mitochondrial factors in apoptosis: a Russian roulette with more than one bullet *Cell Death Differ.*, 9 (2002), 1031.
80. G.P. Raaphorst, M.L. Freeman, W.C. Dewey Radiosensitivity and recovery from radiation damage in cultured CHO cells exposed to hyperthermia at 42.5 or 45.0 °C *Radiat. Res.*, 79 (1979), 390.
81. R.W.Y. Habash, R. Bansal, D. Krewski, H. Alhafid Thermal therapy, part 2: hyperthermia techniques *Crit. Rev. Biomed. Eng.*, 34 (2006), 491.
82. R.K. Gilchrist, R. Medal, W.D. Shorey, R.C. Hanselman, J.C. Parrott, C.B. Taylor Selective inductive heating of lymph nodes *Ann. Surg.*, 146 (1957), 596.
83. D. H. Reneker, I. Chun, *Nanotechnology*, 7 (1996) 216.
84. R.W. Rand, H.D. Snow, D.G. Elliott, G.M. Haskins, Induction heating method for use in causing necrosis of neoplasm, US Patent Specification, 545 (1985) 368.
85. A. Ito, H. Honda, T. Kobayashi Cancer immunotherapy based on intracellular hyperthermia using magnetite nanoparticles: a novel concept of "heat-controlled necrosis" with heat shock protein expression *Cancer Immunol. Immunother.*, 55 (2006), 320.

86. M. Faraji, Y. Yamini, M. Rezaee Magnetic nanoparticles: synthesis, stabilization, functionalization, characterization, and applications *J. Iran. Chem. Soc.*, 7 (2010), 1.
87. I. Brigger, C. Dubernet, P. Couvreur Nanoparticles in cancer therapy and diagnosis *Adv. Drug Deliv. Rev.*, 54 (2002), 631.
88. D. Bahadur, J. Giri Biomaterials and magnetism *Sadhana*, 28 (2003), pp. 639–656
89. A. Ito, M. Shinkai, H. Honda, T. Kobayashi Medical application of functionalized magnetic nanoparticles *J. Biosci. Bioeng.*, 100 (2005), 1.
90. L. Zonghuan, P.D. Malcolm, G. Zhanhu, G.O. Vladimir, C.S.S.R. Kumar, L.M. Yuri Magnetic switch of permeability for polyelectrolyte microcapsules embedded with nanoparticles *Langmuir*, 21 (2005), 2042.
91. S. Aime, W. Dastrù, R. Gobetto, D. Santelia, A. Viale, Agents for polarization enhancement in MRI, *Handbook of Experimental Pharmacology 185/I*, Springer-Verlag Heidelberg, Berlin, (2008), 247.
92. L. Schröder, Xenon for NMR biosensing—inert but alert, *Physica Med.* 29 (2013) 3.
93. P. Caravan, J.J. Ellison, T.J. McMurry, R.B. Lauffer, Gadolinium (III) chelates as MRI contrast agents: structure, dynamics, and applications, *Chem. Rev.* 99 (1999) 2293.
94. M.M. Lin, D.K. Kim, A.J. El Haj, J. Dobson, Development of superparamagnetic iron oxide nanoparticles (SPIONS) for translation to clinical applications, *IEEE Nanobioscience* 7 (2008) 298.
95. J. Dobson, Magnetic nano particles for drug delivery, *Dev. Res.* 67 (2006) 55.
96. A.K. Gupta, M. Gupta, Synthesis and surface engineering of iron oxide nanoparticles for biomedical applications, *Biomaterials* 26 (2005) 3995.
97. D. Kozłowska, P. Foran, P. MacMahon, M.J. Shelly, S. Eustace, R. O'Kennedy, Molecular and magnetic resonance imaging: the value of immunoliposomes, *Adv. Drug Deliv. Rev.* 61 (2009) 1402.
98. S. Lee, J. Xie, X. Chen, Activatable molecular probes for cancer imaging, *Curr. Top. Med. Chem.* 10 (2010) 1135.

99. G.M. Lanza, P.M. Winter, A.M. Neubauer, S.D. Caruthers, F.D. Hockett, S.A. Wickline, 1 H/ 19 F Magnetic resonance molecular imaging with perfluorocarbon nanoparticles, *Curr. Top. Dev. Biol.* 70 (2005) 57.
100. S. Lee, K. Park, K. Kim, K. Choi, L.C. Kwon, Activatable imaging probes with amplified fluorescent signals, *Chem. Commun.* 36 (2008) 4250.
101. C. Bouzigues, T. Gacoin, A. Alexandrou, Biological applications of rare-earth based nanoparticles, *Am. Chem. Soc.* 5 (2011) 8488.
102. M. Longmire, P.L. Choyke, H. Kobayashi, Dendrimer-based contrast agents for molecular imaging, *Curr. Top. Med. Chem.* 8 (2008) 1180.
103. P.M. Winter, S.D. Caruthers, Molecular imaging of angiogenesis in nascent Vx-2 rabbit tumors using a novel alpha(nu)beta3-targeted nanoparticle and 1.5 tesla magnetic resonance imaging, *Cancer Res.* 63 (2003) 5838.
104. T. Ivanusă, K. Beravs, J. Medič, I. Sersă, G. Sersă, V. Jevtič, F. Demsar, U. Mikac, Dynamic contrast enhanced MRI of mouse fibrosarcoma using small-molecular and novel macromolecular contrast agents, *Phys. Med.* 23 (2007) 85.
105. Y.W. Jun, J.S. Choi, J. Cheon, Heterostructured magnetic nanoparticles: their versatility and high performance capabilities, *Chem. Commun.* 12 (2007) 1203.
106. P. Karandikar, M. Agashe, K. Vijayamohan and A. J. Chandwadkar, *Appl. Catal., A: Gen.*, 257 (2004) 133
107. B. B. Pluska, I. Szymczyk and H. Abramczyk, *J. Mol. Struct.*, (2005) 744.
108. F. Raimondi, G. G. Scherer, R. Kotz and A. Wokaun, *Angew. Chem.*, 117 (2005)2228
109. C. Freire, C. Pereira and S. Rebelo, *Catalysis*, 24 (2012) 116
110. B. R. Vaddula, A. Saha, J. Leazer and R. S. Varma, *Green Chem.*, 14 (2012) 2133
111. Z. Zhao, Y. Han, C. Lin, D. Hu, F. Wang, X. Chen, Z. Chen and N. Zheng, Multifunctional Core–Shell Upconverting Nanoparticles for Imaging and Photodynamic Therapy of Liver Cancer Cells, *Chem as Journ*, 7 (2012) 830.
112. P. Modisha. E. Antunes, J. Mack, T. Nyokong, Improvement of the photophysical parameters of zinc octacarboxy phthalocyanine upon conjugation to magnetic nanoparticles, *Int. J. Nanosci.*12 (2013) 1350010.

113. X. Chen, J. Zou, L. Liu, Y. Zhang, J., Preparation of magnetic silica nanoparticle-supported iron tetra-carboxyl phthalocyanine catalyst and its photocatalytic properties. (2010) 64552.
114. M Goldys, K Drozdowicz-Tomsia, S Jinjun, D Dosev, IM Kennedy, S Yatsunencko, M Godlewski J Am Chem Soc 128 (2006) 14498
115. H Guo, N Dong, M Yin, WP Zhang, LR Lou, SD Xia J Phys Chem B 108 (2004) 19205
116. XY Chen, E Ma, GK Liu, M Yin J Phys Chem C 111 (2007) 9638
117. S Okamoto, H Kobayashi, H Yamamoto J Appl Phys 86 (1999) 5594
118. T Danger, A Bleckmann, G Huber Appl Phys B Lasers Opt 58 (1994) 413
119. R. M. Petoral, Jr., F. Söderlind, A. Klasson, A. Suska, M. A. Fortin, N. Abrikosova, L. Selegård, P.-O. Käll, M. Engström and K. Uvdal, J. Phys. Chem. C, , 113, (2009) 6913.
120. Toth E, Bolskar RD, Borel A, Gonzalez G, Helm L, Merbach AE, Sitharaman B, Wilson LJ Water-soluble gadofullerenes: toward high-relaxivity, pH-responsive MRI contrast agents. J Am Chem Soc 127 (2005) 799.
121. Zhang J, Fatouros PP, Shu C, Reid J, Owens LS, Cai T, Gibson HW, Long GL, Corwin FD, Chen Z-J, Dorn HC High relaxivity trimetallic nitride (Gd<sub>3</sub>N) metallofullerenes MRI contrast agents with optimized functionality. Bioconjug Chem 21 (2010) 610.
122. Bolskar RD, Benedetto AF, Husebo LO, Price RE, Jackson EF, Wallace S, Wilson LJ, Alford JM First soluble M@C<sub>60</sub> derivatives provide enhanced access to metallofullerenes and permit in vivo evaluation of Gd@C<sub>60</sub> [C(COOH)<sub>2</sub>]<sub>10</sub> as a MRI contrast agent. J Am Chem Soc 125 (2003) 5471.
123. Zhang X, Ballem MA, Ahre'n M, Suska A, Bergman P, Uvdal Nanoscale Ln(III)-carboxylate coordination polymers (Ln = Gd, Eu, Yb): temperature-controlled guest encapsulation and light harvesting. J Am Chem Soc 132 (2010) 10391.
124. Skotland T, Iversen T-G, Sandvig K New metal-based nanoparticles for intravenous use: requirements for clinical success with focus on medical imaging. Nanomedicine NBM 6 (2010) 730.
125. JL Bridot, AC Faure, S Laurent, C Riviere, C Billotey, B Hiba, M Janier, V Josserand, JL Coll, L Vander Elst, R Muller, S Roux, P Perriat, O Tillement Hybrid gadolinium oxide nanoparticles: multimodal contrast agents for in vivo imaging. J Am Chem Soc 129 (2007) 5076.

126. M-A Fortin, RM Petoral Jr, F So"derlind, A Klasson, mM Engstro", T Veres, P-O Ka"ll, K Uvdal Polyethylene glycol-covered ultra-small Gd<sub>2</sub>O<sub>3</sub> nanoparticles for positive contrast at 1.5 T magnetic resonance clinical scanning. *Nanotechnology* 18 (2007) 395501
127. MA McDonald, KL Watkin Investigations into the physicochemical properties of dextran small particulate gadolinium oxide nanoparticles. *Acad Radiol* 13 (2006) 421.
128. F Evanics, PR Diamente, FCJM van Veggel, GJ Stanis, RS Prosser Water-soluble GdF<sub>3</sub> and GdF<sub>3</sub>/LaF<sub>3</sub> nanoparticles-physical characterization and NMR relaxation properties. *Chem Mater* 18 (2006) 2499.
129. J Drbohlavova, R Hrdy, V Adam, R Kizek, O Schneeweiss, J Hubalek. Preparation and Properties of Various Magnetic Nanoparticles. *Sensors* 9 (2009) 2352.
130. S Santra, RP Bagwe, D Dutta, JT Stanley, GA Walter, W Tan, MB Moudgil, RA Maricle. Synthesis ND Characterization of Fluorescent, Radio-Opaque, and Paramagnetic Silica Nanoparticles for Multimodal Bioimaging Applications. *Adv. Mater* 17 (2005) 2165.
131. T Ann. Nanoparticles in Photodynamic Therapy. *Nano Biomed Eng* 3 (2) (2011) 137.
132. S. Mornet, S. Vasseur, F. Grasset, E. Duguet, J. Mater. Chem., 14 (2004) 2161.
133. J. C. Love, L. A. Estroff, J. K. Kriebel, R. G. Nuzzo, G. M. Whitesides, *Chem Rev.*, 105 (2005) 1103.
134. K. S. Shin, Y. K. Cho, J. Choi, K. Kim, *Appl. Catal. A: Gen.*, 413 (2012) 170.
135. H Dougherty, H Dougherty, CJ Gomer, G Jori, D Kessel, M Kerbelik. Photodynamic Therapy. *Natl Cancer Inst* 90 (1998) 889.
136. S. Tombe, E. Antunes, T. Nyokong. Electrospun fibers functionalized with phthalocyanine-gold nanoparticle conjugates for photocatalytic applications. 371 (2013) 125.
137. Y. Song, Z. He, F. Xu, H. Hou, L. Wang, pH-controlled electrocatalysis of amino acid based on electrospun cobalt nanoparticles-loaded carbon nanofibers. 166 (2012) 357.
138. J. Zeleny, *Physical reviews*, 3 (1914) 69.
139. D. H. Reneker, I. Chun, *Nanotechnology*, 7 (1996) 216.
140. P. Supaphol, C. Uppatham, M. Anakul, *J. Polym. Sci. B: Polym. Phys.*, 43 (2005) 3699.

141. S. De Vrieze, B. De Schoenmaker, o. Ceylan, J. Depuydt, I. Van Landuyt, H. Rahier, G. Assohe, K. De Clerck. Morphological study of steady state electrospun polyamide-6 nanofibres., 199 (2011) 2984.
142. R. Zügler, C. Litwisky, N. Torto, T. Nyokong. *New J. Chem.*, 35 (2011) 1588.
143. Christie R.M., *Colour Chemistry*. The Royal Society of Chemistry, Cambridge (UK) (2001)
144. C. Zhu, L. Wang, L. Kong, X. Yang, L. Wang, S. Zheng, F. Chen, F. Maizhi, H. Zong, *Chemosphere*, 41 (2000) 303
145. K.-T. Chung, G.E. Fulk, A.W. Andrews, *Appl. Environ. Microbiol.*, 42 (1981) 641
146. J. Mosinger, K. Lang, P. Kubát, J. Sýkora, M. Hof, L. Píšťil, B. Mosinger Jr., *J. Fluorec.*, 19 (2009) 709.
147. S. Tang, C. Shao, Y. Li, R. Mu, *J. Phys. Chem. Solids*, 68 (2007) 2337.
148. R. Zügler, T Nyokong, *J. Mol. Cat. A: Cem.*, 358 (2012) 49.
149. Y. Filatov,. A. Budyka,. V. Kirichenko,.*Electrospinning of micro- and nanofibers: fundamentals and applications in separation and filtration processes*, Begell House Inc., New York, USA, (2007).
150. S. Lee,. S. K. Obendorf, *Use of Electrospun Nanofiber Web for Protective Textile Materials as Barriers to Liquid Penetration. Textile Research Journal*77 , 9 (2007)'696.
151. Christie R.M., *Colour Chemistry*. The Royal Society of Chemistry, Cambridge (UK) (2001)
152. C. Zhu, L. Wang, L. Kong, X. Yang, L. Wang, S. Zheng, F. Chen, F. Maizhi, H. Zong, *Chemosphere*, 41 (2000) 303
153. K.-T. Chung, G.E. Fulk, A.W. Andrews, *Appl. Environ. Microbiol.*, 42 (1981)641
154. H.M. Pinheiro, E. Touraud, O. Thomas, *Dyes Pigm.*, 61 (2004) 121
155. F. Sosath, *Biologisch-chemische Behandlung von Abwässern der Textilveredelung mit Reaktivfarbstoffen*, VDI Fortschrittsberichte, Reihe Umweltverfahrenstechnik, (1999) 209
156. N. Daneshvar, H. Ashassi-Sorkhabi, A. Tizbar, *Sep. Purif. Technol.*, 31 (2003)153
157. Y.M. Slokar, A.M.L. Marechal, *Dyes. Pigm.*, 335 (1998) 220
158. C. Galindo, P. Jacques, A. Kalt, *Chemosphere*, , 48 (2002) 1047
159. S. Saranaik, P. Kanekar,.*J. Appl. Bacteriol.*79 (1995) 459.
160. M. Pera-Titus, V. Garcia-Molina, M.A. Banos, *Appl. Catal. B: Environ.*, 47 (2004) 219.

161. A. Özcan, M.A. Oturan, N. Oturan, Y. Sahin, J. Hazard. Mater.,163 (2009) 1213.
162. H. T. Gomes, S. M. Miranda, M. J. Sampaio, A. M. T. Silva, J. L. Faria, Catal. Today, 15 (2010) 153.
163. M. Koch, A. Yediler, D. Lienert, G. Insel, A. Kettrup, Chemosphere, 46 (2002) 109.
164. N. Daneshvar, A. Oladegaragoze, N. Djafarzadeh, J. Hazard. Mater.,129 (2006) 116.

# **Chapter 2**

## **Experimental**

Incorporated in this chapter are all the experimental procedures used during the course of this thesis, including the methods of characterization for the nanoparticles, phthalocyanine, conjugates and nanofibers employed in this work.



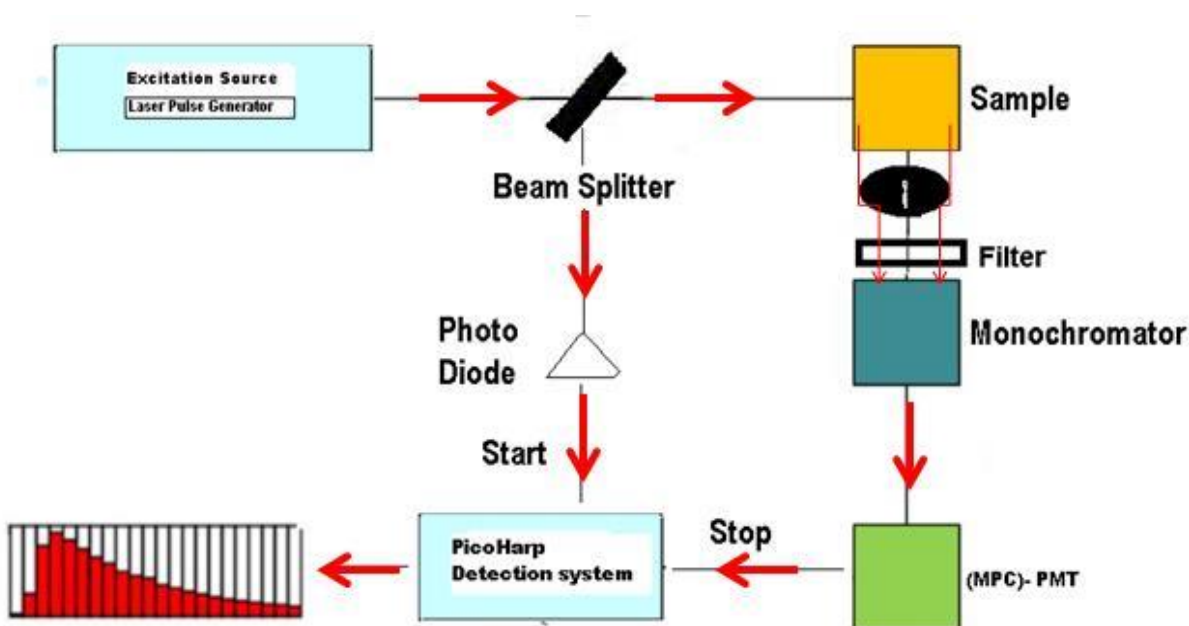
## 2.1 Solvents and Reagents

Dimethylsulphoxide (DMSO), ethanol (EtOH), dimethylformamide (DMF), methanol (MeOH) and toluene were obtained from SAARChem. Water collected from a Milli-Q water purification system (Millipore Corp., Bedford, MA, USA) was used for the preparation of all aqueous solutions. 1,3-diphenylisobenzofuran (DPBF), Anthracene-9, 10-bis-methylmalonate (ADMA), N,N'-dicyclohexylcarbodiimide(DCC), sodium hydroxide (NaOH) pellets, polyethylene glycol (PEG), (3-aminopropyl)triethoxysilane (APTES, 99 %), Acetic acid (98 %), formic acid (99.8 %), Gadolinium nitrate hexahydrate (99.99 %), Orange G (OG) and N-hydroxysuccinimide (NHS) were purchased from Sigma-Aldrich. Polyamide-6 Ultramid® B grades (i.e., B24, B27, B32 and B36) were supplied by BASF. The average molecular weights in grams per mole are: 70,000, 80,000, 90,000 and 10, 000 for B24, B27, B32 and B36, respectively.

## 2.2 Instrumentation

1. UV-Vis absorption spectra were measured at room temperature on a Shimadzu UV-2550 spectrophotometer using a 1 cm pathlength cuvette for the solution studies.
2. Infrared (FTIR) spectra were recorded using a Perkin-Elmer 100 FTIR Spectrometer equipped with a Universal Attenuated Total Reflectance (ATR) sampling accessory.
3. Fluorescence emission and excitation spectra were obtained on a Varian Eclipse spectrofluorimeter using a 1 cm pathlength quartz cuvette.
4. Fluorescence lifetimes were measured using a time correlated single photon counting setup (TCSPC) (FluoTime 200, Picoquant GmbH), Scheme 2.1. The fluorescence lifetime of the phthalocyanine and its conjugates were determined using a diode laser (LDH-P-670 with PDL 800-B, Picoquant GmbH, 670 nm, 20 MHz repetition rate, 44 ps pulse width). Fluorescence was detected under the magic angle with a Peltier cooled photomultiplier tube (PMT) (PMA-C 192-N-M, Picoquant) and integrated electronics (PicoHarp 300E, Picoquant GmbH). A monochromator with a spectral width of about 4 nm was used to select the required emission

wavelength band. The response function of the system, which was measured with a scattering Ludox solution (DuPont), had a full width at half-maximum (FWHM) of 300 ps. All luminescence decay curves were measured at the maximum of the emission peak and lifetimes were obtained by deconvolution of the decay curves using the FLUOFIT software program (PicoQuant GmbH, Germany). The support plane approach was used to estimate the errors of the decay times.



**Scheme 2.1: Schematic diagram for the TCSPC spectrometer.**

5. Laser flash photolysis experiments (shown in Scheme 2.2) were performed with the light pulses produced by a Quanta-Ray Nd: YAG laser providing 400 mJ, 90 ns pulses of laser light at 10 Hz, pumping a Lambda -Physik FL3002 dye (Pyridin 1 dye in methanol). The energy of a single pulse ranged from 2 to 7 mJ. The analyzing beam source was from a Thermo Oriel xenon arc lamp and a photomultiplier tube was used as a detector. Signals were recorded with a digital real-time oscilloscope (Tektronix TDS 360); the kinetic curves were averaged over 256 laser pulses.

6. Photo-irradiation for photodegradation or singlet oxygen determinations were performed using a General Electric Quartz line lamp (300 W). A 600 nm glass cut off filter (Schott) and water filters were used to filter off ultraviolet and infrared radiations, respectively. An interference filter (Intor, 670 nm filter with a band width of 20 nm, or a 700 nm filter with a band width of 40 nm depending on the Q-band maxima of the Pc) was additionally placed in the light path before the sample (Scheme 2.3). Light intensity was measured with a POWER MAX5100 (Molelectron Detector Incorporated) power meter and found to be  $3.2 \times 10^{20}$  photons  $\text{cm}^{-2} \cdot \text{s}^{-1}$  for the photodegradation studies and  $1.3 \times 10^{19}$  photons  $\text{cm}^{-2} \cdot \text{s}^{-1}$  for the singlet oxygen studies.
7. Scanning Electron Microscopy (SEM) was used to analyse the morphology of the electrospun nanofibers using a JOEL JSM 840 SEM at an accelerating voltage of 20 kV. The average fiber diameter and their standard deviations were based on 70 measurements, using the Cell D software from Olympus.
8. Energy dispersive X-ray spectroscopy (EDX) was carried out using a INCA PENTA FET coupled to the VAGA TESCAME using 20 kV accelerating voltage.
9. Transmission electron microscopy (TEM) images were obtained using a ZEISS LIBRA<sup>®</sup> TEM and the sizes determined using ImageJ software.
10. X-ray powder diffraction (XRD) patterns were recorded on a Bruker D8 Discover equipped with a LynxEye detector, using Cu-K $\alpha$  radiation ( $\lambda = 1.5405 \text{ \AA}$ , nickel filter). Data were collected in the range from  $2\theta = 5^\circ$  to  $60^\circ$ , scanning at  $1^\circ \text{ min}^{-1}$  with a filter time-constant of 2.5 s per step and a slit width of 6.0 mm. Samples were placed on a zero background silicon wafer slide. The X-ray diffraction data were treated using the Eva (evaluation curve fitting) software. Baseline correction was performed on each diffraction pattern, while the full-width at half-maximum values from the fitted curves were used to determine the nanoparticle size (if possible) in this study.
11. X-ray photoelectron spectroscopy (XPS) was done using a Kratos Axis Ultra DLD, using an Al (monochromatic) anode, equipped with a charge neutralizer, while the operating pressure was kept below  $5 \times 10^{-9}$  torr. For survey XPS scans, the following parameters were used: emission current was kept at 5 mA, the anode (HT) voltage at 15kV, and the resolution at 160

eV pass energy using a hybrid lens in the slot mode. The step size used was at 1 eV, while the dwell times were kept at 300 ms. The high resolution spectra were obtained at pass energy of 40 eV, also in slot mode with the dwell times and step sizes at 500 ms and 0.1 eV, respectively

12. The thermal degradation properties of the Polyamide (PA), functionalized PA fibers and individual components were studied using a Simultaneous DTA-TG (Shimadzu) thermal analyzer (TA 60WS, Shimadzu) at a heating rate of 10 °C/min to 500 °C under a nitrogen atmosphere with a gas flow rate of 120 ml/min.
13. An X band EMX<sup>plus</sup> Bruker Electron Paramagnetic Resonance (EPR) Spectrometer was employed where the first derivative signal was obtained in solid state for the Gd<sub>2</sub>O<sub>3</sub> NPs, Si-Gd<sub>2</sub>O<sub>3</sub> NPs and their conjugates with ZnTCPPc.
14. Polymer solution viscosity and conductivity measurements were carried out using a rotating Brookfield Viscometer LVDV-II and a CDM-210 conductivity meter (Radiometer Analytical). The electrospinning set-up consisted of an infusion pump (KD Scientific Syringe Pump Series 100) which was used to pump out a solution held in a 20 ml plastic syringe fitted with a needle (dimensions: 1.024 mm × 15.24 cm). A high-voltage source (Glassman High Voltage Series EH) was used to generate an electric field between the needle tip and a grounded collector.

## 2.3 Methods

### 2.3.1 Fluorescence quantum yields ( $\Phi_F$ ) and lifetimes ( $\tau_F$ )

The fluorescence spectra of the synthesised Pcs together with the zinc phthalocyanine (ZnPc) standard, were prepared such that the absorbance of each, at their respective excitation wavelength, was  $\sim 0.05$ . Due to differences in solubility, the emission spectra of the Pcs and ZnPc standard were measured in different solvents. However, the differences in refractive indices were corrected and the area under the emission curves measured to calculate the fluorescence quantum yields using equation 1.1. The ZnPc standard was measured in DMSO ( $\Phi_F = 0.20$ ) [1].

$$\Phi_F = \frac{F \cdot A_{\text{std}} \cdot n^2}{F_{\text{std}} \cdot A \cdot n_{\text{std}}^2} \Phi_F^{\text{std}} \quad (1.1)$$

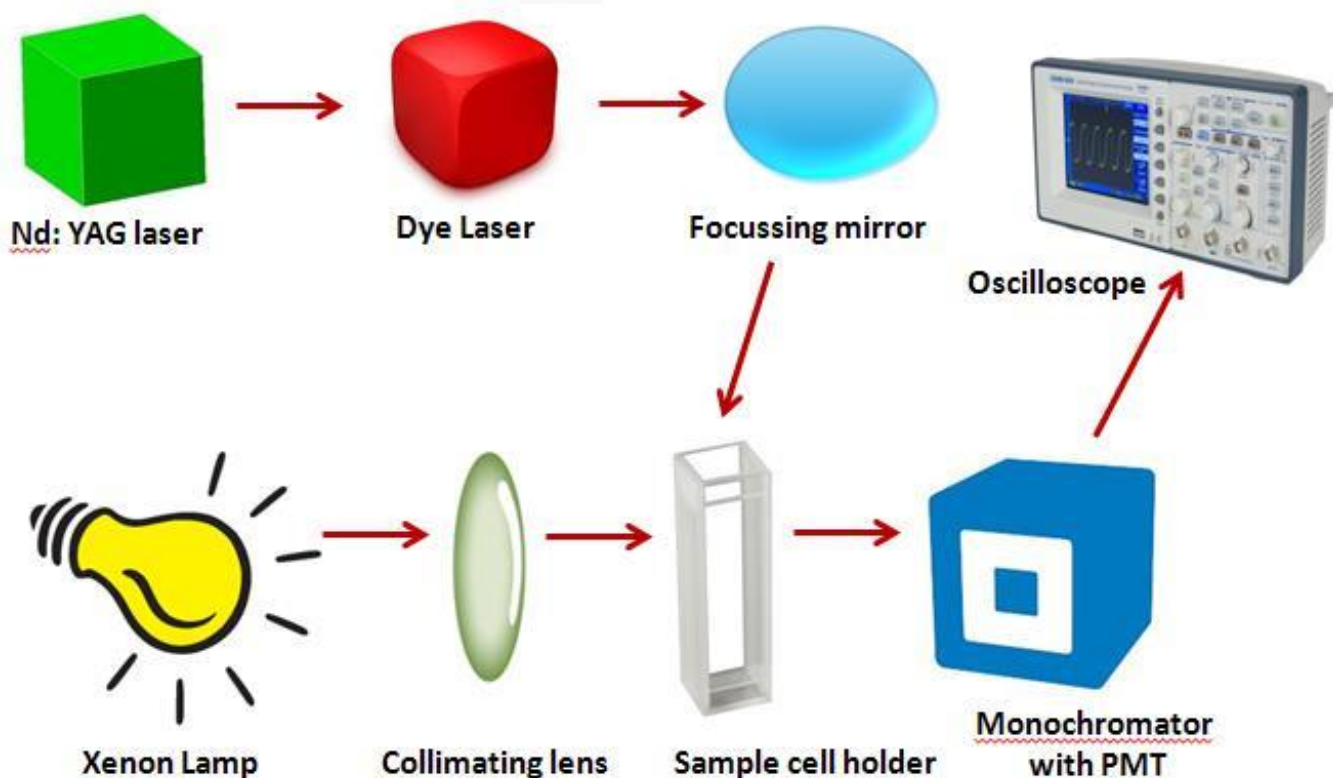
where  $F$  and  $F_{\text{std}}$  are the areas under the fluorescence curves of the sample and the standard respectively.  $A$  and  $A_{\text{std}}$  are the respective absorbances of the sample and the standard at the excitation wavelength and  $n$  and  $n_{\text{std}}$  are the refractive indices of the solvents used for the sample and standard respectively.

The fluorescence lifetime,  $\tau_F$ , of an excited species is the time needed for a concentration of the excited species to decay to  $1/e$  or  $\sim 37\%$ , of its original value [2]. The  $\tau_F$  is related to the radiative lifetime,  $\tau_0$ , and is defined by equation 1.2.

$$\Phi_F = \frac{\tau_F}{\tau_0} \quad (1.2)$$

### 2.3.2 Triplet quantum yields and lifetimes

Triplet quantum yields ( $\Phi_T$ ) and lifetimes ( $\tau_T$ ) were determined by a laser flash photolysis set-up (Scheme 2.2).



**Scheme 2.2: Schematic representation of a laser flash photolysis set-up**

The concentration of the argon saturated solutions of each of the samples under investigation, as well as an unsubstituted ZnPc (standard), was adjusted to an absorbance of  $\sim 1.5$  and introduced into a 1 cm path length spectrophotometric cell. The samples were then irradiated at the wavelength where the Q-band of the sample and standard solutions intersect. The triplet quantum yields of the samples were determined using equation 1.3 with ZnPc in DMSO ( $\Phi_T = 0.65$ ) [3]. The triplet lifetimes were determined by the exponential fitting of the triplet decay curves using OriginPro 7.5 or 8.0 software.

$$\Phi_T = \Phi_T^{std} \frac{\Delta A_T \cdot \epsilon_T^{std}}{\Delta A_T^{std} \cdot \epsilon_T} \quad (1.3)$$

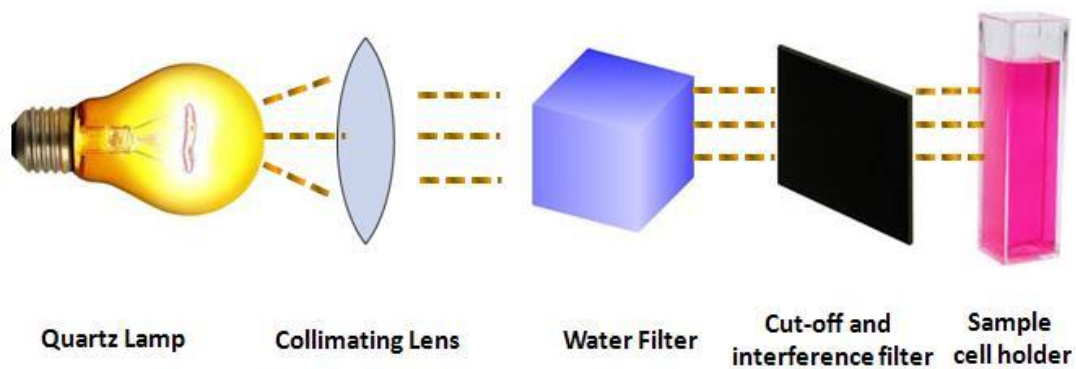
where  $\Delta A_T$  and  $\Delta A_T^{std}$  are the changes in the triplet state absorbances of the Pc derivative and the standard respectively;  $\epsilon^T$  and  $\epsilon_T^{std}$ , the triplet state molar extinction coefficients for the Pc derivative and the standard respectively;  $\Phi_T^{std}$  the triplet quantum yield for the standard e.g. ZnPc.  $\epsilon^T$  and  $\epsilon_T^{std}$  are determined from the molar extinction coefficients of their respective ground singlet states ( $\epsilon_s$  and  $\epsilon_s^{std}$ ), the changes in absorbances of the ground singlet states ( $\Delta A_s$  and  $\Delta A_s^{std}$ ) and changes in the triplet state absorption, ( $\Delta A_T$  and  $\Delta A_T^{std}$ ) according to Equations 2.1a and 2.1b:

$$\epsilon_T = \epsilon_s \frac{\Delta A_T}{\Delta A_s} \quad (2.1a)$$

$$\epsilon_T^{std} = \epsilon_s^{std} \frac{\Delta A_T^{std}}{\Delta A_s^{std}} \quad (2.1b)$$

### 2.3.3 Singlet oxygen quantum yields ( $\Phi_\Delta$ )

The singlet oxygen quantum yield ( $\Phi_\Delta$ ) determinations for the various phthalocyanine samples were recorded using a set-up as shown in Scheme 2.3.



**Scheme 2.3 Schematic representation of a photochemical set-up.**

The studies were carried out in air using a 2 mL solution of the phthalocyanine or conjugate sample mixed with a singlet oxygen chemical quencher 1,3-diphenylisobenzofuran (DPBF in organic solvents or Anthracene-9,10-bis-methylmalonate (ADMA) in aqueous media for the samples embedded in fiber). The photochemical reaction was executed in a 1 cm path length spectrophotometric quartz cell fitted which had a tight-fitting stopper and the sample then photolysed at the Q-band region using a 300 W General Electric quartz lamp, as described in section 2.2. The light intensity reaching the reaction vessel was calculated to be  $\sim 1.3 \times 10^{19}$  photons.cm<sup>-2</sup>.s<sup>-1</sup>. Singlet oxygen quantum yield values were determined (using equation 1.4) by monitoring the decrease in absorbance of ADMA at 380 nm in aqueous media, or DPBF at 414 or 415 nm in DMSO, with time. To avoid chain reactions, the concentrations of DPBF were kept at  $\sim 6 \times 10^{-5}$  mol.dm<sup>-3</sup>. ZnPc was employed as a standard in DMSO ( $\Phi = 0.67$  [4]).

$$\Phi_{\Delta} = \Phi_{\Delta}^{\text{std}} \frac{R \cdot I_{\text{abs}}^{\text{std}}}{R^{\text{std}} \cdot I_{\text{abs}}} \quad (1.4)$$

where  $\Phi^{\text{std}}$  is the singlet oxygen quantum yield for the standard (ZnPc,  $\Phi^{\text{std}} = 0.67$  in DMSO [4]), R and R<sup>std</sup> are the DPBF photobleaching rates in the presence of the respective MPC conjugates under investigation and the standard respectively. I<sub>abs</sub> and I<sub>abs</sub><sup>std</sup> are the rates of light absorption by the MPCs

The irradiation experiments were carried out using the photolysis setup described in Scheme 2.3.



## 2.4 Synthesis

### 2.4.1 Synthesis of uncoated/bare gadolinium oxide nanoparticles (1) Scheme 3.1 (step 1)

The method for the synthesis of the uncoated or bare gadolinium oxide nanoparticles (**1**, Gd<sub>2</sub>O<sub>3</sub>NPs) was carried out as reported by Bazzi *et. al.* [5] with slight modification as follows: Firstly, 1 g (2.7 mmol) of the Gd(NO<sub>3</sub>)<sub>3</sub> salt instead of GdCl<sub>3</sub>•6H<sub>2</sub>O was placed in 20 ml of PEG whereas Bazzi et al. used diethylene glycol, as a capping agent, at 60°C under vigorous stirring overnight under an argon atmosphere. The temperature was decreased from 140° to 60° in order to control the assembling of the nanoparticles and exclude any aggregation. An aqueous solution of NaOH (2 M, 1 ml) was added dropwise to the reaction flask after which the temperature was raised to 140 °C for 1 h and subsequently increased to 180 °C for a further 4 h. The resulting product was precipitated with ethanol, centrifuged and washed a further 3 times with ethanol. The Gd<sub>2</sub>O<sub>3</sub>NPs (**1**) were successfully synthesised and were dispersed in ethanol (10 ml) and stored for further use. Yield=~2.0 g

### 2.4.2 Silica coated Gd<sub>2</sub>O<sub>3</sub>nanoparticles (2) Scheme 3.1 (step 2)

Following the method of Bazzi *et. al.* [5], dried, uncoated Gd<sub>2</sub>O<sub>3</sub>NPs (**1**, 0.25 mg) were washed 3 times with toluene, air-dried and suspended in a solvent mixture of DMF (12 ml) and toluene (8 ml). APTES (1 ml, 4.27 mmol) was added dropwise and the mixture stirred for 24 h at room temperature under an argon atmosphere. The resultant product was separated out by centrifugation and washed 4 times with toluene and thereafter stored in toluene (10 mL) until further use. The silica coated Gd<sub>2</sub>O<sub>3</sub>NPs are represented as SiGd<sub>2</sub>O<sub>3</sub>NPs (**2**). Yield: 3.0 g.

### 2.4.3 ZnTCPPc (3) Scheme 3.2

Zinc tetracarboxyphenoxy phthalocyanine (ZnTCPPc, complex **3**) was synthesized as reported before [6]. The method followed a synthesis using 4-nitrophthalonitrile and 4-(3,4-dicyanophenoxy)benzoic acid which were also synthesised according to literature methods [6].

UV/Vis:  $\lambda_{\max}$  nm (log  $\epsilon$ ): 349 (4.8) 678 (5.2) FTIR  $\text{cm}^{-1}$ : 3430(O-H), 3134(C-H), 2969 (carboxylic acid OH), 1640 (C=O) 1581(C=C), 1345, 1337, 1131, 840, 748 (CH).

### 2.4.4 ZnTCPPc- Gd<sub>2</sub>O<sub>3</sub> NPs (conj) conjugate (4) Scheme 3.2

ZnTCPPc (**3**) (0.1 g, 0.092 mmol) was firstly added to DCC (1.03 g, 5 mmol) in DMSO (2 ml) and stirred at room temperature for 12 h to activate the carboxylic acid functional groups on the Pc. Thereafter NHS (0.58 g, 5 mmol) and the silica-coated Gd<sub>2</sub>O<sub>3</sub> (SiGd<sub>2</sub>O<sub>3</sub>,**2**) (0.4 g) were sequentially added to the mixture, followed by stirring for 48 h. The product was purified using gravity silica column chromatography with ethanol and toluene as eluents, to separate the free pc and the gadolinium oxide nanoparticles from the conjugate (**4**). Yield: 1.35g.

### 2.4.5 ZnTCPPc- Gd<sub>2</sub>O<sub>3</sub> NPs (mixed) (5)

In addition to the conjugate (**4**) formed, ZnTCPPc (**3**) (0.2 g, 1.84 mmol) was also simply added to the silica-coated Gd<sub>2</sub>O<sub>3</sub> (SiGd<sub>2</sub>O<sub>3</sub>,**2**) (0.4 g) and stirred in DMSO (2 ml) for 48 hrs and centrifuged and the precipitate collected. This produced a sample that contained no covalent bond and is represented as ZnTCPPc-SiGd<sub>2</sub>O<sub>3</sub> NPs (mixed, **5**). Yield: 2. 5g.

## 2.5. Electrospinning methods

### 2.5.1 Polyamide fibers

Four fiber spinning grades of polyamide-6 were supplied. The weight-average molecular weights for these resins were reported to be 60 000, 70 000, 80 000 and 90 000 Da, respectively. From this point forward, these resins will be called PA-6-24, PA-6-27, PA-6-32 and PA-6-36, respectively.

Since the same procedure was followed for all four different grades of polyamide 6, only one experimental procedure will be described.

PA-6-32, were found to produce the best polymers as it resulted in no clogging and dripping of the polymer solution and gave a stable Taylor cone. PA-6-32 pellets were dissolved in formic acid and acetic acid in a 1:1 ratio to yield a 6, 8, 10, 12, 14, 16 and 18 wt % solution and stirred for 24 h at room temperature to expedite dissolution of the polymers. All reagents were used without further purification. The polymer solution was electrospun using a 5 mL syringe with a hypodermic needle (inner diameter of 0.1 mm) at 0.2 ml/h flow rate for the different polymer solutions to obtain a stable Taylor cone. The polymer solution was electrospun onto a grounded collector covered with aluminium foil where the aligned, solidified nanofibers were collected. The potential was also varied (10-30 kV) depending on the solution as different polymer solutions stabilized at different voltages. All the experiments were performed at ambient room temperature (about 25 °C) under normal atmosphere with 25% humidity. The nanofibers were allowed to dry at room temperature overnight before further characterization was performed on them.

### 2.5.2 Functionalised ZnTCPPc (3), Conjugate (4) and mixed (5) nanofiber preparation

For functionalised nanofibers, ZnTCPPc (**3**, 2 mg), ZnTCPPc-Gd<sub>2</sub>O<sub>3</sub> NP (**4**, 3 mg) conjugate or the mixed (**5**) samples were added to the polymer solution (where the PA-6 pellets were dissolved in formic acid and acetic acid in **1:1 ratios** to yield a 14% solution), stirred overnight to aid dissolution, followed by electrospinning the following day to give the PA-6/ZnTCPPc, PA-6/ZnTPCPC-MNPs (conjugate) and PA-6/ZnTPCPC-MNPs mix nanofibres. The polymer solution was electrospun using a 5 mL syringe with a hypodermic needle (inner diameter of 0.1 mm) at a flow rate of 0.2 mL h<sup>-1</sup>. The solutions were electrospun onto a grounded collector covered with aluminium foil where the aligned, solidified nanofibers were collected. The voltage used for all solutions was 30 kV. All the experiments were performed at ambient temperature (about 25 °C) in air with 25% humidity. The nanofibers were allowed to dry at room temperature overnight before further characterization was performed on them.

## 2.6 References

1. Ogunsipe, J. Y. Chen, T. Nyokong, *New. J. Chem.* 28 (2004) 822
2. T. Minami, M. Kawahigashi, Y. Sakai, K. Shimamoto, S. Hirayama, *J. Lumin.*, 35 (1986) 347.
3. T.H. Tran-Thi, C. Desforge, C. Thiec, *J. Phys. Chem.* 93 (1989) 1226.
4. N. Kuznetsova, N. Gretsova, E. Kalmykova, E. Makarova, S. Dashkevich, V.Negrimovskii, O. Kaliya, E. Lukyanets, *Rus. J. Gen. Chem.* 70 (2000) 133.
5. M. Bazzi, C. Flores-Gonzalez, K. Louis, C. Lebbou, A. Dujardin, W. Brenier, O. Zhang, E. Tillement, P. Bernstein, J. Perriat. *Lumin* 102 (2003) 445.
6. Y. Li, T. M. Pritchett, J. Huang, M. Ke, P. Shao, W. Sun. *J. Phys. Chem. A* 112 (2008)

# **RESULTS AND DISCUSSION**

**Chapter 3: Synthesis and characterization**

**Chapter 4: Electrospun nanofibers**

**Chapter 5: Photodegradation of azo dye  
pollutants**

## Manuscripts in preparation

1. Surface Modification Of Silica-Coated Gadolinium Oxide Nanoparticles With Zinc Tetraphenoxycarboxy Phthalocyanine, **Mpho Ledwaba**, Tebello Nyokong, Edith Antunes (In Preparation).
2. Assembling Phthalocyanine-Magnetic Nanoparticle Hybrid Nanofibers For The Catalytic Photodegradation Of Orange-G, **Mpho Ledwaba**, Tebello Nyokong, Edith Antunes (In Preparation).

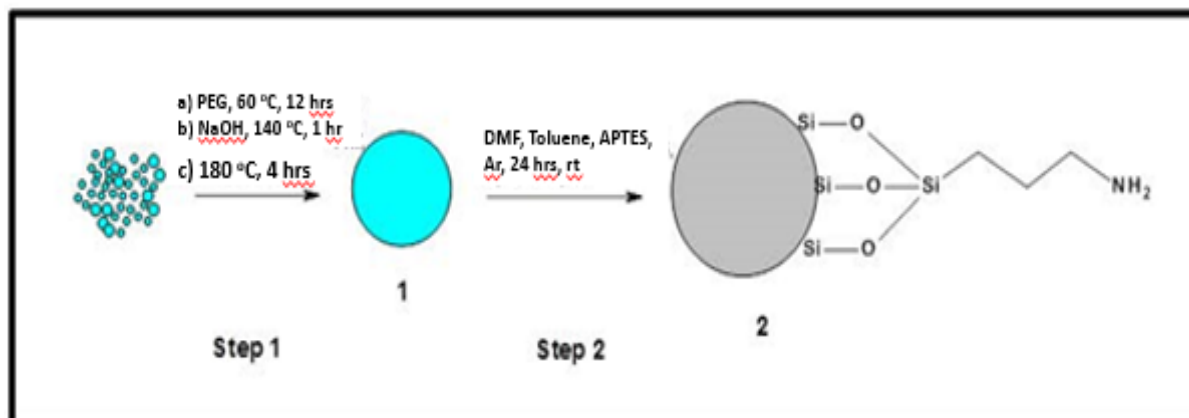
# Chapter 3

## Synthesis and Characterization

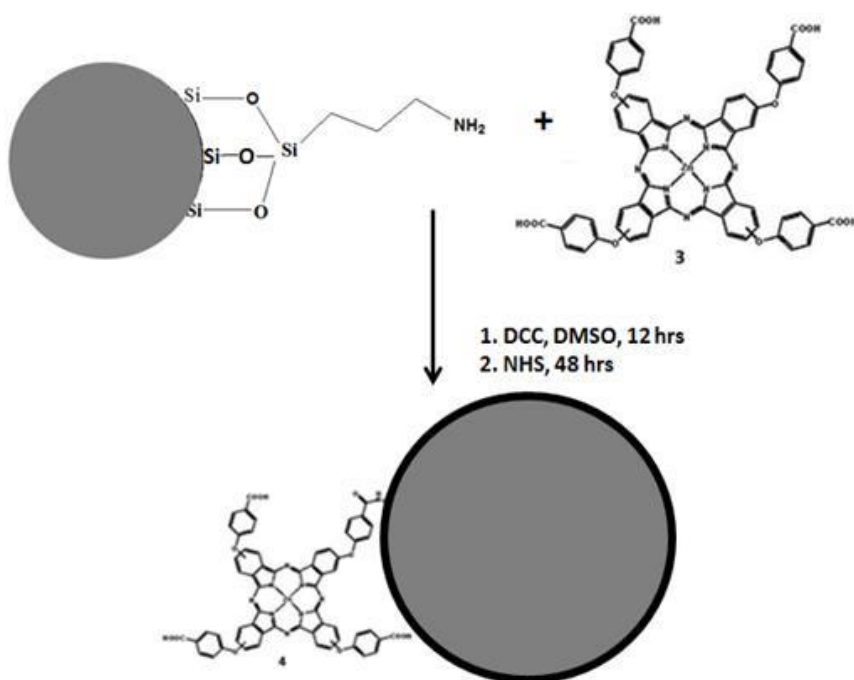
Reported in this chapter is the synthesis and spectroscopic characterization of the nanoparticles, i.e. gadolinium oxide nanoparticles ( $\text{Gd}_2\text{O}_3$  NPs, **1**), the silica-coated gadolinium oxide nanoparticles ( $\text{Si-Gd}_2\text{O}_3$  NPs, **2**), the phthalocyanine ( $\text{ZnTCPPc}$ , **3**) and the Pc-NP conjugate and composite (**4** and **5** respectively) employed in this work (as outlined in schemes 3.1 and 3.2 below). The preparation of the nanoparticles (**1**, **2**), the phthalocyanine (**3**), as well as the phthalocyanine functionalized nanoparticles (**4**, **5**) is discussed.







**Scheme 3.1:** Synthetic route for the preparation of the bare Gd<sub>2</sub>O<sub>3</sub> NPs (**1**) and the silica-coated Gd<sub>2</sub>O<sub>3</sub> NPs (Si-Gd<sub>2</sub>O<sub>3</sub> NPs, **2**). PEG = polyethylene glycol; APTES = aminopropyl triethoxysilane.



**Scheme 3.2:** Synthetic route showing the conjugation of the ZnTCPPc (**3**) to the surface of the silica-coated Gd<sub>2</sub>O<sub>3</sub> NPs (**2**) via an amide bond. DCC = N,N'-dicyclohexylcarbodiimide; NHS = N-hydroxy succinimide.

For the sake of ease, a list of the synthesized complexes used in this work is given below in Table 3.1.

**Table 3.1: List of the synthesized or functionalized complexes used in this work.**

Nanoparticle/complex	Abbreviation	No.
Gadolinium oxide nanoparticle	Gd <sub>2</sub> O <sub>3</sub> NP	1
Silica-coated gadolinium nanoparticles	Si-Gd <sub>2</sub> O <sub>3</sub> NP	2
Zinc tetraphenoxycarboxy phthalocyanine	ZnTCPPc	3
*ZnTCPPc linked gadolinium oxide nanoparticles	ZnTCPPc-SiGd <sub>2</sub> O <sub>3</sub> NP (conj)	4
*ZnTCPPc mixed gadolinium oxide nanoparticles	ZnTCPPc- Si-Gd <sub>2</sub> O <sub>3</sub> NP (mix)	5

\* ZnTCPPc- Zinc tetracarboxyphenoxypthalocyanine

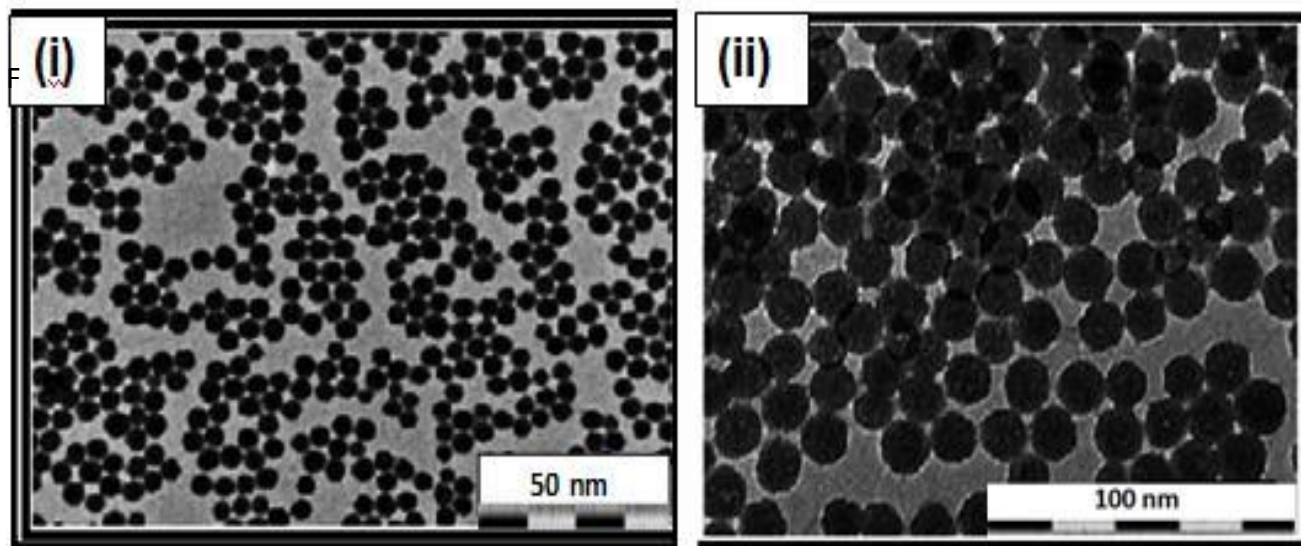
### 3.1 Synthesis and Characterization of the Gd<sub>2</sub>O<sub>3</sub> NPs (1 and 2)

The synthetic procedure for synthesizing the magnetic gadolinium oxide nanoparticles (Gd<sub>2</sub>O<sub>3</sub> NPs, **1**) as well as the procedure for coating the surface of the Gd<sub>2</sub>O<sub>3</sub> NPs with a silica shell to form Si-Gd<sub>2</sub>O<sub>3</sub> NPs (**2**) is shown in Scheme 3.1. Paramagnetic Gd<sub>3</sub>O<sub>2</sub> nanoparticles were prepared by using a two-step route polyol method as reported by Bazzi *et al.* [1]. Minor adjustments such as an increase in reaction time and an initial increase in temperature followed by a steady decrease, as depicted in chapter 2, were found to improve the shape and dispersion of the nanoparticles. The polyalcohol used was also different; in this case polyethylene glycol was used. Several methods were attempted in the preliminary stage of the study, however due to the need of attaining water soluble nanoparticles for biological studies and pollution studies, the polyol method was found to be the most appropriate. To allow for

stability, the magnetic nanoparticles (MNPs) were stabilized with PEG, giving a white powder which exhibited a strong magnetic response when brought close to a magnet. The nanoparticles were then functionalised with 3-aminopropyltriethoxy silane (APTES), also as reported in Bazzi *et. al.* [1], to give the aminofunctionalised nanoparticles. This amino group would allow for further functionalization with a suitable molecule of interest. APTES was found to produce highly stable nanoparticles and did not affect the monodispersivity of the nanoparticles by, for example, introducing aggregation as it can be seen from the TEM images.

### 3.1.1. Transmission electron microscopy (TEM)

TEM is an essential technique which allows one to visualise the shape, distribution and dispersion of nanoparticles [2]. The TEM images obtained for the uncapped/bare  $Gd_2O_3$  NPs (1) are shown in Figure 3.1 (i) which illustrates the excellent dispersion and size distribution of the nanoparticles. The sizes for the uncapped  $Gd_2O_3$  NPs (1) were determined to range from approximately 5.97 to 7.87 nm. The silica shell coating procedure to form the  $Si-Gd_2O_3$  NPs (2) was found to increase the size of the  $Gd_2O_3$  NPs from 6 nm to 15 nm, 3.1 (ii), as expected. Figure 3.1(ii) shows that the silica coated NPs (2) are still well dispersed and uniform in size.



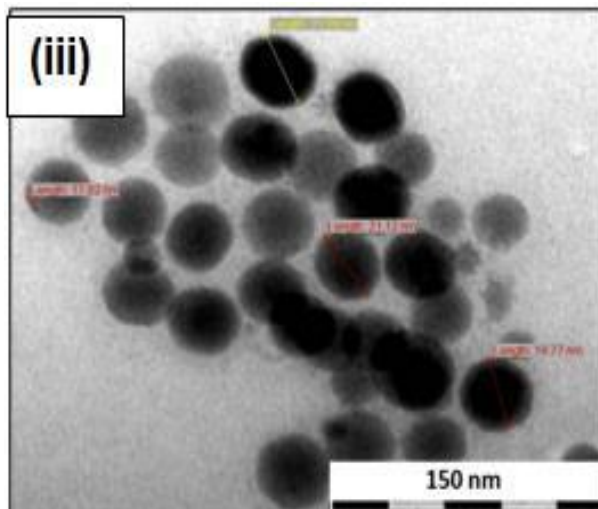


**Figure 3.1: TEM image of (i)  $Gd_2O_3$  NPs (1), (ii) Si- $Gd_2O_3$  NPs (2) (which shows the increased size of the nanoparticles), and (iii) ZnTCPPc- $Gd_2O_3$  NPs-conjugate (4) (showing the change in diameter and morphology of the conjugates).**

The  $Gd_2O_3$  NPs **1** and **2** were further characterized using Uv-Vis and FTIR spectroscopies, as well as thermogravimetric analyses (TGA), electron paramagnetic resonance (EPR), powder X-ray diffraction (XRD) and X-ray photoelectron spectroscopy (XPS). Apart from UV-Vis spectroscopy (this will be discussed later), the techniques listed above will be used to discuss the NPs synthesized.

### **3.1.2 Fourier transform infrared (FTIR) spectroscopy**

FTIR is a measurement technique which is used in identifying the structure of a molecule by means the characteristic functional group bands, which are identified by means of the position (frequency) and their intensity [3].

Satisfactory FTIR data were obtained for all the NPs which confirmed the silica-coating on the surface of the gadolinium oxide nanoparticles. **A strong bands at 1150  $cm^{-1}$**  which correspond to the Si-O bend is observed after functionalization [4]. Also a characteristic peak at 1560  $cm^{-1}$  of

a primary amino group (-NH<sub>2</sub>) is observed in Figure 3.2(iii) confirming the efficient functionalization of the surface of the gadolinium oxide nanoparticles. The spectrum of pure PEG is characterized greatly by the stretching vibration of the C-H at 2887 cm<sup>-1</sup>, which can be observed in the spectra of the gadolinium oxide nanoparticles. The broadened peak in the range of 3100 to 3600 cm<sup>-1</sup> can be attributed to the OH group found on PEG [5]. This is observed in all the FTIR spectra (i, ii and iii). Similar spectral changes were observed for the Gd<sub>2</sub>O<sub>3</sub>NPs and Si-Gd<sub>2</sub>O<sub>3</sub>NPs.

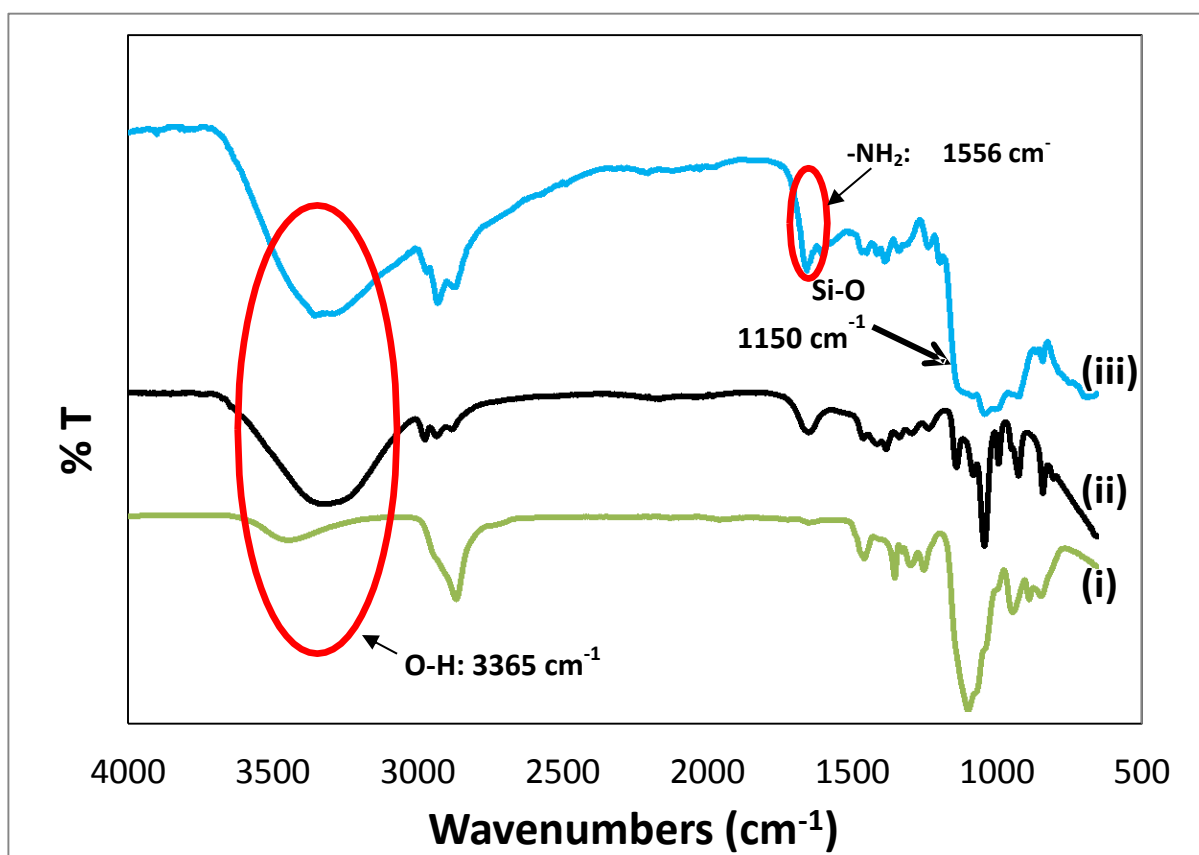


Figure 3.2: FTIR (i) PEG utilized in the synthesis and the synthesized nanoparticles (ii) Gd<sub>2</sub>O<sub>3</sub> NPs (1) and (ii) Si-Gd<sub>2</sub>O<sub>3</sub> NPs (2).

### 3.1.3 Thermogravimetric analysis (TGA)

Thermogravimetric analysis (TGA) is a **thermodynamic** technique. This characterization method determines the mass loss or gain of a sample over a certain temperature profile [6]. In this work, TGA was used to confirm the compositional differences between the bare and silica coated gadolinium oxide nanoparticles (**1** and **2**). Different thermal decomposition profiles point to structurally different materials. The thermal decomposition profiles obtained under a steady flow of  $N_2$ , at a heating rate of  $10\text{ }^\circ\text{C min}^{-1}$  are shown in Figure 3.3.

The TGA curves shown in Figure 3.3 are for the starting materials, i.e. the  $Gd(NO_3)_3$  salt (i) and polyethylene glycol (ii); the bare  $Gd_2O_3$  NP (iii) and the silica-coated NP (Si- $Gd_2O_3$  NP, (iv)). The Gd salt (Figure 3.3 (i)) shows two main weight loss steps with a third possibly taking place at approximately  $500\text{ }^\circ\text{C}$ . The first step at  $\sim 150\text{ }^\circ\text{C}$  i.e. an initial loss of 15% is attributed to the loss of water while the slow decomposition step (50% weight loss) taking place up to  $420\text{ }^\circ\text{C}$  is thought to be due to the loss of the **atoms of the salt**. The Gd metal content in the salt is calculated to be 35%, though the mass loss at the end of this TGA run is only at 53% which suggests that removal of the functional groups is not complete at  $500\text{ }^\circ\text{C}$ . The thermal decomposition profile of the capping agent alone, PEG (Figure 3.3 (ii)), shows a single, dramatic, complete (100% weight loss) decomposition step with an onset temperature of approximately  $190\text{ }^\circ\text{C}$ .

The bare  $Gd_2O_3$  NP (Figure 3.3 (iii)) revealed a single, featureless step (20% weight loss) which is attributed to the slow decomposition of the organic material (probably the PEG) on the surface of the nanoparticle. It is predicted that the entire PEG capping agent on the surface of the NP should be removed by  $420\text{ }^\circ\text{C}$ . It is also possible to make the assumption that the PEG capping constituted approximately 20% of the NP sample. At first it is surprising to note that the thermal stability of the silica coated NP (Figure 3.3 (iv)) was reduced by 20% (upon comparison of the % weight loss at  $500\text{ }^\circ\text{C}$  for the  $Gd_2O_3$  NP and Si- $Gd_2O_3$  NP samples). However, the decrease in thermal stability for these nanoparticles can be accounted for as additional organic groups (aminopropyl functional groups) have now been added to the surface of the NP and

will consequently tally the increase in overall weight loss for the silica coated NP at 500 °C. The initial weight loss (up to 150 °C) though may also be due to the loss of adsorbed water or solvents.

The Gd<sub>2</sub>O<sub>3</sub> NPs and the Si-Gd<sub>2</sub>O<sub>3</sub> NPs were shown to be thermally stable as compared to the Gd(NO<sub>3</sub>)<sub>3</sub> salt and PEG as they retain over 50% of their weight at temperatures above 400 °C.

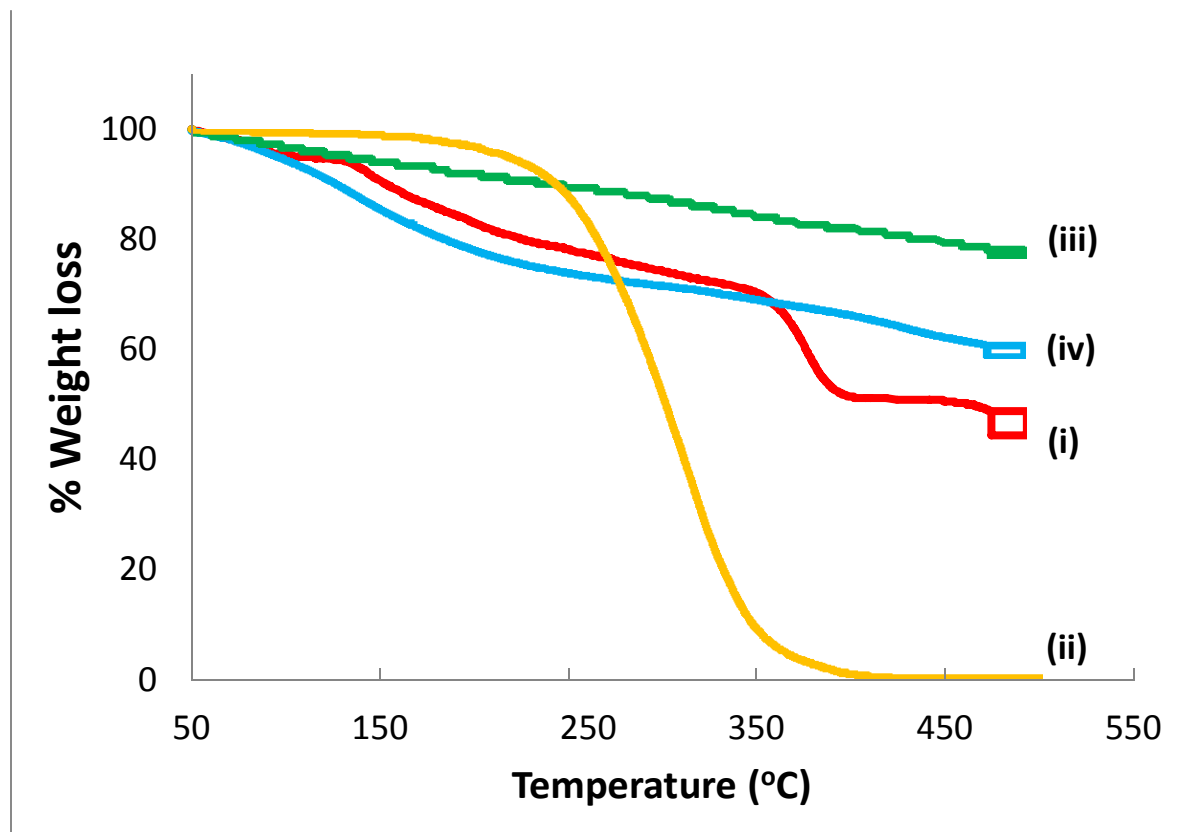


Figure 3.3: TGA profiles of (i) Gd(NO<sub>3</sub>)<sub>3</sub>, (ii) PEG, (iii) Gd<sub>2</sub>O<sub>3</sub>NPs (1) and (iv) Si-Gd<sub>2</sub>O<sub>3</sub>NPs (2).

### 3.1.4 X-ray diffraction (XRD)

X-ray diffraction (XRD) is a spectroscopic technique that is used for the elucidation of structural information relating to the crystal lattice of a sample; here it was intended to aid the determination of the nanoparticle size by making use of the Debye-Scherrer equation, to give an idea of the degree of crystallinity and purity of the sample, and finally to enable comparison



between the nanocomposite formed (in particular ZnTCPPc-SiGd<sub>2</sub>O<sub>3</sub> (conj), **4**) and the individual components.

The XRD patterns for the bare Gd<sub>2</sub>O<sub>3</sub> and the Si-Gd<sub>2</sub>O<sub>3</sub> nanoparticles are shown in Figure 3.4 (i) and (ii), respectively. An attempt was made to determine the crystal structure and purity of the Gd<sub>2</sub>O<sub>3</sub> and SiGd<sub>2</sub>O<sub>3</sub> nanoparticles by measuring the XRD data and a broad peak is observed at  $\sim 2\theta = 20^\circ$  for both samples. A broad reflection is expected at this position due to amorphous silica which was used to cap the NPs (**2**) [7]. For comparative purposes, the synthesised NPs (**1** and **2**) were compared to the starting Gd(NO<sub>3</sub>)<sub>3</sub> salt (Figure 3.4). However, the information derived from the x-ray diffractograms for the gadolinium oxide NPs (**1** and **2**) were not clear, with the patterns suggesting either that there is a substantial degree of amorphousness or that the nanoparticles are very small, resulting in significant line broadening observed when the Gd<sub>2</sub>O<sub>3</sub> NPs are smaller than 20 nm [8,9]. From these data, it was not possible to determine whether the NPs could be indexed to the cubic phase (JCPDS card No. 11-604) as is expected for Gd<sub>2</sub>O<sub>3</sub> NPs [10]. The TEM images (Figure 3.1 (i and ii)) obtained and described above, however, clearly show the NP shape and crystal structure, although the XRD data does not.

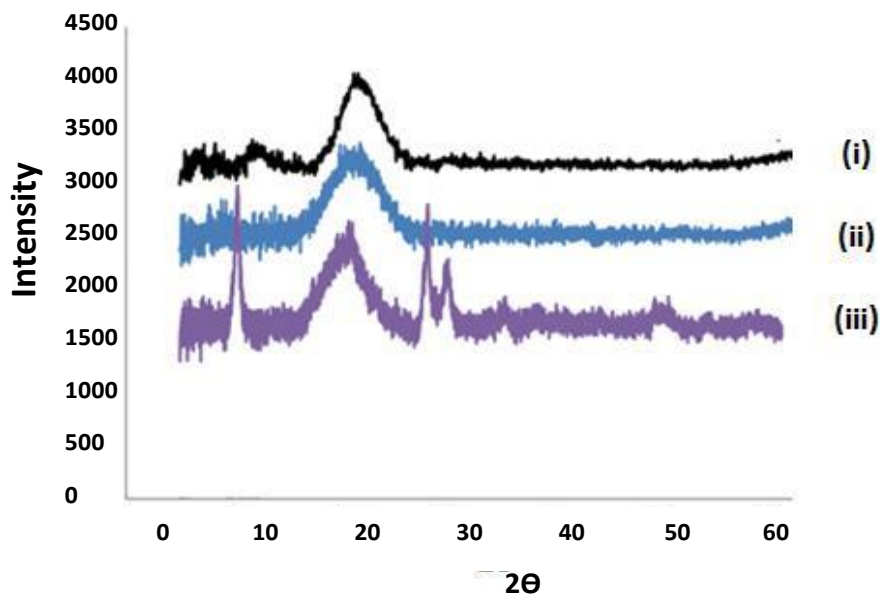


Figure 3.4: X-Ray diffractograms of (i) Gd(NO<sub>3</sub>)<sub>3</sub>, salt (ii) bare Gd<sub>2</sub>O<sub>3</sub> NPs (**1**) and (iii) Si-Gd<sub>2</sub>O<sub>3</sub> NPs (**2**)

### 3.1.5 X-ray Photoelectron Spectroscopy

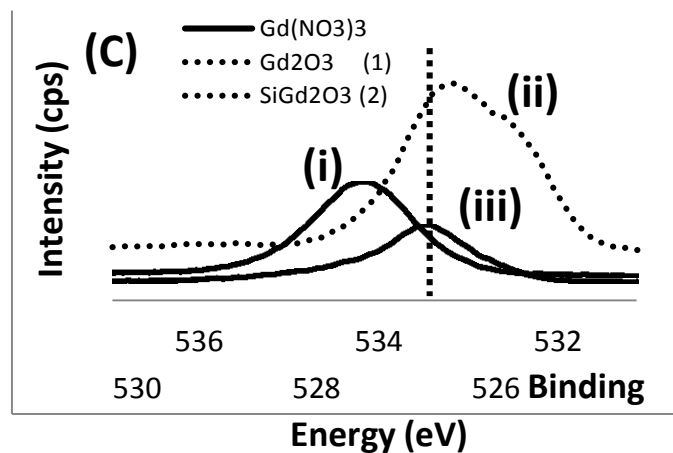
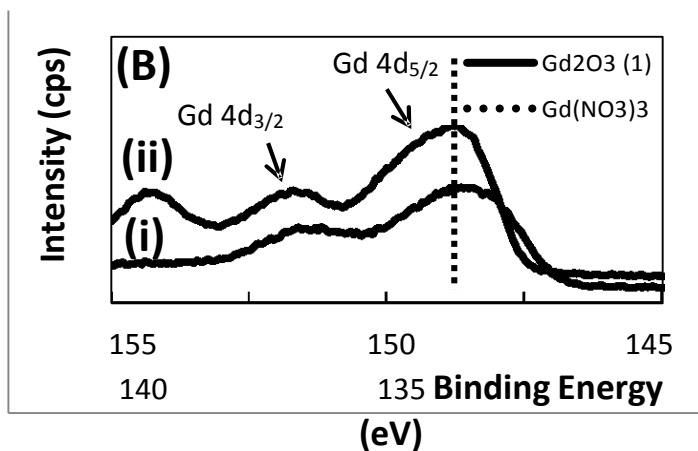
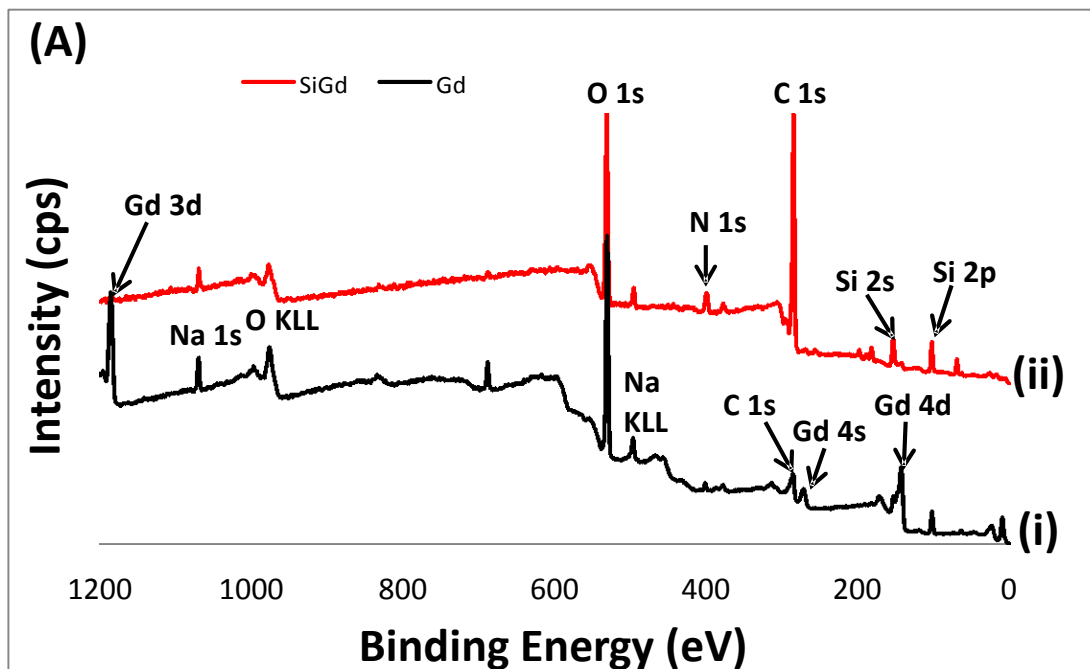
X-ray photoelectronspectroscopy (XPS) is a surface-sensitive, quantitative spectroscopic technique that measures the elemental composition at parts per thousand ranges. XPS is used to analyse the surface chemistry of a material, elemental composition of the surface, chemical or electronic state of each element in the surface, elements that contaminate a surface and can also determine the empirical formula of pure materials. Each element produces a characteristic set of XPS peaks at characteristic binding energy values that directly identify each element that exists in or on the surface of the material being analysed [11].

X-ray photoelectron spectroscopy (XPS) measurements were performed in this work to confirm the elemental constituents of the synthesised material.

Wide scan and high resolution XPS spectra were acquired for the  $\text{Gd}_2\text{O}_3$  (**1**) and  $\text{Si-Gd}_2\text{O}_3$  (**2**) NPs (Figure 3.5A (i) and (ii) respectively) and the experimental data analysed using curve fitting. Figure 3.5A (ii) clearly shows the presence of the characteristic Gd peaks, particularly the Gd  $3d_{3/2}$  and  $3d_{5/2}$  peaks at  $\sim 1185$  eV, together with C 1s, O 1s and Na 1s peaks for the bare  $\text{Gd}_2\text{O}_3$  NP (**1**). The O 1s (at  $\sim 530$  eV) was expected to be part of the  $\text{Gd}_2\text{O}_3$  NP core as well as the hydroxyl oxygen atoms of the capping agent PEG. The capping agent also accounted for the presence of carbon (at  $\sim 284$  eV) in the XPS spectra. Na peaks (Na 1s at  $\sim 1100$  eV) were also observed and are most likely due to the NaOH used in the synthesis of the NPs (**1**). It is difficult to estimate the experimental Gd/O ratio (which may be calculated from the total areas under the peaks of the Gd 3d and O 1s peaks in the survey XPS spectrum) since the organic capping agent may suppress the signal from the NP core. However, this is dependent on the thickness of the capping agent layer. For this reason survey spectra of the sample annealed at  $500^\circ\text{C}$  were also analysed but the temperatures used for annealing were not high enough as some C was still observed in the spectra.

The survey scan obtained for the silica coated  $\text{Gd}_2\text{O}_3$  (**2**), shows that the silica coating step has completely capped the NP (Figure 3.5A (ii)), as none of the Gd peaks are now observed. This was to be expected as XPS is a surface sensitive technique (where typically the photoelectrons

generated are from within the first 3 nm of the surface being analysed) [10]. The survey scan obtained for NP 2 shows instead the characteristic peaks associated with Si (e.g. Si 2p at 100 eV) and an increase in intensity of the N 1s peak at 397 eV, the position of this peak also indicates successful amino group functionalization [12].





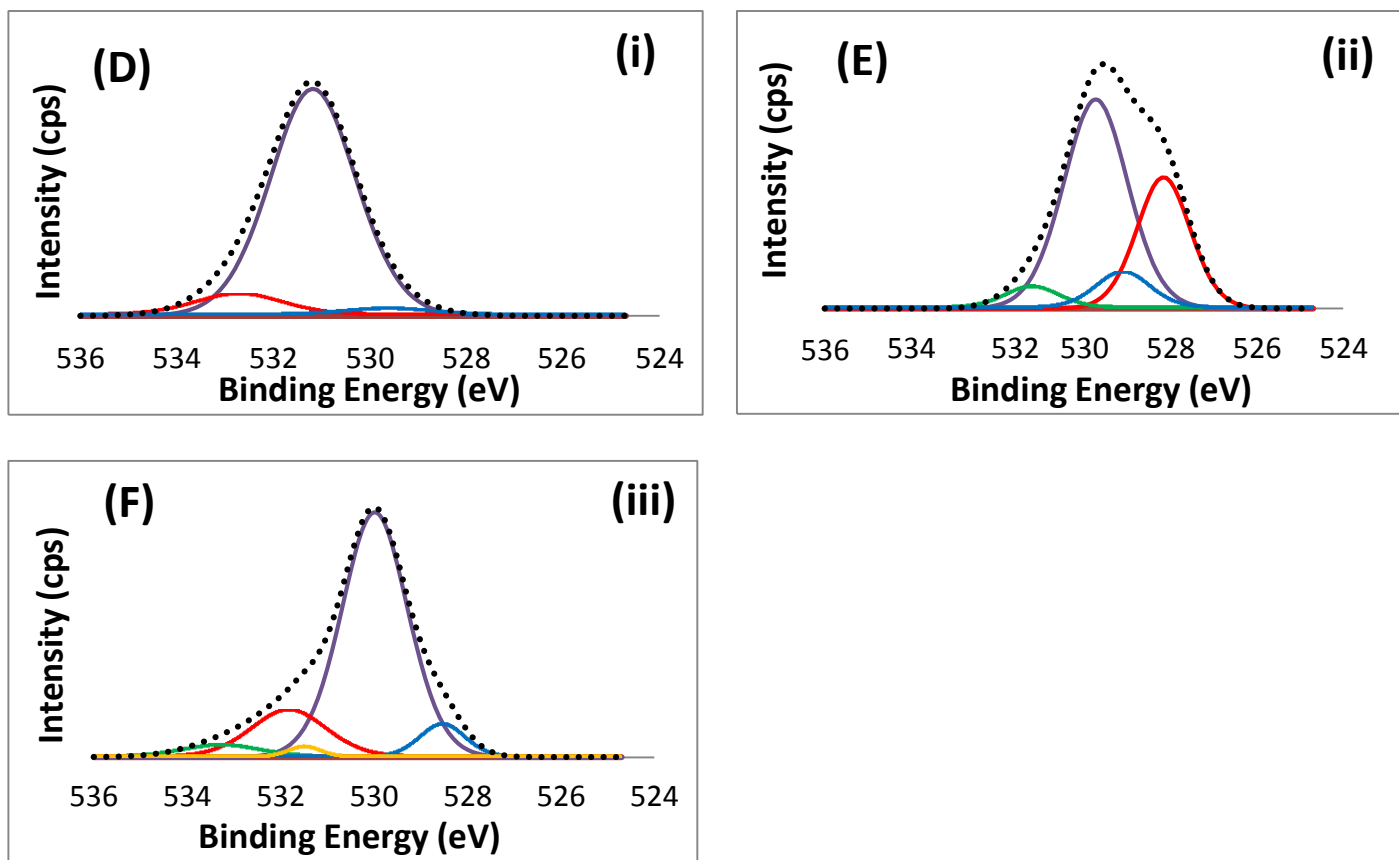


Figure 3.5: Wide scan XPS spectra (A) of (i) Gd<sub>2</sub>O<sub>3</sub> NPs (1) and (ii) SiGd<sub>2</sub>O<sub>3</sub> NPs (2). High resolution spectra of: (B) Gd 4d region for (i) Gd(NO<sub>3</sub>)<sub>3</sub> salt and (ii) Gd<sub>2</sub>O<sub>3</sub> NP; and (C) O 1s region for (i) Gd(NO<sub>3</sub>)<sub>3</sub> salt, (ii) Gd<sub>2</sub>O<sub>3</sub> NPs, and (iii) SiGd<sub>2</sub>O<sub>3</sub> NPs. Deconvolution of the O 1s high resolution spectra is given in graphs D – F where: (D) is the Gd(NO<sub>3</sub>)<sub>3</sub> salt (i), (E) is the bare Gd<sub>2</sub>O<sub>3</sub> NP (ii), and (F) is the Si-Gd<sub>2</sub>O<sub>3</sub> NP (iii).

Figure 3.5B shows the high resolution spectra obtained for the Gd 4d regions for the Gd(NO<sub>3</sub>)<sub>3</sub> salt and Gd<sub>2</sub>O<sub>3</sub> NPs (1), while Figure 3.5C shows the data for the high resolution O 1s regions for the Gd(NO<sub>3</sub>)<sub>3</sub> salt employed and the synthesised Gd<sub>2</sub>O<sub>3</sub> NPs (1 and 2). For the Gd<sub>2</sub>O<sub>3</sub> NP (1), the Gd 2d<sub>3/2</sub> and Gd 2d<sub>5/2</sub> peaks were found to reside at 142.5 and 148.8 eV (Figure 3.5B(ii)) and this found to be in agreement with XPS values reported for cubic phase Gd<sub>2</sub>O<sub>3</sub> [13].

Figure 3.5C shows the high resolution spectra for the O 1s peak of the Gd(NO<sub>3</sub>)<sub>3</sub> salt (Figure 3.5C(i)) employed and the Gd<sub>2</sub>O<sub>3</sub> NPs (1 and 2) obtained (Figure 3.5C(ii) and (iii) respectively).

Deconvolutions of the high resolution O 1s spectra are shown in Figure 3.5D-F. The differences are clear, where the O 1s peaks are found at higher binding energies for the nitrate salt (Figures 3.5C and 3.5D). The O 1s peak for the nitrate salt shows perhaps 3 peaks, one main peak (at 531.4 eV) with a second smaller peak (532.9 eV) at a higher binding energy and a third, almost negligible peak (at 529.9 eV). Since oxygen is ubiquitous in systems, it is possible that at least one of these peaks is due to normal adsorption of oxygen to the sample. The two other peaks are attributed to N-O and Gd-O O 1s peaks for the gadolinium nitrate salt shown in 3.5B (i) [14]. The O 1s high resolution spectra for the Gd<sub>2</sub>O<sub>3</sub> NP (**1**) sample, (Figure 3.5C(ii)), shows two main peaks centred at 529.5 eV and 527.9 eV, together with two smaller peaks at ~531.4 and 529.4 eV, clearly seen upon deconvolution of the O 1s spectra (Figure 3.5E). The two main peaks are presumably due to the Gd-O and Gd=O, while the other would be due to either the C-O or the O-H of the capping agent PEG. Finally, the high resolution O 1s spectra for Si-Gd<sub>2</sub>O<sub>3</sub> NP (**2**) (Figure 3.5C(iii)) showed a complicated deconvolution pattern (6 peaks), however there is one main peak centred at 530.2 eV (Figure 3.5F) which is attributed to the Si-O peak [15] (of the silica shell on the NP), since this is a surface analytical technique, the core O 1s peaks (e.g. Gd-O) of the Gd<sub>2</sub>O<sub>3</sub> NP, while they can still be present, is not expected to be intense. The other peaks are therefore considered to be due to ubiquitous O, Gd-O (shell) and Gd-O (core). The sources of the other peaks are not yet known. All these results confirm that a silica shell has been placed on the surface of the nanoparticle [16].

### 3.1.6 Electron Paramagnetic Resonance

Electron paramagnetic resonance (EPR), a magnetic resonance technique similar to nuclear magnetic resonance (NMR), is an excellent technique for studying materials with unpaired electrons and detecting paramagnetic species such as free radicals [17]. In this study EPR was used to evaluate the paramagnetic properties of the Gd<sub>2</sub>O<sub>3</sub> nanoparticles (**1** and **2**) and the conjugate in order to get an idea of their effectiveness as MRI agents for diagnosis.

The solid state EPR spectra, expected to be broad, are shown in Figure 3.6.  $Gd^{3+}$  is paramagnetic (due to seven unpaired electrons), but its EPR spectrum consists of only one broad line due to spin-spin interactions between unpaired electrons; hence the observed broad spectra. For comparison, the spectrum for the  $Gd(NO_3)_3$  salt is shown in Figure 3.6, showing an intense, asymmetrical, broad curve. On the other hand, the EPR spectra acquired for  $Gd_2O_3$  (**1**) and  $SiGd_2O_3$  (**2**) NPs, shown in Figure 3.6 (insert), show very *weak* asymmetrical, broad signals.  $Gd(III)$  is a paramagnetic species, however since the relaxation time of  $Gd(III)$  is extremely short, detection of  $Gd$  complexes using EPR is difficult [18] and a stronger magnet is most likely needed at very low temperatures to detect paramagnetic species. It may be possible that the NPs **1** and **2**, have even shorter relaxation times, making detection much more difficult [16]. Though the EPR spectra did not show conclusive results,  $Gd$  is present in the NP system – as it was accounted for with the XPS measurements.

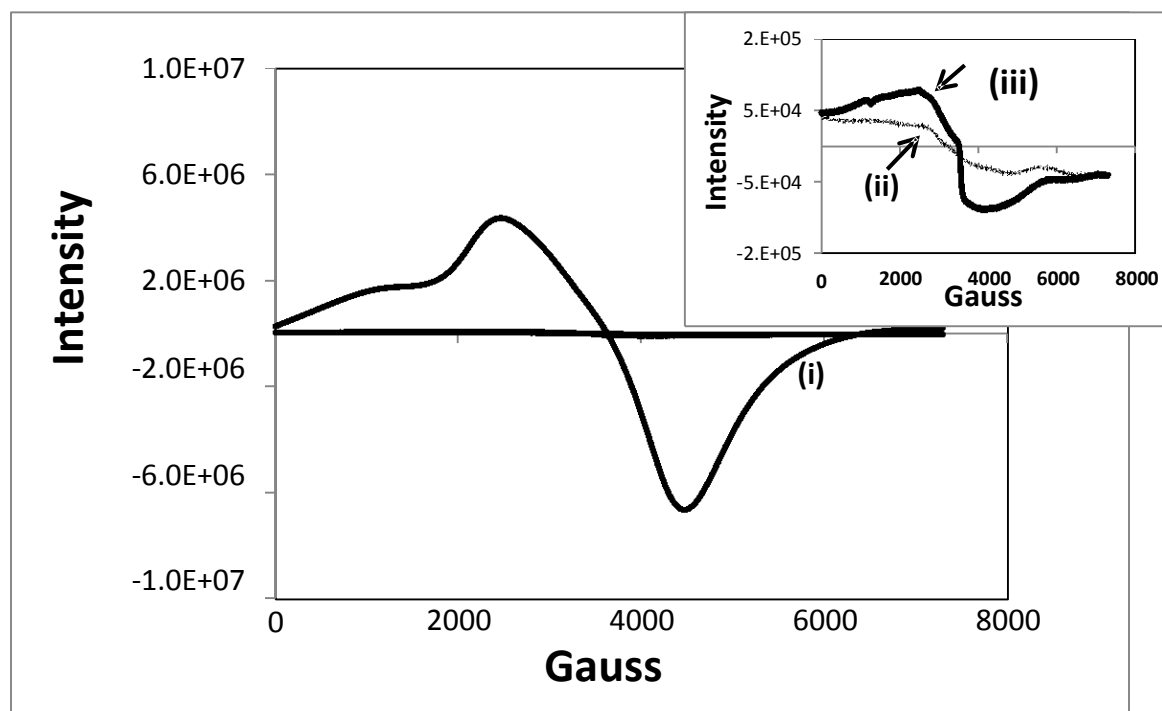


**Figure 3.6:** EPR spectra acquired in the solid state at room temperature for (i)  $Gd(NO_3)_3$ , (ii)  $Gd_2O_3$  NPs (**1**) and (iii)  $Si-Gd_2O_3$  NPs (**2**). Inset: zoomed in section to show the spectra obtained for the NPs.

## 3.2 Synthesis and characterization of the phthalocyanine-MNP conjugates

### 3.2.1 Synthesis and characterization of zinc tetracarboxyphenoxy phthalocyanine (3, ZnTCPPc)

The zinc tetracarboxyphenoxy phthalocyanine (ZnTCPPc) was synthesized according to a method reported in literature. The method followed a synthesis using 4-nitrophthalonitrile and 4-(3,4-dicyanophenoxy)benzoic acid which were also synthesised according to literature methods [19]. The expected molecular weight of the ZnTCPPc molecule was 1120 g/mol, however the experimental molecular weight found was 1058 g/mol. The decrease was calculated to be due to the loss of H<sub>2</sub>O and a COO<sup>-</sup>.

Using FTIR spectroscopy, the IR spectra of the Pc showed characteristic peaks of the OH group in the 3430 cm<sup>-1</sup> region, the C=O was confirmed by the peak at 1640 cm<sup>-1</sup> and the C=C peaks were observed at 1581 cm<sup>-1</sup> and 1480 cm<sup>-1</sup>. C-O-C peaks were evident at 1251 cm<sup>-1</sup> and 1180 cm<sup>-1</sup> regions of the spectra. C-H peaks were observed at 840 cm<sup>-1</sup>.

The Pc showed a broad absorbance peak known as the B band at 349 nm in DMSO, Figure 3.7. The ground state electronic absorption spectra of ZnTCPPc also showed monomeric behaviour as evidenced by a single, narrow Q-band. The Q band of the ZnTCPPc in DMSO is observed at 678 nm, Figure 3.7.



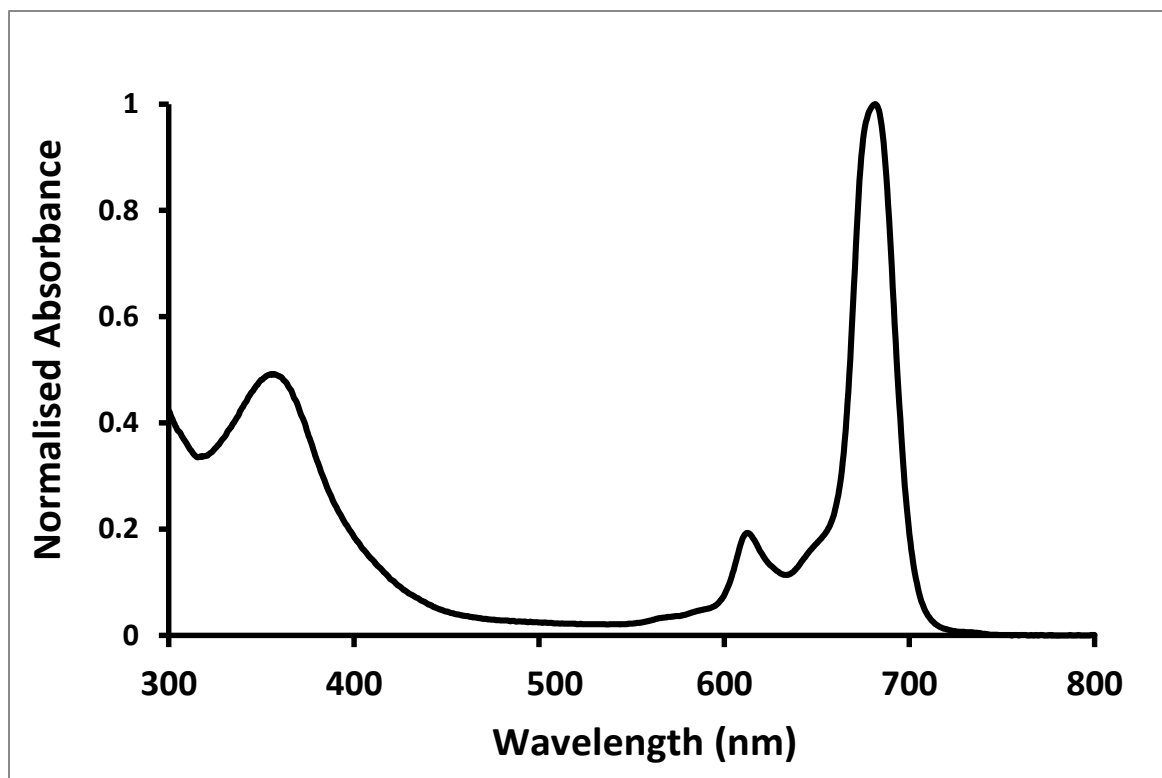
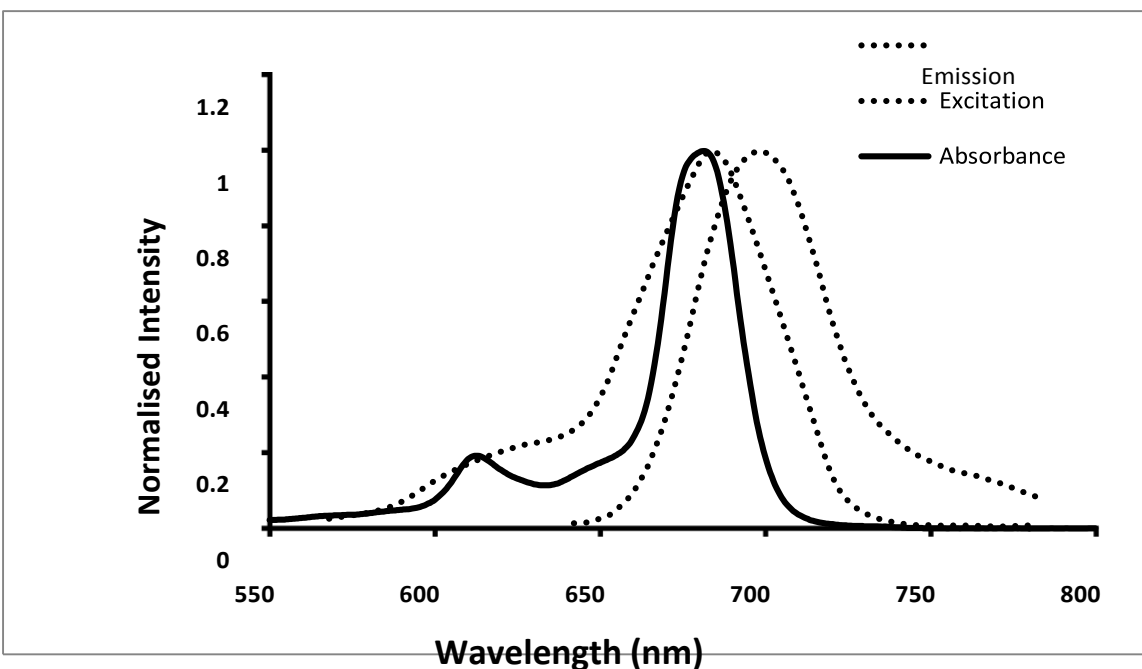


Figure 3.7: UV-vis **spectrum** of ZnTCPPc in DMSO. The Figure illustrates the typical monomeric behaviour of the Pc with a Q-band maximum at 678 nm.

The fluorescence **excitation** spectra were found to be similar to absorption spectra and both were mirror images of the emission spectra, Figure 3.8. The position of the Q band in the excitation and absorption spectra were observed at 679 and 678 nm respectively, while the emission peak was observed at 689 nm giving a **Stokes** shift of 10nm. The fluorescence excitation and emission spectra are typical of phthalocyanine complexes in DMSO, where Stokes shifts typically range from 3-19 nm [20].



**Figure 3.8 Normalized absorption, emission and excitation spectra of ZnTCPPc in DMSO.**

$\lambda_{\text{Abs}_{\text{max}}}$ = 679;  $\lambda_{\text{Exc}_{\text{max}}}$ = 680 nm;  $\lambda_{\text{Em}_{\text{max}}}$ = 689 nm.

### 3.2.2 Assembly of the phthalocyanine-MNP conjugates

The main goal in functionalizing the NP surface is to modify their surface with a molecule that possesses the appropriate chemical functionality which would then allow the NP to serve as a platform to enable further conjugation/ derivatization and achieve a desired application. The molecule of interest in this work is the phthalocyanine. This was done to allow for multi-functionality of the nanocomposite i.e. MRI (attributes imparted by the  $\text{Gd}_2\text{O}_3$  NP) and PDT (due to the properties imparted by the phthalocyanine) during cancer therapy. Chemical functionalization of the nanoparticle can be achieved either by covalent attachment or by non-covalent (adsorption) reaction. Planar molecules are capable of adsorbing onto the nanoparticle surface via  $\pi$ - $\pi$  interactions [21]. The as-synthesised gadolinium oxide nanoparticles were functionalised with 3-(aminopropyl)triethoxysilane (APTES), which served a dual purpose: firstly, it introduced amino groups onto the surface of the nanoparticles and

secondly, it improved the dispersability of the NP in a variety of solvents. The presence of the amino group on the NP surface also now facilitated conjugation of the carboxy substituted Pc to the amino functionalized NP to form an amide bond.

### 3.2.2.1 Synthesis and characterization of the phthalocyanine – MNP conjugate

At this stage the silica-coated nanoparticles (Si-Gd<sub>2</sub>O<sub>3</sub> NP, **2**) were then functionalized with the carboxy substituted phthalocyanine (**3**). The carboxylic acid groups on the ZnTCPPc enabled covalent linkage to the amino functionalized MNPs through formation of an amide bond. N,N'-dicyclohexylcarbodiimide (DCC) and N-hydroxy succinimide (NHS) were used to activate the carboxylic acid groups on the ZnTCPPc before linking to the amino groups of the MNPs, as shown by Scheme 3.2. The covalent linkage was followed by characterization using some of the techniques described previously i.e. FTIR spectroscopy, as well as thermogravimetric analyses (TGA), XRD and XPS confirming the covalent linkage. High yields were obtained for all the compounds.

The absorbance of the Si-Gd<sub>2</sub>O<sub>3</sub> (**2**) nanoparticles in DMSO in the UV/Vis spectra is minimal and is shown in Figure 3.9 (i). The ground state electronic absorption spectra of the ZnTCPPc (**3**) alone, is shown in Figure 3.9 (ii) in DMSO. No significant change was observed in the UV/Vis absorption spectra when the NPs (**2**) and the Pc (**3**) were simply mixed (Figure 3.9 (iv)), where the effects of Si-Gd<sub>2</sub>O<sub>3</sub> are less pronounced in terms of the absorption seen in the 600 to 400 nm range. On the other hand, a steady increase of absorbance from 600 to 400 nm was observed for the conjugate upon linking the Pc (**3**) to the Si-Gd<sub>2</sub>O<sub>3</sub> (**2**), Figure 3.9 (iii), and this is due to absorption caused by the nanoparticles. No shifts in the Q band of the ZnTCPPc (**3**) were observed for the conjugate (**4**) or the mixture (**5**).

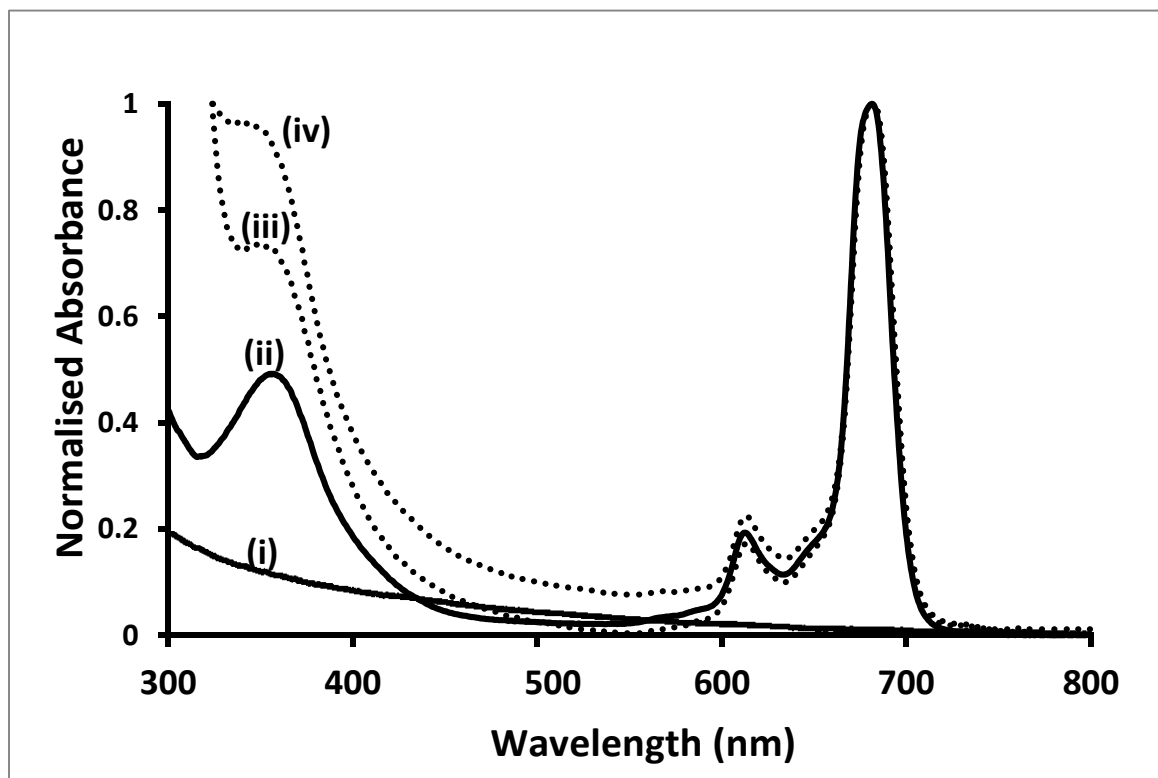


Figure 3.9: UV/vis spectra obtained for the samples in DMSO: (i) Si-Gd<sub>2</sub>O<sub>3</sub> NPs (2), (ii) ZnTCPPc (3), (iii) ZnTCPPc-SiGd<sub>2</sub>O<sub>3</sub> NP (conj) (4) and (iv) ZnTCPPc-SiGd<sub>2</sub>O<sub>3</sub> NP-mix (5).

### 3.2.2.2 TEM

The TEM image in Figure 3.1 (iii) for the ZnTCPPc-SiGd<sub>2</sub>O<sub>3</sub> NP (conj) (4) shows that the size of the SiGd<sub>2</sub>O<sub>3</sub> NPs (2) was further increased upon conjugation with the phthalocyanine to 17 nm, providing some evidence of the nanocomposite (4) formation. These images show that the nanocomposite (4), although there is a change in the overall appearance of the NP, is still well dispersed and somewhat uniform in size.

### 3.2.2.3 FTIR spectroscopy

The covalent link expected to form between the Si-Gd<sub>2</sub>O<sub>3</sub> NPs (**2**) and ZnTCPPc (**3**) to form the nanocomposite (**4**) was confirmed using FTIR spectroscopy, as shown in Figure 3.10A and B.

The characteristic peaks of the primary amino (-NH<sub>2</sub>) groups for Si-Gd<sub>2</sub>O<sub>3</sub> NPs (**2**) are observed at 1568 cm<sup>-1</sup> and 1463 cm<sup>-1</sup> [4], Figure 3.10(i). The intense peak at ~1060 cm<sup>-1</sup> is assigned to the Si-O-Si bonding stretch for the NPs (**2**), as reported in literature [22]. The ZnTCPPc (**3**) alone (Figure 3.10 (ii) shows the C=O vibrational band at 1640 cm<sup>-1</sup> and weak bands in the range 3100 cm<sup>-1</sup> to 3600 cm<sup>-1</sup> corresponding to the O-H of the carboxyl group. For the ZnTCPPc-Gd<sub>2</sub>O<sub>3</sub> NPs (conj, **4**) conjugate Figure 3.10 A(iii), the peaks attributed to the -COOH functional group disappeared, while the peaks assigned to the amide (-NHCO-) group at 1631 cm<sup>-1</sup> and 1535 cm<sup>-1</sup> were enhanced, with the appearance of an -NH- stretch at 3283 cm<sup>-1</sup>, Figure 3.10 (iii). The presence of these bands suggests the successful formation of a covalent bond between the Si-Gd<sub>2</sub>O<sub>3</sub> NPs (**2**) and ZnTCPPc (**3**). These spectra were compared to ZnTCPPc-SiGd<sub>2</sub>O<sub>3</sub> NPs (mixed, **5**). Figure 3.10 A(iv) shows that the C=O vibrational peak (at 1710 cm<sup>-1</sup>) and the O-H of the carboxyl group of (~ 3300 cm<sup>-1</sup>) for the ZnTCPPc remains unchanged in composite **5**. This spectrum served to show the differences between a nanocomposite (**4**) and that of a simple mixture (i.e. no covalent bond link, **5**) between the SiGd<sub>2</sub>O<sub>3</sub> NPs (**2**) and ZnTCPPc (**3**). The most apparent difference between the mixture (**5**, Figure 3.10 B(iii)) and the nanocomposite (**4**, Figure 3.10 B(ii)) is the shift in the C=O stretch at 1700 cm<sup>-1</sup> and the appearance of an amide N-H stretch at 3300 to 3500 cm<sup>-1</sup> upon conjugation.

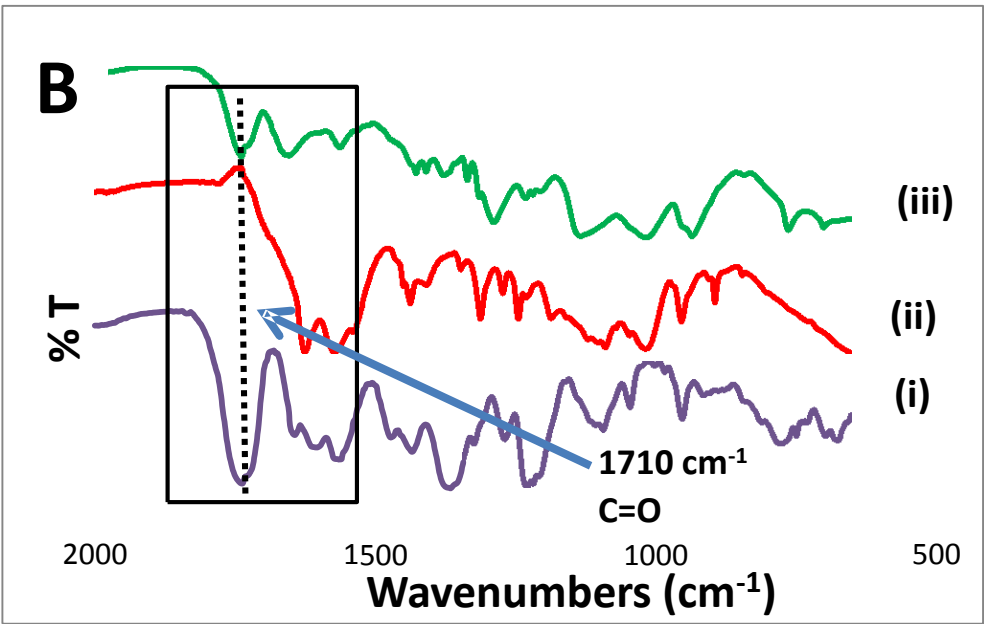
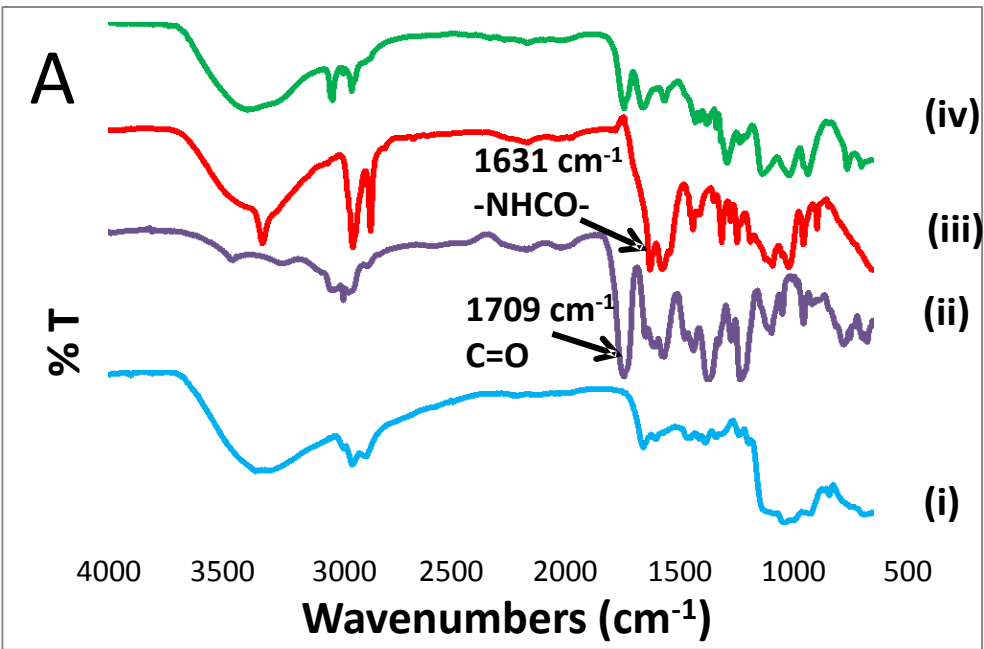


Figure 3.10: FTIR spectra of the synthesized (A) (i) Si-Gd<sub>2</sub>O<sub>3</sub> NPs (2), (ii) ZnTCPPc (3), (iii) ZnTCPPc-SiGd<sub>2</sub>O<sub>3</sub> NP (4) and (iv) the simple mixture ZnTCPPc-SiGd<sub>2</sub>O<sub>3</sub> NP-mix (5). Graph (B) are zoomed into the region 2000 – 600 cm<sup>-1</sup> to highlight the changes observed between (i) ZnTCPPc (3), (ii) ZnTCPPc-SiGd<sub>2</sub>O<sub>3</sub> NPs (4) and ZnTCPPc-SiGd<sub>2</sub>O<sub>3</sub> NPs-mix (5).

### 3.2.2.4 Thermogravimetric Analyses

The thermal decomposition profiles obtained for ZnTCPPc (i) and the ZnTCPPc –Si-Gd<sub>2</sub>O<sub>3</sub> (4) are shown in Figure 3.11. The decomposition profile for the Si-Gd<sub>2</sub>O<sub>3</sub> NPs (2) has already been described above in section 3.1.3 but is included here as Figure 3.11 (i) for ease of comparison. Two main decomposition steps are observed for ZnTCPPc (Figure 3.11 (i)), with the first shallow step, between 100 and 280°C, suggesting some solvent loss [23]. The second main decomposition step from ~280 – 500°C is associated with functional group decomposition i.e. of the groups associated with the complexes e.g. –COOH groups [24]. Overall a 50% weight loss occurred for the Pc at 500 °C. This decomposition profile is typical for phthalocyanine complexes as they are known to be highly thermally stable, showing no evidence of melting, only decomposition at higher temperatures [25]. The decomposition profile for the conjugate showed a marked increase in weight loss (45% at 250 °C), followed by a further, shallower decomposition step from 250 – 500 °C where 25% was additionally lost. This composite was found to be hygroscopic and thus the first weight loss may be attributed to solvent loss. The 2<sup>nd</sup> decomposition step is due to removal of the remainder of the organic groups on the surface of the nanoparticle. Thus the conjugate was observed to be less thermally stable as overall a 70% weight loss was observed for (4) as compared to ZnTCPPc (3) alone and the Si-Gd<sub>2</sub>O<sub>3</sub> NP (2) which showed a weight loss of ~50% overall at 500 °C.

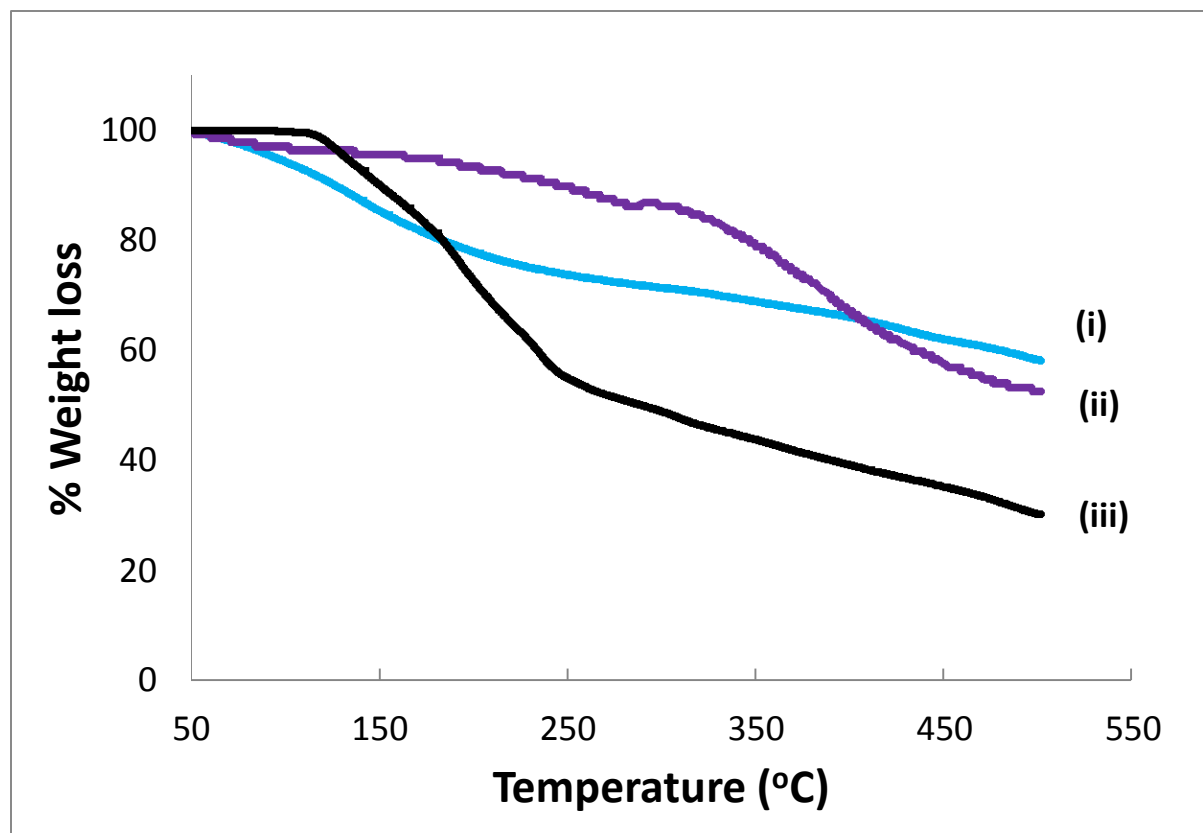


Figure 3.11: TGA profiles of (i) Si-Gd<sub>2</sub>O<sub>3</sub> NP (2), (ii) ZnTCPPc (3) and (iii) ZnTCPPc-Gd<sub>2</sub>O<sub>3</sub>-conjugate (4) at a heating rate of 10 °C/min to 500 °C under a nitrogen atmosphere with a gas flow rate of 120 ml/min.

### 3.2.2.5 X-ray diffraction

The XRD patterns for ZnTCPPc (3) and the conjugate (4) only showed a broad reflection at  $\sim 2\theta = 28^\circ$  which is typical for phthalocyanines [26] together with the reflections observed for the Si-Gd<sub>2</sub>O<sub>3</sub> NPs (2) alone. No real information about the composite structure was obtained from XRD.



### 3.2.2.6 Electron paramagnetic resonance

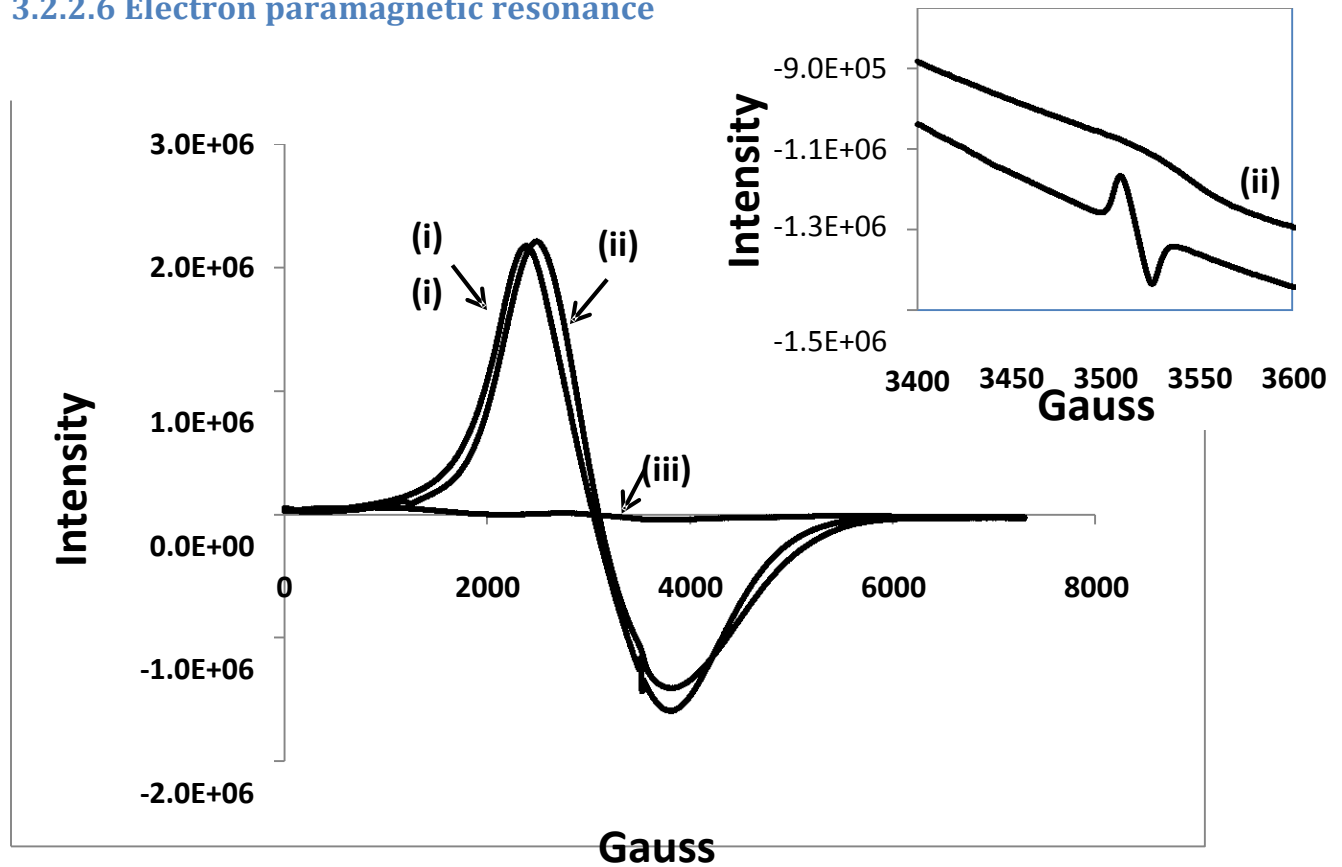


Figure 3.12: EPR spectra acquired at room temperature in the solid state for (i) ZnTCPPc (**3**), (ii) ZnTCPPc-SiGd<sub>2</sub>O<sub>3</sub> NP (conj) (**4**) and (iii) ZnTCPPc-SiGd<sub>2</sub>O<sub>3</sub> NP (mix) (**5**). Inset: Zoomed in section (3400 – 3600 G) for the ZnTCPPc (i) and the conjugate (ii).

Figure 3.12 shows the EPR spectra acquired for the ZnTCPPc (**3**), the conjugate (**4**) and the mixed (**5**) complexes –in the solid state, to at room temperature. The conjugate showing a small shift to a higher field, from 2288 to 2345 G as compared to ZnTCPPc, appears to be rather similar to that of the Pc (**3**) alone. The mix (**5**) on the other hand shows characteristics that are reminiscent of the EPR spectra acquired for the NPs themselves, i.e. weak, broad signals, suggesting that the conjugate formation exerted some change in the NP physical properties, while a simple mix did not.

EPR spectra of unsubstituted zinc phthalocyanines have been studied and single, narrow, intense EPR signals centered at  $g = 2.0036$  with a line width of 4.25 G both in chloroform and in the solid



state (at 290 K and at 100 K) were obtained. In our case, in addition to the obvious broad signal obtained for the ZnTCPPc alone, a small, narrow, sharp signal line centered at 3518 G was also observed (Figure 3.11, inset). The conjugate, on the other hand, showed a broad, shallow step centered at 3544 G, suggesting some change having taken place upon conjugate formation.

### 3.3. Photophysical studies

#### 3.3.1. Fluorescence quantum yields ( $\Phi_F$ ) and lifetimes ( $\tau_F$ )

The fluorescence behaviour of ZnTCPPc-SiGd<sub>2</sub>O<sub>3</sub> NP (conj) and ZnTCPPc-SiGd<sub>2</sub>O<sub>3</sub> NP (mix) in DMSO showed that the fluorescence emission spectra were mirror images of their excitation spectra confirming the lack of aggregation in the solution and that there is no change in the symmetry of the molecule upon excitation (Figure 3.13 A and B). However, the absorption spectrum of ZnTCPPc-SiGd<sub>2</sub>O<sub>3</sub> NPmix (Figure 3.13 B) showed a narrower Q band than the excitation spectra. The Stokes shift for the ZnTCPPc-SiGd<sub>2</sub>O<sub>3</sub> NP (conj) and ZnTCPPc-SiGd<sub>2</sub>O<sub>3</sub> NP (mix) were found to be 11 and 9 nm respectively, which is typical for phthalocyanine complexes; i.e. emission occurs at longer wavelengths than absorption, with Stokes shifts ranging from 3 nm to 19 nm [27] as tabulated in Table 3.2.

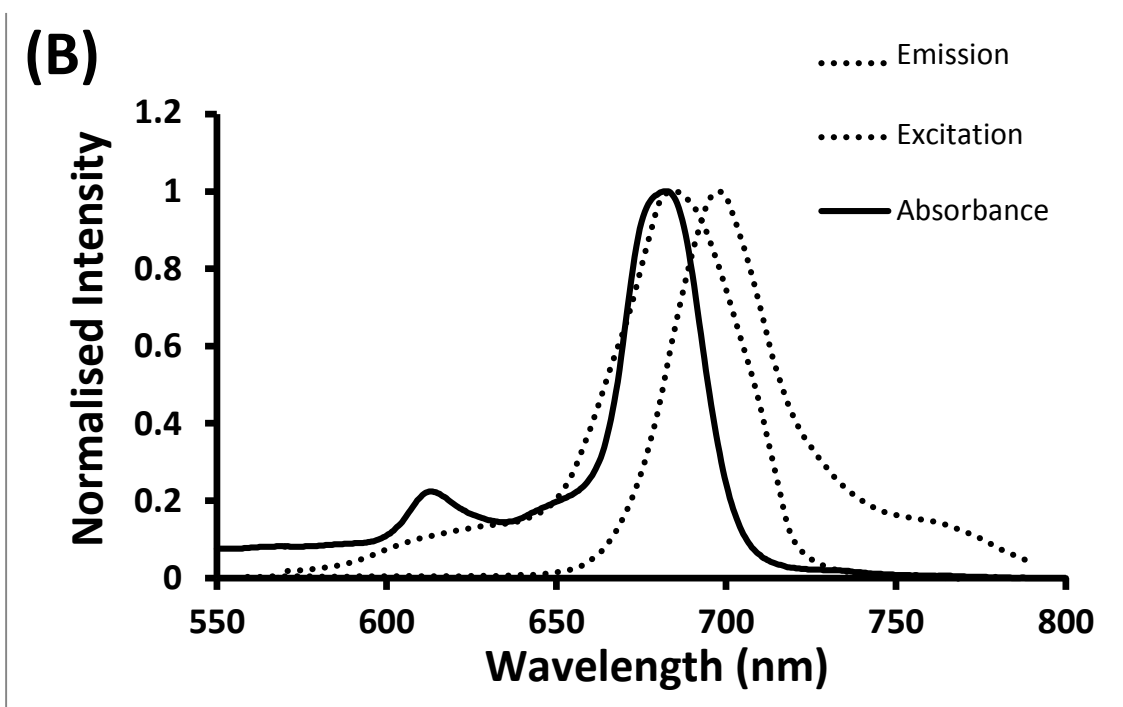
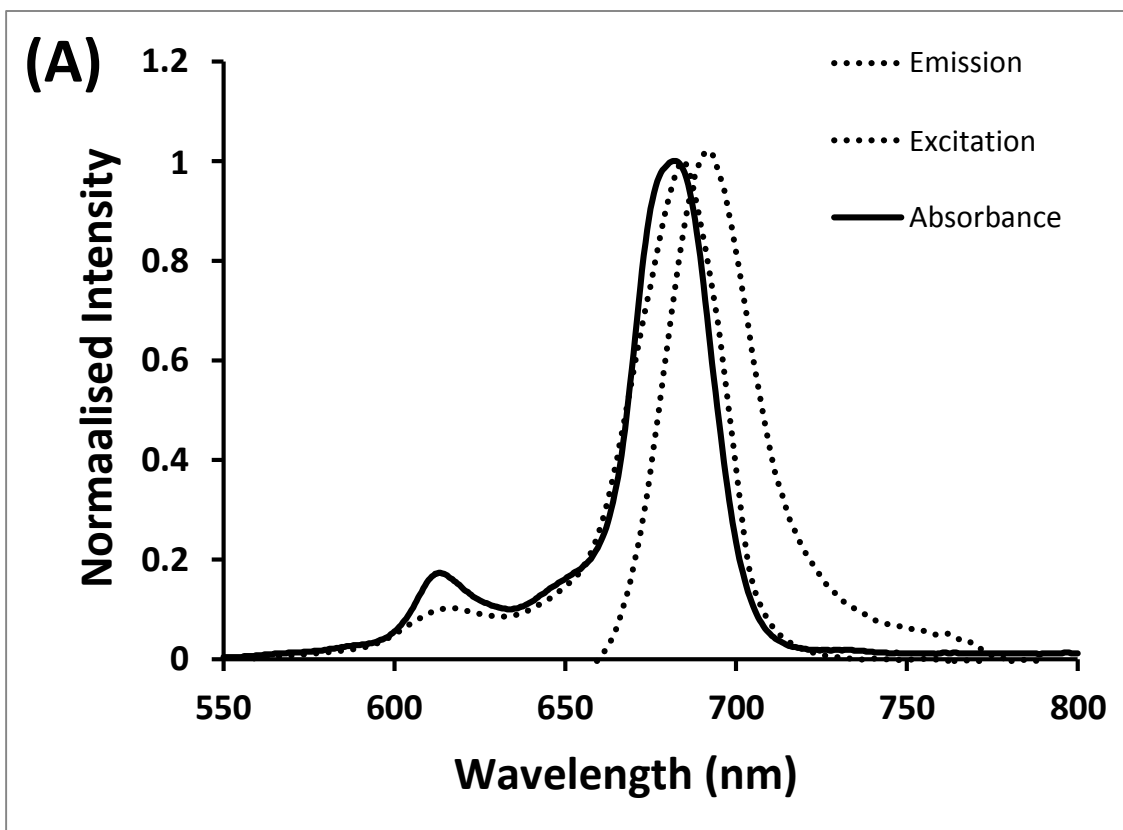


Figure 3.13: Normalized absorption, fluorescence emission and excitation spectra of (A) ZnTCPPc-SiGd<sub>2</sub>O<sub>3</sub> NP (conj) and (B) ZnTCPPc-SiGd<sub>2</sub>O<sub>3</sub> NP(mix) in DMSO ( $\lambda_{exc}$ = 610 nm).

The fluorescence quantum yields ( $\Phi_F$ ) values were determined by the comparative method and the values were found to decrease by 0.09 upon conjugation with the gadolinium oxide nanoparticles. Fluorescence quantum yields are often influenced by the heavy atom effect and aggregation tendencies, which increase upon conjugation and thus a decrease in the fluorescence quantum yield [28, 29] is usually observed. The low  $\Phi_F$  values of 2.31 (indicated in Table 3.2) are therefore expected for the conjugate and mixed samples as intersystem crossing (ISC) to the triplet state is expected to be enhanced due to the presence of Gd in the NP system (heavy atom effect). ISC to the triplet state increases the triplet quantum yield but it inevitably shortens the fluorescence lifetimes and quantum yields of the **singlet** excited states, hence the observed low fluorescence quantum yields for the conjugates [30] shown in Table 3.2.

Fluorescence lifetimes for MPc complexes are short, and are strongly dependent on the solvent used, the nature of the central metal ion, and nature of substituents on the Pc molecule. Fluorescence lifetimes were obtained for the ZnTCPPc (**3**), ZnTCPPc- Gd<sub>2</sub>O<sub>3</sub> NPs (conj, **4**) and ZnTCPPc-SiGd<sub>2</sub>O<sub>3</sub> NPs (mixed, **5**). The decay curves are shown in Figure 3.14. All complexes show bi-exponential fluorescence decay curves. The decrease in fluorescence lifetimes for the phthalocyanines alone have been explained as being due to the formation of aggregates which are non-fluorescent, but which can quench the monomer [31] (though the aggregates are not easily apparent in the UV/Vis spectra).

The fluorescence lifetime of the Pc decreased after conjugation and after mixing, which illustrates that the Pc's fluorescence was quenched by the mere presence of the gadolinium oxide nanoparticles. The decrease was much greater upon conjugation as compared to mixing. Two lifetimes for the conjugates could be related to the different orientations of the phthalocyanine on the nanoparticles. It has been reported that when a fluorophore is in close proximity with a metal, the fluorophore interacts with the free electrons on the surface of the metal modifying its fluorescence behaviour [32]. This results in an increase or a decrease in the fluorescence lifetime depending on the orientation of the fluorophore to the metal and the distance between the fluorophore and the metal [33, 34].

The quenching of the lifetimes may be explained using fluorescence radiative lifetimes ( $\tau_0$ ) calculated using equation 1.2:

$$\tau_0 = \tau_F / \Phi_F \quad (1.2)$$

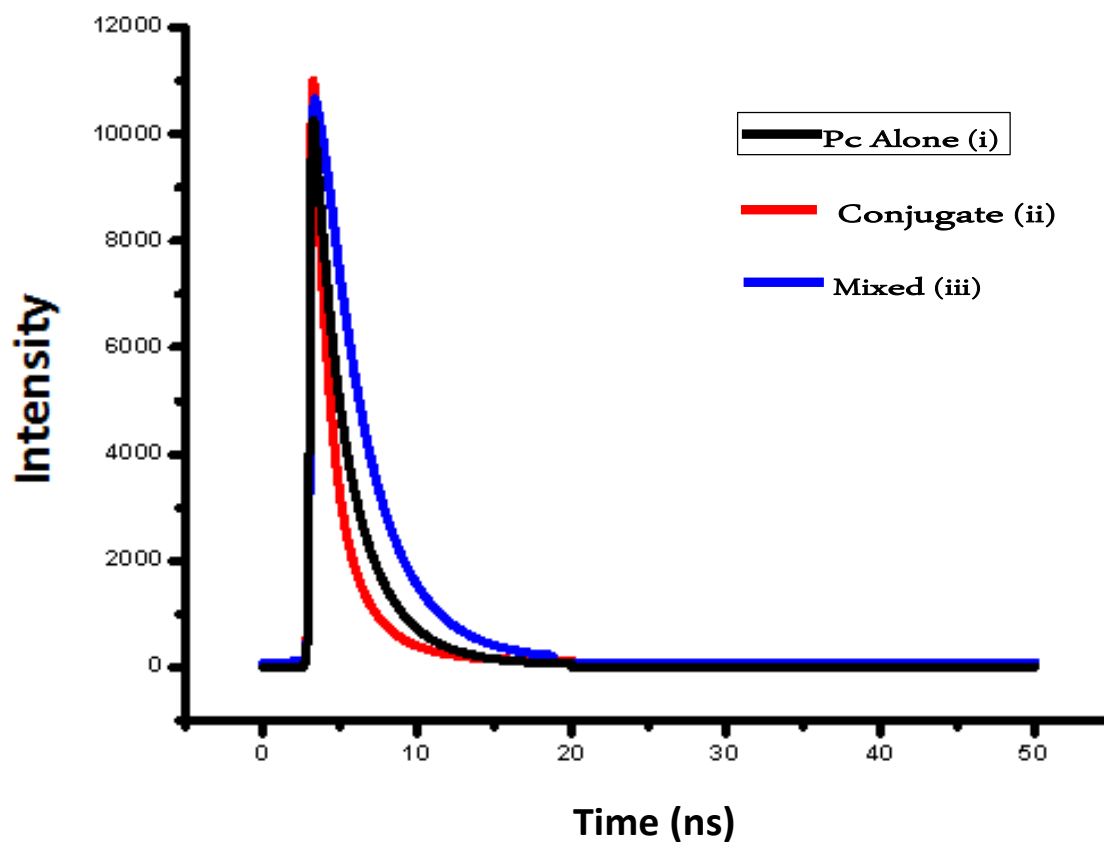


Figure 3.14: Fluorescence lifetime decay curves of (i) ZnTCPPc (3) alone, (ii) ZnTCPPc - Gd<sub>2</sub>O<sub>3</sub> NPs conjugate (4) and (iii) the mixture in DMSO. Exc.  $\lambda$  = 689 nm.

**Table 3.2: Sizes of the NPs, absorbance, photophysical and photochemical results of the Pc components.**

Complex	Solvent	$\lambda_{abs}$ (nm)	$\lambda_{em}$ (nm)	$\Phi_F$	$\tau_F$ (ns)	$\tau_0$ (ns)	$\Phi_T$	$\tau_T$ ( $\mu$ s)	$\Phi_\Delta$
ZnTCPPc (3)	DMSO	679	689	0.27	2.53 0.79	9.37	0.61	319.25	0.32
ZnTCPPc-Si- Gd <sub>2</sub> O <sub>3</sub> NPs (4)	DMSO	679	690	0.18	2.31 0.68	12.83	0.69	306.97	0.36
ZnTCPPc- Gd <sub>2</sub> O <sub>3</sub> NPs mixed (5)	DMSO	679	688	0.12	2.35 0.65	19.58	0.69	313.76	0.49

### 3.3.2. Triplet quantum yields ( $\Phi_T$ ) and lifetimes ( $\tau_T$ )

Figure 3.15 shows the triplet decay curves for the ZnTCPPc (3), conjugate (4) and mixed (5) samples in DMSO. Triplet quantum yield ( $\Phi_T$ ) is a measure of the fraction of absorbing molecules that undergo intersystem crossing to the meta-stable triplet excited state. The triplet decay curves of all the complexes displayed first order decay profiles. The triplet state parameters ( $\Phi_T$ ,  $\tau_T$ ), were determined experimentally using laser flash photolysis. The values obtained for  $\Phi_T$  and  $\tau_T$  are tabulated in Table 3.2. The triplet quantum yields were found to be 0.61, 0.69 and 0.69 for the ZnTCPPc, ZnTCPPc-Si-GdNP (conj) and ZnTCPPc-Si-GdNP (mixed), respectively. The triplet quantum yield increased for the conjugate and the mixed as compared to the Pc alone. Lower triplet lifetimes were obtained after conjugation and mixing. However, based on the increased quantum yields of the conjugate and the mix, it is expected that these complexes will most likely be efficient in singlet oxygen generation.

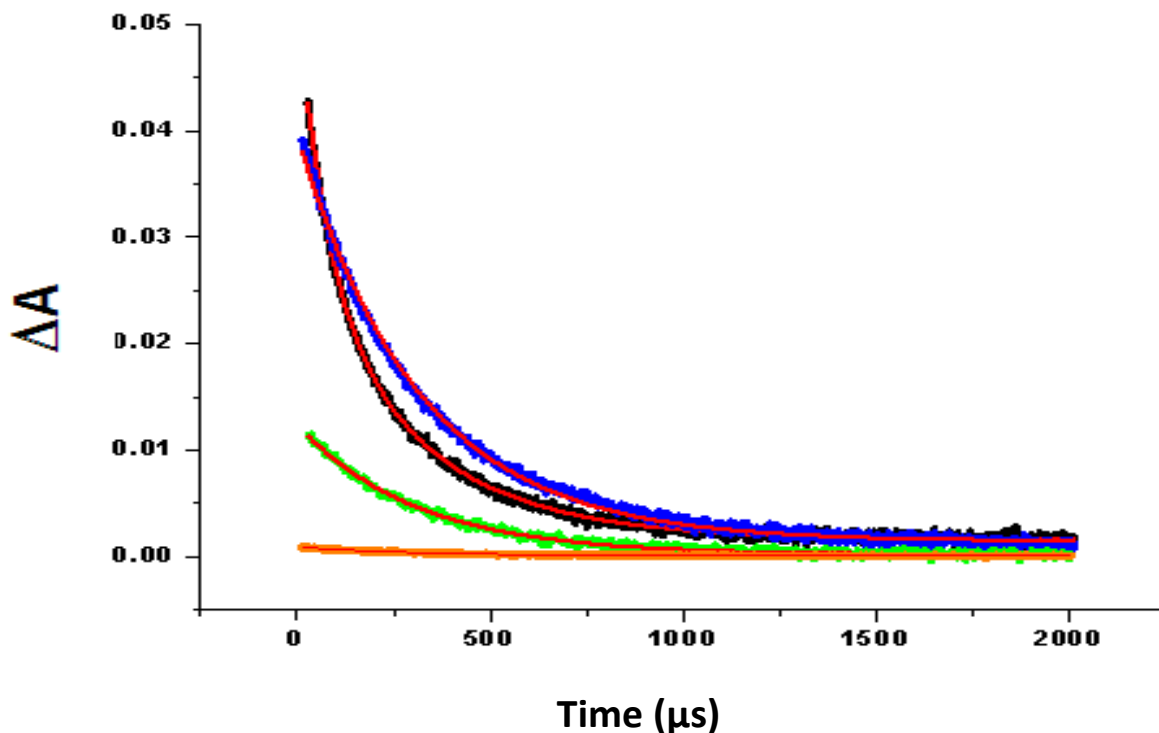


Figure 3.15: Triplet decay curves for the synthesized complexes in DMSO at 490 nm. Exc.  $\lambda = 682$  nm.

### 3.3.3. Singlet oxygen quantum yields ( $\Phi_{\Delta}$ )

In this work, the singlet oxygen quantum yields of the complexes were determined using a chemical method, i.e. using DPBF in DMSO. Singlet oxygen quantum yield ( $\Phi_{\Delta}$ ) values are expected to depend on the corresponding triplet quantum yield ( $\Phi_T$ ) values of the photosensitizer, since it is the species in the triplet state which results in the production of singlet oxygen, and the triplet state lifetimes, efficiency of energy transfer (which depends on the energy of the triplet state) amongst other factors all give an indication of the singlet oxygen generation efficiency of the sensitizer [35]. That is, if the triplet state of a photosensitizer is highly populated, the excited sensitizer can then interact with ground state triplet molecular oxygen exciting it to



its singlet excited state to a greater extent. Though there is no direct correlation, an increase in  $\Phi_T$  signifies an increase in  $\Phi_\Delta$  as shown in Table 3.2.

Figure 3.16 shows the decay of DPBF (a singlet oxygen quencher) with time for ZnTCPPc. No significant decrease in the Q band of the Pc for the period of irradiation time was observed suggesting that the phthalocyanine had not degraded and was stable over the study. DPBF degrades due to the singlet oxygen being produced by Pc complexes. The decrease of DPBF was monitored at  $\sim 417$  nm and the rate of decay of DPBF is directly related to the production of singlet oxygen species. The conjugate and mix showed stable Q bands for the Pc and a steady decrease in the DPBF band. The conjugate and the mix showed an improved ability to generate singlet oxygen (shown in Table 3.2) with  $\Phi_\Delta$  values of 0.36 as compared to the 0.32 obtained for the Pc alone. Thus we observe a higher  $\Phi_\Delta$  for the conjugate and the mix ( $\Phi_\Delta 0.49$ ) as compared to the Pc alone. An increase of 0.04 and 0.17 for the conjugate and the mixed respectively, shows that the increase is significant particularly for the mixed sample and therefore the overall efficiency of the Pc is enhanced by the presence of the  $Gd_2O_3$  NP, with or without formation of a covalent bond.

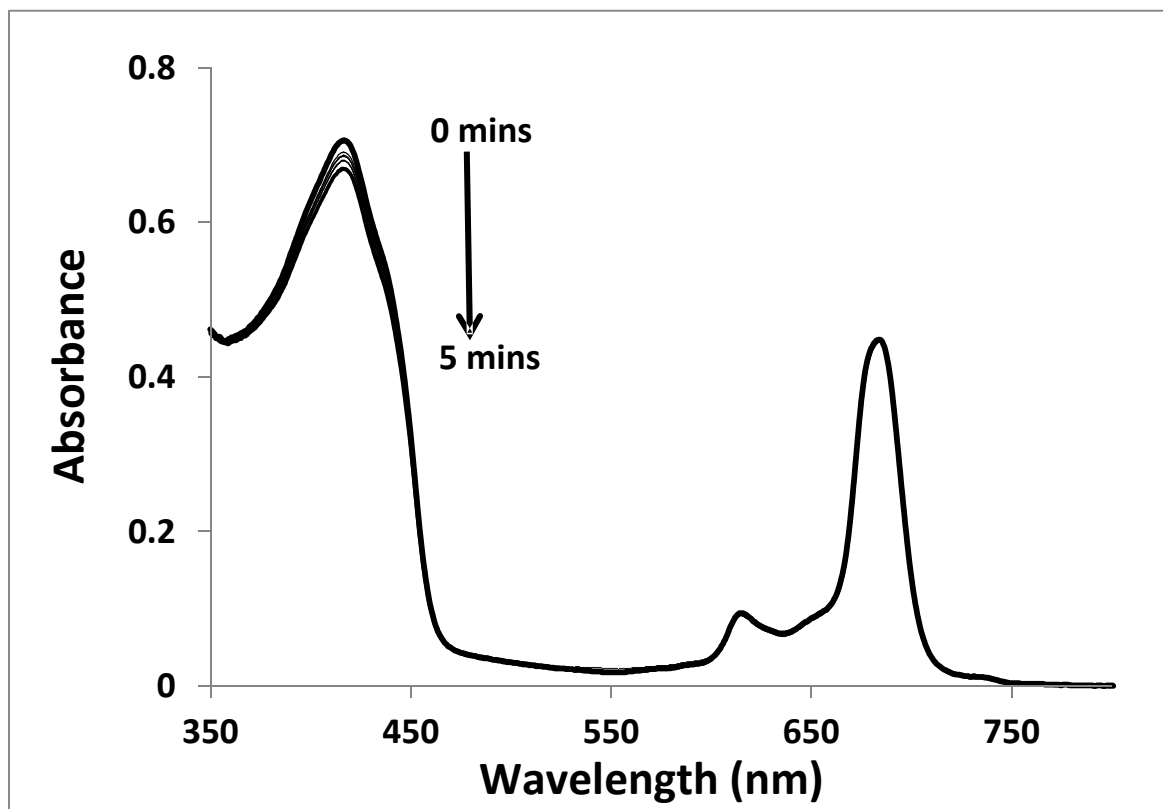


Figure 3.16: Photodegradation of DPBF in the presence of ZnTCPPc in DMSO. [ZnTCPPc] =  $4.8 \times 10^{-6}$  M and [DPBF] =  $2.5 \times 10^{-5}$  M.

### 3.4 References

1. R. Bazzi, M. Flores-Gonzalez, C. Louis, K. Lebbou, C. Dujardin, A. Brenier, W. Zhang, O. Tillement, E. Bernstein, P. Perriat. *J. Lumin* 102 (2003) 445.
2. P. Granitzer, K. Rumpf, A.G. Roca, M. P.Morales, P. Poelt, M. Albu, J. Magn. and Magn. Mater.,322 (2010) 1343.
3. D.W. Mayo, F.A. Miller and R.W. Hannah, *Course Notes on the Interpretation of Infrared and Raman Spectra*, John Wiley and Sons, Inc., New Jersey, (2004) 5.
4. J. Ho Chang, K. Ho Kang, J. Choi, Y. K. Jeong, *Superlattices Microstruct.*, 44 (2008) 442.
5. D.W. Mayo, F.A. Miller and R.W. Hannah, *Course Notes on the Interpretation of Infrared and Raman Spectra*, John Wiley and Sons, Inc., New Jersey, (2004) 5.
6. A. Bianco, K. Kostarelos, C.D. Partidos, M. Prato, *Chem. Commun.* (2005) 571.
7. M. E. Park, J. Ho Chang, *Mater. Sci. Eng., C*, 27 (2007) 1232.
8. Liangjun Zhou,ac Zhanjun Gu,Xiaoxiao Liu,Wenyan Yin,Gan Tian,D Liang Yan,Shan Jin,C Wenlu Ren,a Gengmei Xing,a Wei Li,Xueling Chang,Zhongbo Huc and Yuliang Zhao *J. Mater. Chem.*, 22 (2012)966.
9. H. Fong, D.H. Reneker, *J. Polym. Sci. B.*, , 37 (1999) 3488
10. T.H. Tran-Thi , C. Desforge, C. Thiec, *J. Phys. Chem.* 93 (1989) 1226.
11. J. F. Watts, J. Wolstenholme, *An Introduction to Surface Analysis by XPS and AES*. Wiley-VCH , (2003) 224.
12. P. Kubat, J. Mosinger, *J. Photochem. Photobiol. A :Chem.* 96 (1996) 93.
13. T.H. Tran-Thi , C. Desforge, C. Thiec, *J. Phys. Chem.* 93 (1989) 1226.
14. D. Raiser and J.P. Deville, *J. Electron. Spec.* 57 (1991)
15. M.R. Alexander,R.D. ShortF.R. JonesW. MichaeliC.J. Blomfield, A study of HMDSO/O<sub>2</sub> plasma deposits using a high-sensitivity and -energy resolution XPS instrument: curve fitting of the Si 2p core level. 137 (1999) 179.
16. S. Watcharinyanon, D. Nilsson, E. Moons et al., "A spectroscopic study of self-assembled monolayer of porphyrin- functionalized oligo(phenyleneethynylene)s on gold: the influence of the anchor moiety," *Physical Chemistry Chemical Physics*, 10 (2008) 5264..

17. D. T. Edwards, Z. Ma, T.J. Meada, D. Goldfarb, S. Han, M.S. Sherwin. Extending the distance range accessed with continuous wave EPR with Gd 3+ spin probes at high magnetic fields. *Phys. Chem.* 25 (2002) 11313.
18. K. Takeshita, et al. *Chem. Pharm. Bull.* 60 (2012) 31.
19. Y. Li, T. M. Pritchett, J. Huang, M. Ke, P. Shao, W. Sun. *J. Phys. Chem. A* 112 (2008) 7200.
20. M. O. Liu, C. H. Tai, A. T. Hu, T. H. Wei, *J. Organomet. Chem.*, 689 (2004) 2138
21. J. C. Love, L. A. Estroff, J. K. Kriebel, R. G. Nuzzo, G. M. Whitesides, *Chem Rev.*, 105 (2005) 1103.
22. A. Ogunsiye, D. Maree, T. Nyokong, *J. Mol. Struct.* 650 (2003) 131.
23. X. Wang, Y. Liu, W. Qiu, D. Zhou, *J. Mater. Chem.* 12 (2002) 1636.
24. B. Ballesteros, G. de la Torre, C. Ehli, G.M. Aminur Rahman, F. Agullo-Rueda, D.M. Guldi, T. Torres, *J. Am. Chem. Soc.* 129 (2007) 5061.
25. R. Seoudi, G.S. El-Bahy, Z.A. El Sayed, FTIR, TGA and DC electrical conductivity studies of phthalocyanine and its complexes. 753 (2005) 119.
26. T. N. Kuznetsova, E.A. Makarova, S.N. Dashkevich, N.S. Gretsova, E.A. Kalmykova, V.M. Negrimovsky, O.L. Kaliya, E.A. Lukyanets, *Russ. J. Gen. Chem.*, 70 (2000) 140.
27. M. O. Liu, C. H. Tai, A. T. Hu, T. H. Wei, *J. Organomet. Chem.*, 689 (2004) 2138
28. A. Gilbert, J.E. Baggott in: *Essentials of Molecular Photochemistry*, Blackwell Scientific, Oxford, (1991).
29. J. G. Calvert, J. N. Pitts, *Photochem.*, 285 (1967) 258.
30. J. R. Darwent, P. Douglas, A. Harriman, G. Potter, M. C. Richoux, *Coord. Chem. Rev.*, 44 (1982) 83.
31. C.D. Geddes, J.R. Lakowicz, *J. Fluoresc.*, 12 (2002) 121
32. J. A. Lacey, D. Philips, *Photochem. Photobiol. Sci.*, 1 (2002) 378.
33. J.R. Lakowicz, Y. Shen, S. D'Auria, J. Malicka, J. Fang, Z. Gryczynski, I. Gryczynski, *Anal. Biochem.*, 301 (2002) 261
34. C.D. Geddes, J.R. Lakowicz (Eds.), *Topics in Fluorescence Spectroscopy*, Springer, New York, 2005
35. L. Kaestner, M. Cesson, K. Kassab, T. Christensen, P.D. Edminson, M.J. Cook, T. Chambrier, G. Jori, *Photochem. Photobiol. Sci.*, 2 (2003) 660.

# **Chapter 4**

## **Electrospun nanofibers**

This work reports on the study of the effect of electrospinning solution parameters on the morphology and size of fibers. Moreover, the microscopic, spectroscopic and photophysical and photochemical behavior of phthalocyanine and phthalocyanine-gadolinium nanoparticle functionalized electrospun polymer fibers is studied.

## 4 Electrospun polymer fibers

### 4.1. Influence of electrospinning conditions on morphology of polymer fiber

Electrospun polymer fibers have a wide range of applications due to their porosity, small pore sizes and high surface area to volume ratio [1-4]. Their uniformity and morphology, however, are heavily dependent on a number of factors during the production processes which include the polymer molecular weight, polymer concentration, viscosity, conductivity, surface tension and volatility of solvents (solution properties), applied voltage, flow rate, tip-to-collector distance and temperature, humidity and atmospheric pressure (ambient parameters), collector composition and geometry (processing parameters).

In this work, before functionalization of the electrospun polymer fibers with phthalocyanines for various applications **was** attempted, the effect of some of the electrospinning conditions (including polymer concentration, viscosity, conductivity and solvent ratio) on the morphology of the fibers and fiber diameter was investigated. Different grades of Polyamide 6 (B24, B27, B32 and B36 with average molecular weights of 70,000, 80,000, 90,000 and 10,000 g/mol) were used as the model polymer. The average fiber diameter for the fiber mats was used in this work to assess the effect of these electrospinning conditions.

#### 4.1.1 Effect of polymer viscosity and conductivity on fiber morphology

Some physical properties (viscosity and conductivity) of the as-prepared solutions were measured and the results are summarized in Table 4.1. This table (Table 4.1), together with Figure 4.1 shows that by increasing the concentration (for all polymer grades), the polymer viscosity increases (Figure 4.1), as does the conductivity of the polymer solution (Figure 4.2). The molecular weight of a particular polymer molecule is a product of the degree of polymerization and the molecular weight of the repeating unit. The viscosity change was found to be the greatest for B36, the largest molecular weight polymer (Figure 4.1). This is thought to be due to the electrical properties, surface tension and the viscosity of the solution;

all of which determine the amount of stretching that can take place in electrospinning the solution. In general, by fixing the polymer concentration (e.g. at 16%), increasing polymer molecular weights (from B24 to B36) were found to increase the solution viscosity and conductivity. Since the molecular weight represents the length of the polymer chain, viscosity is expected to increase with the molecular weight because the degree of entanglement is greater for longer chains. These results are in agreement with the literature [5].

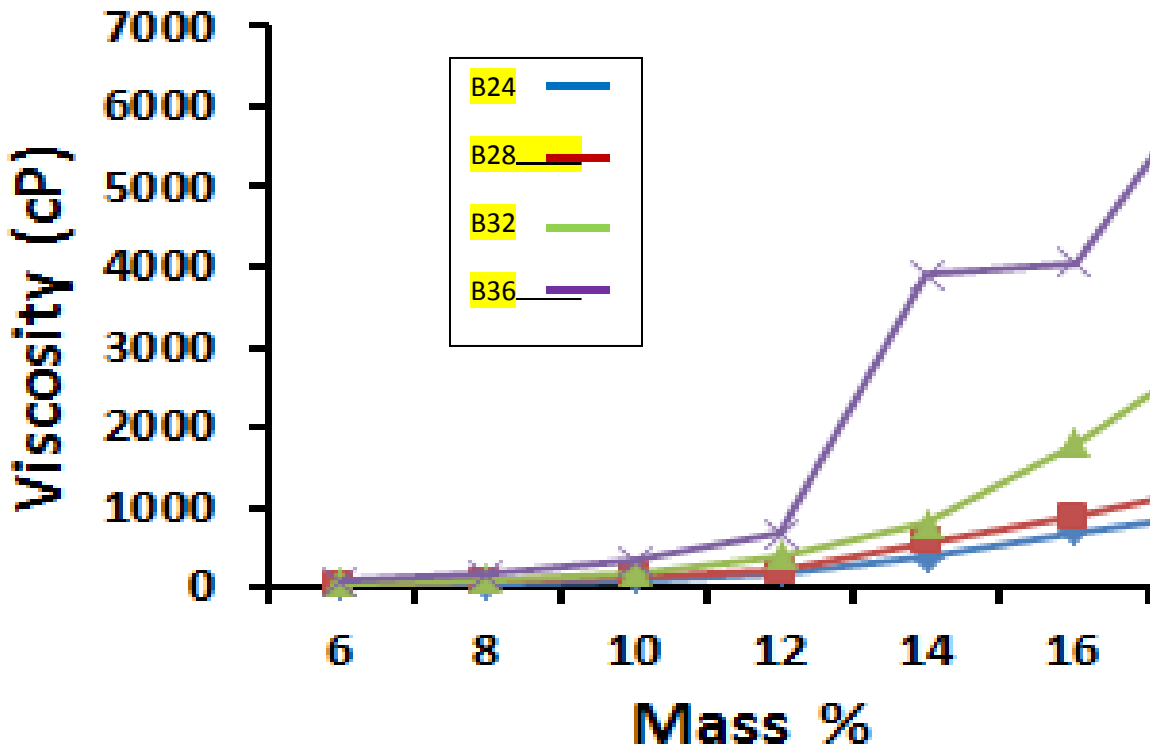


Figure 4.1: Plot of the changes in viscosity with increasing polymer concentration for the different polymer grades.

**Table 4.1: The effect of polymer solution concentrations (for the different polyamide grades) on the viscosity and conductivity parameters (solvent used: 50:50 (FA:AA)).**

<b>Polymer Grade</b>	<b>Polymer Concentration (wt%)</b>	<b>Viscosity (cP)</b>	<b>Conductivity (mS/cm)</b>
<b>B24</b>	6	14	0.502
	8	41	0.591
	10	100	0.643
	12	183	0.678
	14	384	0.716
	16	690	0.739
<b>B27</b>	6	35	0.583
	8	75	0.623
	10	141	0.646
	12	208	0.691
	14	576	0.722
	16	885	0.739
<b>B32</b>	6	47	0.494
	8	101	0.566
	10	188	0.633
	12	389	0.686
	14	796	0.699
	16	1802	0.700
<b>B36</b>	6	69	0.543
	8	156	0.562
	10	336	0.653
	12	682	0.674
	14	3911	0.678
	16	4049	0.766



### 4.1.2 Effect of polymer concentration on fiber morphology

The average fiber diameter for the electrospun fibers of the polymers were used also to assess the effect of polymer concentration on the fiber morphology (Table 4.2). Overall the fiber diameters were generally found to increase with increasing polyamide weight (e.g. 10 wt% for B24, B27, B32, B36). Polymer solutions at higher concentrations were virtually solidifying (drying up) during the electrospinning process resulting in very large fiber diameters. The SEM images in Figure 4.3 also show that as the concentration of the polymer solution increases, the viscosity and fiber diameter also increases. In order to obtain a small fiber diameter, the solution concentration should be as low as possible, which is useful in many applications of fibers essential for filtering. However, at low polymer concentrations (i.e., lower viscosity); defects in the form of beading and droplets were observed. This is a result of electro spraying instead of spinning.

### 4.1.3 Effect of solvent ratios in polymer solutions

The solvent system used for this study was formic acid and acetic acid in varying ratios. As stated by De Schoenmaker [et al.](#), polyamide-6 dissolves in formic acid (FA) and not in acetic acid (AA), however, acetic acid acts as a stabilizer and is required for electrospinning to occur [7]. In order to investigate the effect of the solvent system on the morphological appearance of the as-spun PA-6 fibers, the polymer solutions were prepared by dissolving the pellets firstly in 1:1 formic acid: acetic acid and then 1:3 acetic acid (AA): formic acid (FA). Interestingly, the viscosity of the solutions was found to markedly increase, and the conductivity increased appreciably with the addition of increasing amounts of formic acid (Figure 4.2 and Table 4.2). The increase in the conductivity of the solutions with increasing amounts of formic acid could be the result of the much higher dielectric constant of formic acid (58.5 at 15.6 °C) in comparison with that of acetic acid (6.8 at 20.9 °C) [6]. Therefore formic acid with its high polarity largely determines the charge distribution in the jet. An increase in conductivity with increasing amounts of FA implies a decrease in surface tension, resulting in larger fiber diameters (since steady Taylor cones are facilitated at higher viscosities). Solutions with 3:1 volume ratios of AA:FA were found to be more

electrospinnable than those of 1:1 volume ratios of AA:FA. Table 4.2 shows the larger fiber diameters obtained for the samples with an increase in polymer molecular weight, polymer concentration and volume of formic acid.

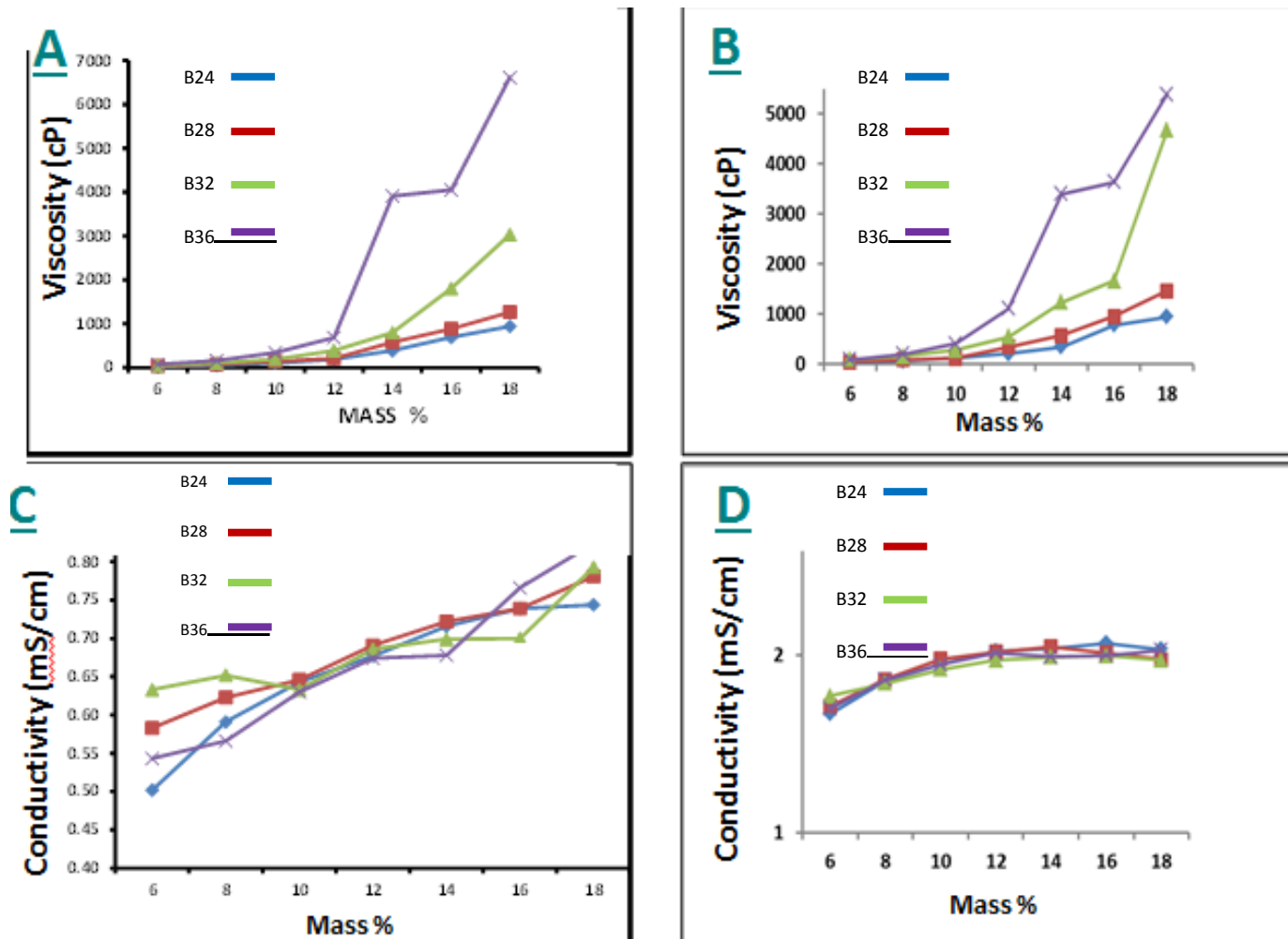


Figure 4.2: Plots showing the effects of varying the acetic acid:formic acid solvent ratio on the viscosity and conductivity of the different polymer grades: where (A) and (C) are the viscosity and conductivity results obtained for the 1:1 FA:AA solvent system respectively; while (B) and (D) are the viscosity and conductivity results obtained for the 3:1 FA:AA solvent system.

**Table 4.2: The effect of solvent ratio (FA:AA), polymer concentration and molecular weight on the fiber diameter (in  $\mu\text{m}$ ).**

<b>Polymer Concentration (wt %)</b>	<b>1:1 vol % FA:AA</b>				<b>3:1 vol % FA:AA</b>			
	<b>B24</b>	<b>B27</b>	<b>B32</b>	<b>B36</b>	<b>B24</b>	<b>B27</b>	<b>B32</b>	<b>B36</b>
<b>10</b>	58	57	90	96	66	81	80	105
<b>12</b>	65	69	131	151	70	96	108	138
<b>14</b>	95	79	160	234	103	112	141	246
<b>16</b>	109	106	209	304	113	127	154	457

- Fiber diameter in micrometers ( $\mu\text{m}$ ).

## **4.2 Characterization of electrospun polymer fibers functionalized with the ZnTPCPC and their photochemical behaviour**

Most applications for phthalocyanines are done in solution media; however there are others, e.g photocatalysis, which are more preferable on solid media, like fibers. These solid systems offer comparably better advantages like ease of recovery [8]. In this chapter the phthalocyanines were supported on electrospun fibers and this section discusses the characterization of phthalocyanine and phthalocyanine-Gd<sub>2</sub>O<sub>3</sub> NP functionalized fibers.

Polyamide 6 (i.e., B32, 14 wt %, 1:1 FA/AA) was used in the study due to its tough, high tensile strength, relative flexibility and resistance to chemical degradation and heat. B32 14 wt % was found to be the best molecular weight, concentration and solvent system because it showed no clogging and dripping of the polymer solution and furthermore the Taylor cone was stable therefore producing fibers with best morphology, i.e a consistent, small fiber diameter.

The embedding of the nanocomposite in the fiber did not follow covalent bond formation, but physical mixing (i.e. the conjugate **(4)** or mixed **(5)** samples were simply added to the polymer solution). This has the advantage that varying amounts of the phthalocyanines can be added to the polymer until the onset of leaching of the phthalocyanine from the polymer in aqueous photocatalytic applications. It was possible to covalently bind the polymer to the carboxylic acid group of the phthalocyanine through an amide bond to the N-H functionality of the polymer; however, due to time constraints this study was not done. Three sets of electrospun fibers were prepared using the B32 polymer grade, 14%: 1) a Pc functionalized fiber (ZnTCPPc,**2**), 2) a Pc NP-conj fiber (PA-6/ZnTCPPc-Gd<sub>2</sub>O<sub>3</sub> NPs-conj, **4**), and finally 3) the composite where the Pc was simply mixed with the Gd<sub>2</sub>O<sub>3</sub> NPs (PA-6/ZnTCPPc-GdNPsmix, **5**).

#### 4.2.1. Microscopic characterization

Fiber diameter and morphology of the electrospun fibers were assessed using Scanning Electron Microscopy (SEM). The average diameters of the electrospun fibers of each polymer alone and those when functionalized with phthalocyanine or phthalocyanine-Gd<sub>2</sub>O<sub>3</sub> NPs were determined using Cell<sup>^</sup>D software from Olympus. Both the functionalized and unfunctionalized polyamide fibers that were formed had controllable fiber diameters and consisted of fibers that were, on the whole, defect free (no beads present).

From the SEM images (Figure 4.3), with lower polymer concentrations, the presence of junctions and bundles, indicating that the fibers were still wet when reaching the collector are observed. However, by increasing the solution viscosity, through increasing the polymer concentration, uniform fibers with few beads and junctions were obtained. These samples consisted of continuous, single fibers with defect-free fiber surfaces and consistent fiber diameters as shown in Figure 4.3. The electrospun fibers of the polyamide polymer alone and those functionalized with the phthalocyanine complexes (Figure 4.4) were wholly uniform and defect free i.e. they did not form an appreciable amount of beads under the experimental conditions (Figure 4.4).

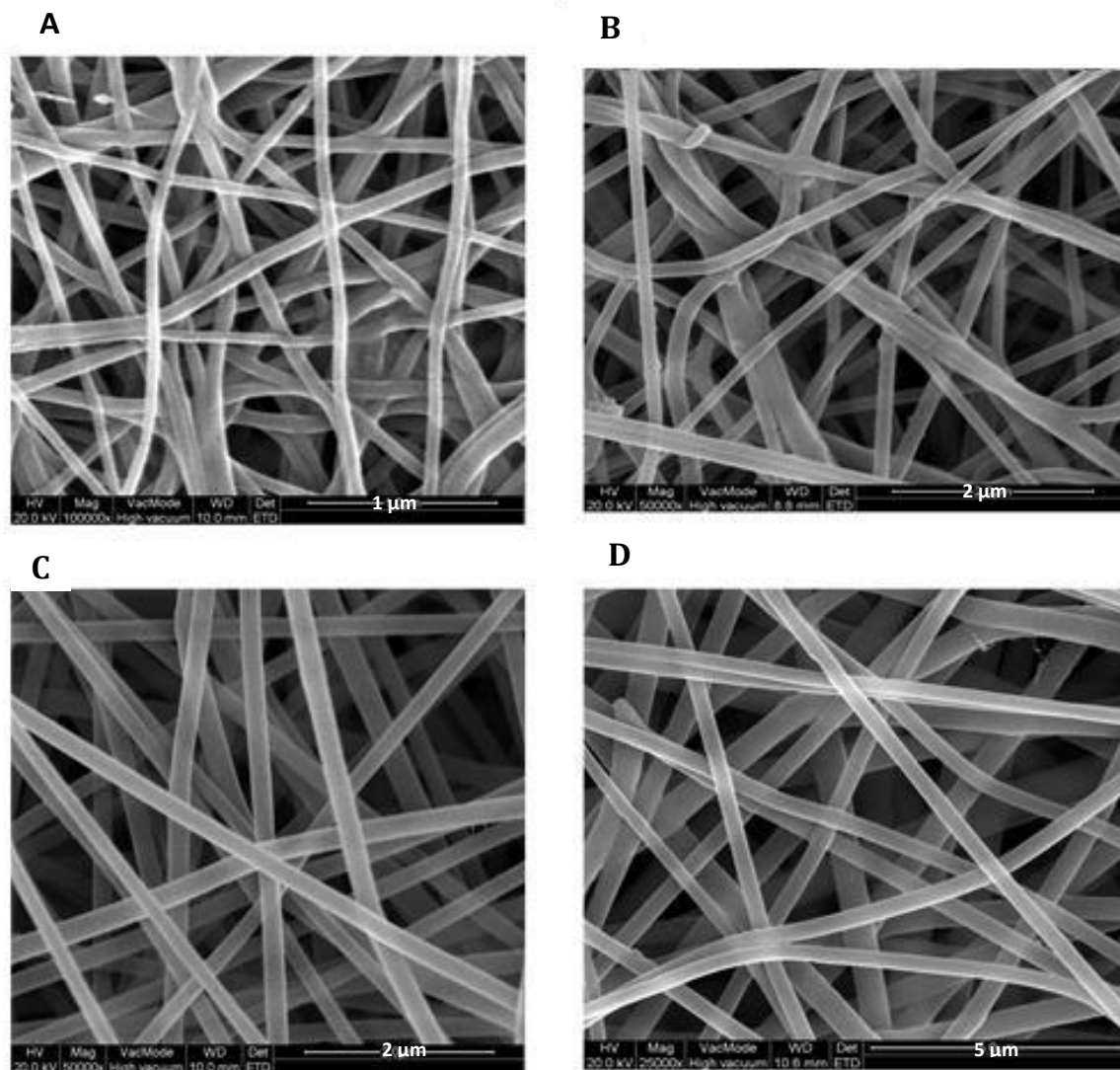


**Figure 4.3: Scanning electron micrographs of the electrospun fiber mats obtained from solutions of PA-6-24 (A), PA-6-27 (B), PA-6-32 (C) PA-6-36 (D) in 1:1 FA:AA.**

The SEM image of the PA-6/ZnTCPPc-GdNP-conj (**4**) fiber is shown in Figure 4.4, revealing that there is a slight increase in fiber diameter as compared to the Pc alone (PA-6/ZnTCPPc). The fiber formed using the Pc-NP conjugate (**4**) conjugate was found to further increase the fiber diameter as expected. The conjugate is a more bulky sample than the Pc alone and is expected to increase the viscosity of the overall polymer solution. Analysis of the SEM images of the PA-6/Pc-NP mix (**5**) resulted in a further increase. The fiber diameters of the electrospun fibers were found

to range from 200 - 1050 nm (0.2-1.05  $\mu\text{m}$ ). The fibers of Pc-NP mix (5) were shown to have a number of beads (circled), Figure 4.4 (C).

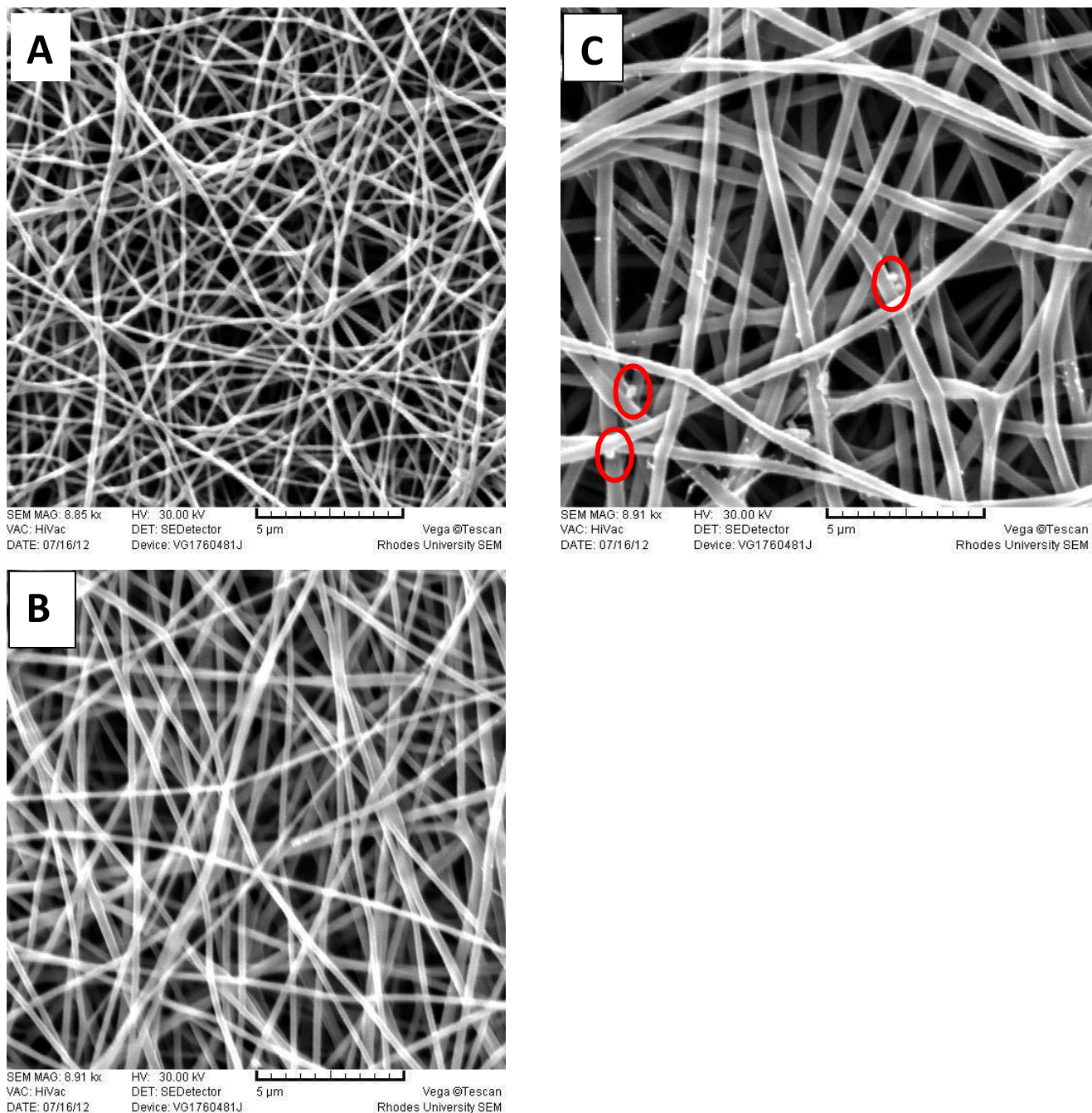


**Figure 4.4:** SEM images of the nanofibers mats of A) PA-6/ZnTCPPc, B) PA-6/ZnTCPPc-SiGd<sub>2</sub>O<sub>3</sub> NPs (conj) (4) and C) PA-6/ZnTCPPc-SiGdNPs (5,mix).

## 4.2.2 Spectroscopic characterization

### 4.2.2.1 EDX spectroscopy

Energy-dispersive X-ray spectroscopy (EDX) is an analytical technique employed for the analysis of elements or chemical characterization of a sample on metal surfaces.

The EDX spectra shown in Figure 4.5 confirm that the ZnTCPPc-SiGd<sub>2</sub>O<sub>3</sub>NP were successfully embedded in the PA-6 nanofibers as seen by the presence of the gadolinium and the zinc constituents. Firstly it reveals the gadolinium (Gd) composition of the nanoparticles. The carbon and the oxygen (O) observed are due to the PEG that was used during the synthetic procedure, having been used to incur stability for the nanoparticles. Upon forming the silica coat, Silica (Si) is observed in Figure 4.5 a) which confirms the successful coating of the gadolinium oxide nanoparticles. The Gd and Si matched the results obtained by Rossinyol *et al.* [9]. The elemental composition of ZnTCPPc was also confirmed by the presence of Nitrogen (N), Carbon (C) and O in Figure 4.5 b) and also observed in Figure 4.5d) for the mixture. No impurities were observed from this analysis; the aluminium observed is from the foil used as a collector for the nanofibers.

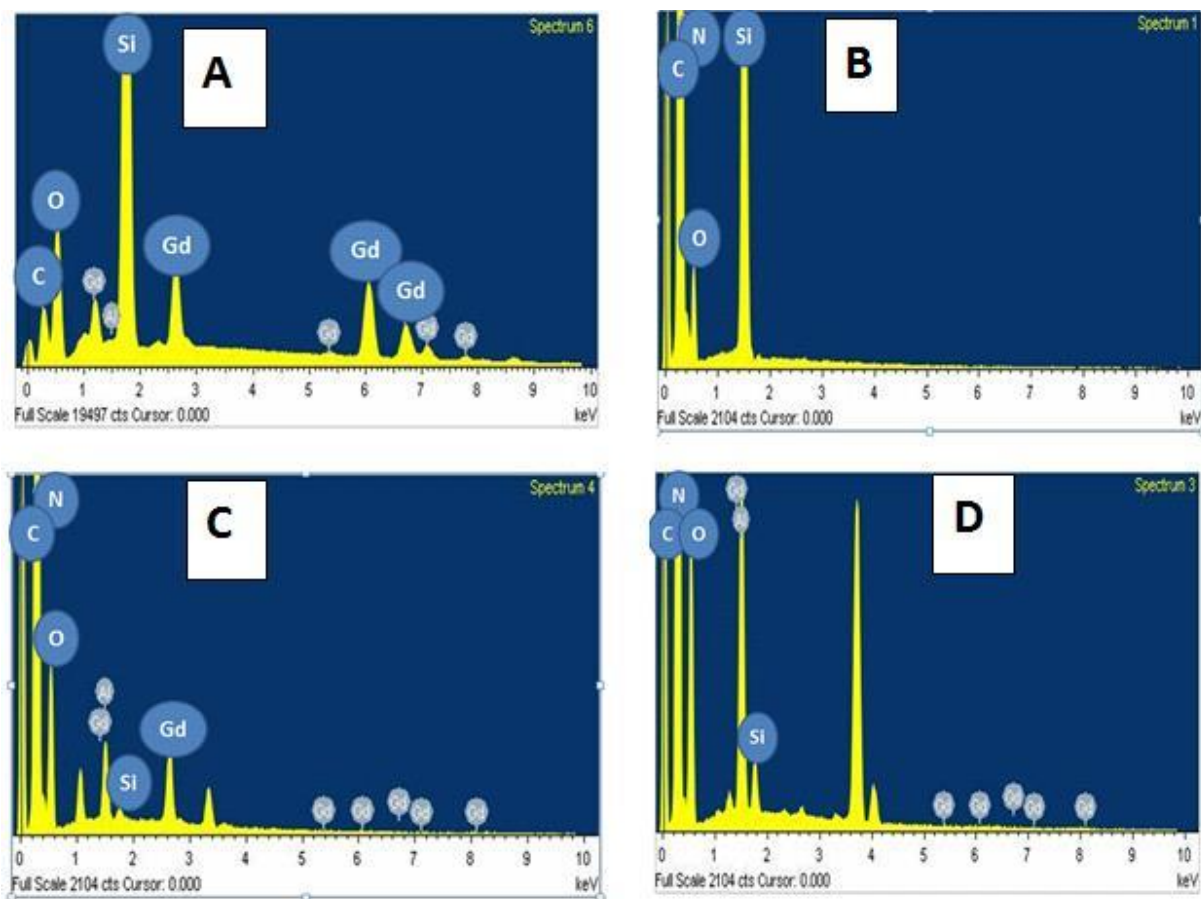


Figure 4.5: EDX spectrum of a) PA-6/Si-Gd<sub>2</sub>O<sub>3</sub> NP (conjugate) b) PA-6/ZnTCPPc c) PA-6/ZnTCPPc-SiGd<sub>2</sub>O<sub>3</sub>NPs (conjugate) and d) PA-6/ZnTCPPc-SiGd<sub>2</sub>O<sub>3</sub>NPs(mix) nanofibers proving the presence of the gadolinium oxide nanoparticles on the fibre.

### 4.3 Photochemical behaviour of the Pc functionalized fibers: singlet oxygen generating ability

Singlet oxygen plays a significant role in photocatalytic reactions. Therefore it is essential to determine the singlet oxygen generating ability of the modified fiber in the aqueous medium which is to be employed for photocatalysis. Similar work has been done, however with a different central metal, using a lutetium carboxyphenoxy phthalocyanine (with no nanoparticles).



The results showed that there was evidence of photo-conversion of the ADMA due to singlet oxygen production of the phthalocyanine within the fiber matrix, though long periods (75 min at 100 W) of irradiation were required. The value of the singlet oxygen quantum yield was estimated to be 0.11. Although the yield was low, which was as expected for aqueous media, since water quenches singlet oxygen [10], the value is still significant in showing the singlet oxygen generating ability of the modified fiber [11].

In this work the singlet oxygen quantum yield ( $\Phi_{\Delta}$ ) determinations for the ZnTCPPc and ZnTCPPc-SiGd<sub>2</sub>O<sub>3</sub>NPs in fibers were carried out in aqueous media using ADMA as a quencher and its degradation was monitored at 380 nm, as shown in Figure 4.6. In each case 15 mg of the modified fibers was suspended in an aqueous solution of ADMA and irradiated for 30 mins at 60W using the photolysis set-up described in Scheme 2.3.

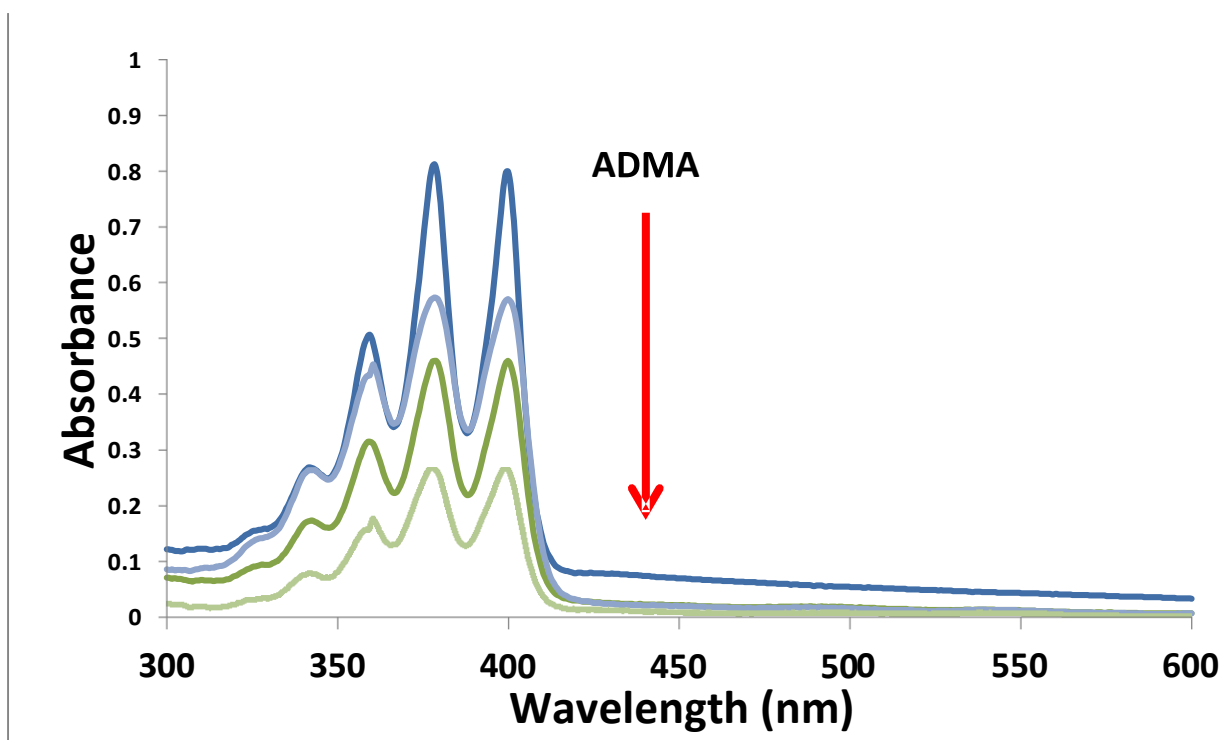


**Figure 4.6: UV-vis spectral changes observed upon photolysis of 15 mg of PA-6/ ZnTCPPc-nanofibers in the presence of ADMA in unbuffered water for 15 min of photolysis. Starting ADMA concentration =  $3.9 \times 10^{-5} \text{ mol dm}^{-3}$ , irradiation interval = 5 min.**

The singlet oxygen quantum yields obtained for the nanocomposite embedded in **fiber** are listed in Table 4.3. The absence of the Q-band of the phthalocyanine when using PA-6/ZnTCPPc and PA-6/ZnTCPPc-SiGd<sub>2</sub>O<sub>3</sub>NP nanofibers indicates that there was no leaching of the Pc into the water during singlet generation since they are not soluble in water. As observed there was a decrease in singlet oxygen quantum yield after conjugation and an increase after physical mixing. The higher the  $\Phi_{\Delta}$  value, the more effective the fiber for the degradation of Orange-G as will be observed in chapter 5. It was evident that the Pc is required for the generation of singlet oxygen, as the fiber alone, under the same conditions, did not produce any singlet oxygen as observed by the lack of degradation of ADMA. Due to a paucity of sample of the ZnTCPPc, ZnTCPPc-SiGd<sub>2</sub>O<sub>3</sub>NP (conjugate and mixed), studies of singlet oxygen generation without the fiber in water (using ADMA) were not determined. However comparing the results obtained from the studies using DPBF in DMSO, it was observed that there was a decrease in singlet oxygen generation when embedded in the fiber (bearing in mind that singlet oxygen quantum yields are generally lower in water than in

organic solvents). This was, however, expected, since water is known to quench singlet oxygen [12]. Regardless of the reduced singlet quantum yields, the nanocomposites in fiber were found to be efficient singlet oxygen generators and they were able to produce enough singlet oxygen to degrade ADMA.

**Table 4.3: The effect of functionalization on singlet oxygen quantum yields. Polymer formed from PA-6 (B 32, 14 wt. %) 3:1 (FA:AA).**

<b>Complex</b>	<b>Fiber Diameter(<math>\mu\text{m}</math>)</b>	<b><math>\Phi_{\Delta}</math> (in water)</b>
<b>PA-6/ZnTCPPc</b>	225	0.16
<b>PA-6/ZnTCPPc-SiGd<sub>2</sub>O<sub>3</sub>NP (conjugate)</b>	575	0.12
<b>PA-6/ZnTCPPc- SiGd<sub>2</sub>O<sub>3</sub>NP (mix)</b>	1025	0.21

## 4.4 References

1. B. Decostere, N. Daels, S. De Vrieze, P. Dejans, T. Van Camp, W. Audenaert, J. Hogie, P. Westbroek, K. De Clerck, S. W. H. Van Hull, *Desalination*, 249 (2009)250.
2. M. M. Bergahoef, G. J. Vansco, *Adv. Mater.*, 11, (1999) 1362.
3. S. Honarbakhsh, B. Pourdeyhimi, *J. Mater. Sci.*, 46, (2011) 2874.
4. C. Xu, F. Xu, B. Wang, T. J. Lu, *J. Nanomater.*, , 2011, (2011) 201834.
5. Z-M. Huang, Y-Z. Zhang, M. Kotaki, S. Ramakrishna. *Comp Sci & Tech*, , 63, (2003) 2223
6. B. De Schoenmaker, L. Van Der Schueren, S. De Vrieze, P. Westbroek, K. De Clerck, *J. Appl. Polym. Sci.*, 120 (2011) 305.
7. [http://www.orioninstrument.com/whtml/dielectric\\_constants.asp](http://www.orioninstrument.com/whtml/dielectric_constants.asp).
8. B. Agboola, K.I. Ozoemena, T. Nyokong, *J. Mol. Catal. A: Chem.*, 248 (2006)84
9. E. Rossinyol, E. Pellicer, A. Prim, S. Estrade, J. Arbiol, F. Peiro, A. Cornet, J. R. Morante, Gadolinium doped Ceria nanocrystals synthesised from mesoporous silica, 10 (2008) 369.
10. N. B. McKeown and J. Painter, *J. Mater. Chem.*, (1994) 1153.
11. R. Zuggle, C. Litwinski, N. Torto, T. Nyokong, Photophysical and photochemical behaviour of electrospun fibers of a polyurethane polymer chemically linked to lutetium caorboxyphenoxy phthalocyanine., 35 (2011)1588.
12. A. Ogunsipe, J.Y. Chen and T. Nyokong. *New J. Chem.*, 28 (2004) 822

# **Chapter 5**

## **Photodegradation of azo dye pollutants**

This chapter reports on the application of Pc and Pc-Gd<sub>2</sub>O<sub>3</sub>NPs functionalized fibers as photocatalysts in the photodegradation of the organic pollutant Orange G.

## 5.1 Introduction

The widespread presence of organic dyes in industrial wastewater has been proven to be a potentially highly serious environmental problem. Azo dyes for example Orange G (OG), especially, are non-biodegradable, toxic and potentially carcinogenic in nature, and are widely used in industries as food colouring, chemical indicators and for many other applications[1]. In the past, various physico-chemical and biological methods were used to remove colour from dye containing wastewaters. These techniques included for example: filtration, coagulation, precipitation, adsorption, ion exchange and classical oxidation techniques [2]. However, there was lack of success because of the pollution transfer from one phase to another leading therefore to a further costly treatment being observed [3]. A promising approach, based on the production of singlet oxygen generated by phthalocyanines under photoradiation which lead to photodegradation of the dye [4], has been developed. The photocatalytic degradation of OG has been reported in several studies [5], however, not with the conjugate/composite as reported in this work (i.e. Pc-Gd<sub>2</sub>O<sub>3</sub> NP).

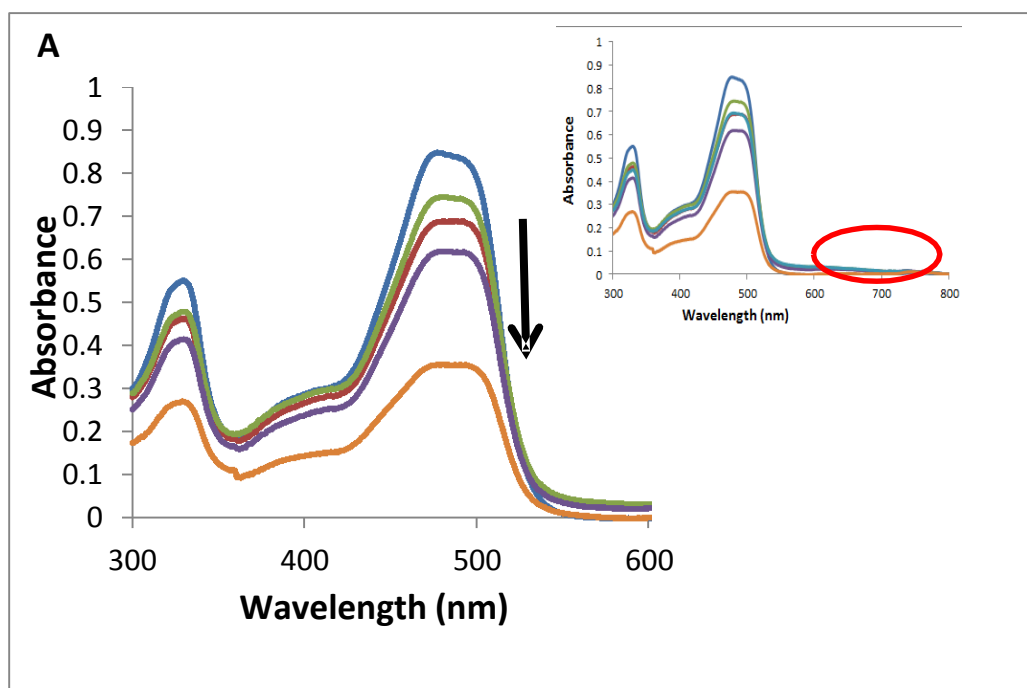
## 5.2. Photodegradation of Orange G (OG)

### 5.2.1. Spectroscopic characterization

Not surprisingly, the unmodified fiber on its own showed no activity toward the photodegradation of OG. This also confirms that the photosensitizer ZnTCPPc is embedded in the fiber mat, hence catalytic activity is observed.

The absence of the Q-band of the phthalocyanine indicates that there was no leaching of the Pc into the water as shown in Figure 5.1A. All experiments were performed by placing 5 g fibre pieces in 5 ml deionised water in a glass vial. The photocatalytic setup used was the same as that used for singlet oxygen detection, Scheme 2.3. The light reaching the reaction vessel was found to be  $3.2 \times 10^{20}$  photons  $\text{cm}^{-2} \cdot \text{s}^{-1}$ . The degradation was monitored by observing the change in the absorbance band of orange G at 478 nm [6]. An advantage for this photocatalytic system is that the used fiber could simply be removed from solution following

photolysis, using a pair of tweezers or with magnet for the fibers embedded magnetic nanoparticles. Figure 5.1 shows the absorption spectral changes observed during the photolysis of Orange-G at 5 min intervals using PA-6/ZnTCPPc (Figure 5.1A), PA-6/ZnTCPPc-Si-Gd<sub>2</sub>O<sub>3</sub>NP (conjugate) (Figure 5.1B) and PA-6/ZnTCPPc-SiGd<sub>2</sub>O<sub>3</sub>NP (mix) nanofibers (Figure 5.1C) as a photocatalyst. The spectral changes observed for PA-6/ZnTCPPc without Si-GdNP showed a smaller decrease in the Orange G band. The OG absorption peak at 478 nm shows a greater decrease in intensity in the presence of PA-6/ZnTPCPC- Si-Gd<sub>2</sub>O<sub>3</sub>NP (Figure 5.2). This decrease can be attributed to the large singlet oxygen quantum yield observed for the conjugate and the mix. With the mix having the greatest singlet oxygen quantum yield, it is expected to be show better catalytic behaviour for the degradation of orange G.



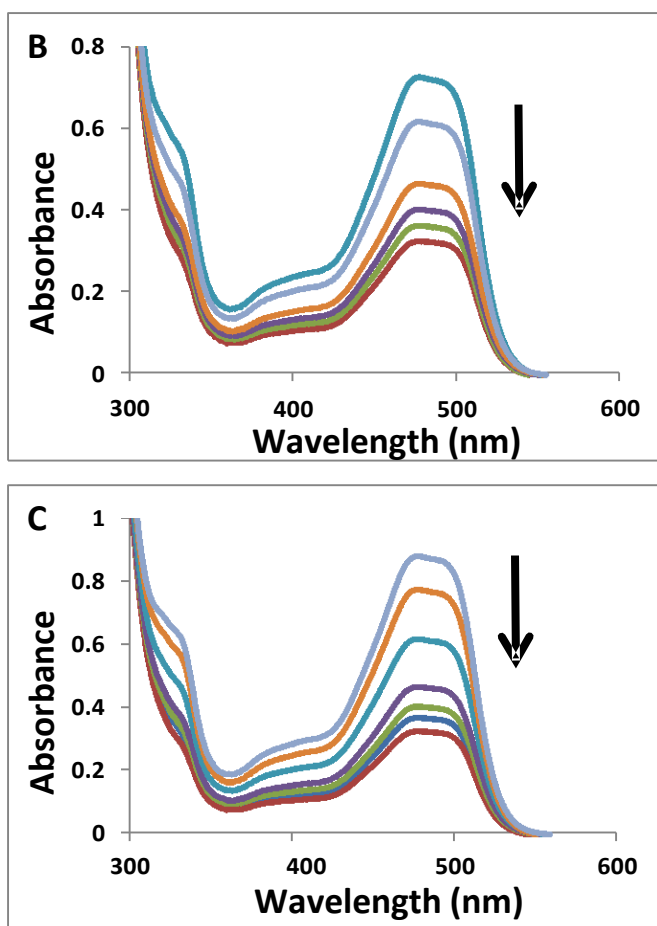


**Figure 5.1** Electronic absorption spectral changes of a  $1.93 \times 10^{-5} \text{ mol L}^{-1}$  Orange G solution during visible light photocatalysis using a 10 mg A) ZnTCPPc , B) ZnTCPPc-SiGd<sub>2</sub>O<sub>3</sub>NP (conjugate) and C) ZnTCPPc-SiGd<sub>2</sub>O<sub>3</sub>NP (mix) nanofiber mat. The experiments were carried out using unbuffered water and the spectra recorded at 5 min intervals.

### 5.2.2. Kinetics studies for the photodegradation of Orange-G (OG)

The plots of  $\ln(C_0/C)$  versus irradiation time are shown in Figure 5.2. The linearity of the plots obtained indicates that this reaction follows first order kinetics. The kinetic data is listed in Table 5.1.



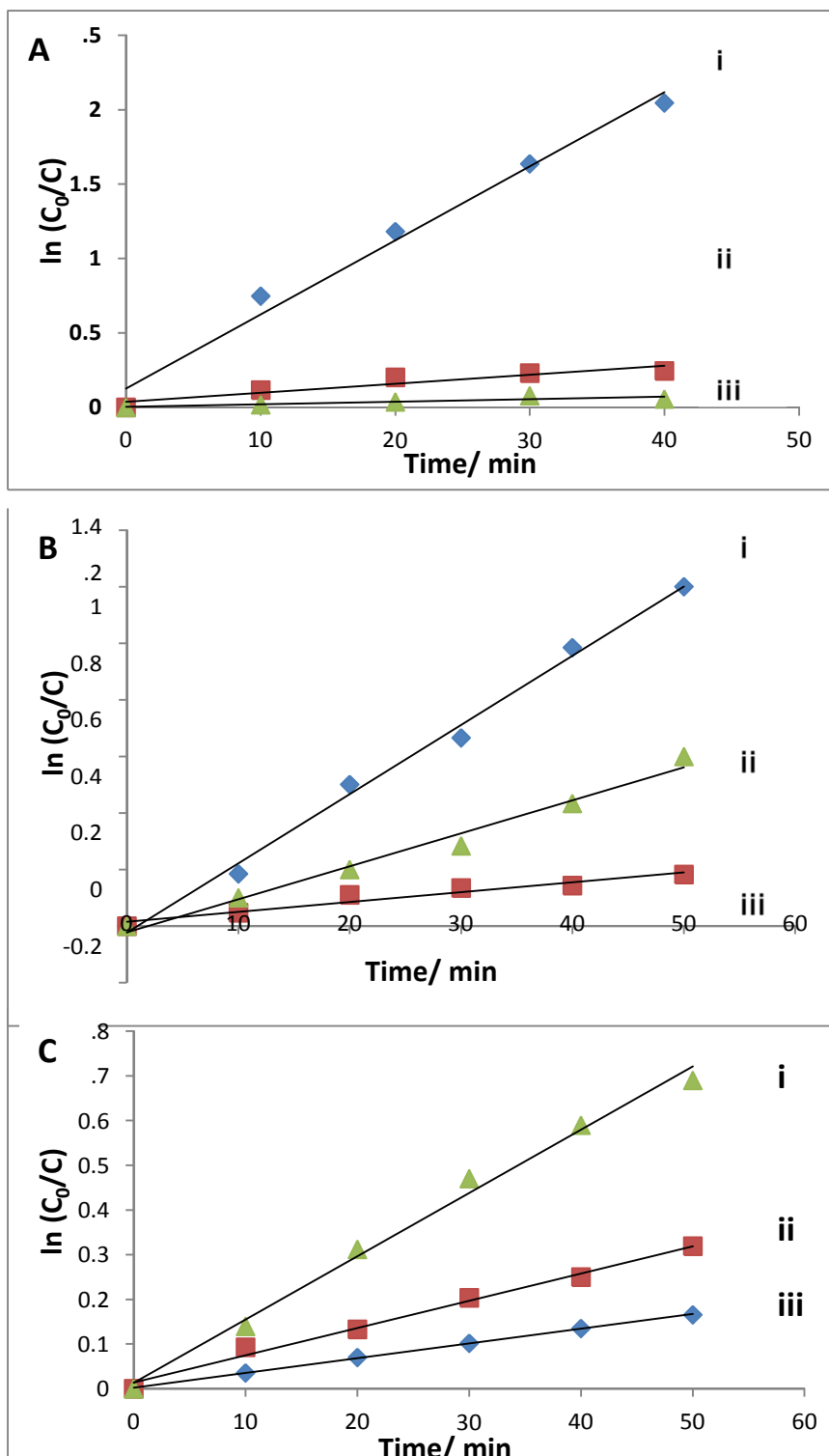


Figure 5.2: First order kinetics plots for the degradation of OG for: (A) PA-6/ ZnTCPPc  $R^2$ : 0.984, 0.882 and 0.780 for (i), (ii), and (iii) respectively (B) PA-6/ ZnTCPPc-SiGd<sub>2</sub>O<sub>3</sub>(conjugate)  $R^2$ : 0.994, 0.982 and 0.944 for (i), (ii), and (iii) respectively and (C) PA-6/ ZnTCPPc-SiGd<sub>2</sub>O<sub>3</sub> (mix)  $R^2$ : 0.992, 0.990 and 0.999 for (i), (ii), and (iii) respectively, nanofiber as a photocatalysts.

OG Concentration: (i)  $2.3 \times 10^{-5}$ , (ii)  $3.5 \times 10^{-5}$  and (iii)  $4.8 \times 10^{-5}$  mol L<sup>-1</sup>

The rate of photodegradation of OG decreased with an increase in OG concentration, where the rate is faster for PA-6/ZnTCPPc-SiGd<sub>2</sub>O<sub>3</sub>NP nanofibers compared to PA-6/ZnTCPPc nanofibers without the nanoparticles. This is due to the higher singlet oxygen quantum yield obtained for nylon-6/ ZnTCPPc-SiGd<sub>2</sub>O<sub>3</sub>NP nanofibers. A decrease in  $K_{obs}$  was observed as the concentration of the orange G increased. Higher  $K_{obs}$  values were obtained for the conjugate and the mix compared to those obtained for the Pc alone. This observation can be explained by the increase in the singlet oxygen generation for the conjugate and the mix. The reduced half-lives for OG oxidation for the ZnTCPPc-SiGd<sub>2</sub>O<sub>3</sub>NP nanofiber compared to ZnTCPPc nanofiber, Table 5.1, shows that the MNPs in the former improve the efficiency of the OG photodegradation due to increased singlet oxygen quantum yields. The rate for OG degradation is slower when ZnTCPPc or ZnTCPPc- SiGd<sub>2</sub>O<sub>3</sub>NP are employed in solution (not embedded in fiber) Table 5.1, although the amounts of the Pc in solution and fiber are different. The  $K_{obs}$  values for the ZnTCPPc in solution are smaller than those observed for ZnTCPPc in fiber. This was observed also for ZnTCPPc-SiGd<sub>2</sub>O<sub>3</sub>NP-conjugate and ZnTCPPc-SiGd<sub>2</sub>O<sub>3</sub>NP-mix. Also the half-lives for ZnTCPPc in solution were much greater than those observed for ZnTCPPc in fiber; again the same pattern is seen for ZnTCPPc-SiGd<sub>2</sub>O<sub>3</sub>NP-conjugate and ZnTCPPc-SiGd<sub>2</sub>O<sub>3</sub>NP-mix. Therefore this shows that photocatalysis is more efficient in functionalised nanofibers.

Table 5.1: The initial rate, rate constant ( $k_{obs}$ ) and half-life ( $t_{1/2}$ ) of various initial concentrations of Orange G using the variously functionalized electrospun fibers.

Values in brackets are for nanocomposites not embedded in fiber.

Catalyst	[OG] ( $\times 10^{-5}$ mol L $^{-1}$ )	$k_{obs}$ (min $^{-1}$ )	Initial rate (mol L $^{-1}$ min $^{-1}$ )	Half-life (min)
PA-6/ZnTCPPc (2 mmol)	2.3	0.014(0.0080)	$3.2 \times 10^{-7}$ ( $1.8 \times 10^{-7}$ )	49 (87)
	3.5	0.0060(0.0058)	$2.1 \times 10^{-7}$ ( $2.0 \times 10^{-7}$ )	116 (119)
	4.8	0.0033(0.0010)	$1.6 \times 10^{-7}$ ( $4.8 \times 10^{-8}$ )	210 (693)
PA-6/ZnTCPPc - Conjugate (2 mmol)	2.3	0.050(0.030)	$1.2 \times 10^{-6}$ ( $6.9 \times 10^{-7}$ )	14 (25)
	3.5	0.016 (0.010)	$5.6 \times 10^{-7}$ ( $3.5 \times 10^{-7}$ )	44 (69)
	4.8	0.0036(0.0020)	$1.7 \times 10^{-7}$ ( $9.6 \times 10^{-8}$ )	193(347)
PA-6/ZnTCPPc-mix (2 mmol)	2.3	0.019	$4.4 \times 10^{-7}$	36
	3.5	0.018	$6.3 \times 10^{-7}$	39
	4.8	0.018	$8.4 \times 10^{-7}$	39

### 5.3 Conclusion

The phthalocyanine and phthalocyanine-gadolinium oxide nanoparticle conjugate nanofibers were found to be photoactive and are promising photosensitizers for the conversion of the environmental pollutant, Orange G. The conjugate and the mix nanocomposites showed an increase in singlet oxygen quantum yield resulting in an increase in the rate of photodegradation. Nanocomposites embedded on fibers were found to be more efficient in degrading orange G than those not in fibers. This proves that functionalised nanofibers are better photocatalysts.

## 5.4 References

1. Stylidi M., Kondarides D. I., Verykios X.E., *Appl. Catal.* 1347, (2004)189.
2. Aplin R., Wait T. D., *Water Sci. Technol*, 42, (2000) 345.
3. Neppalian B., Choi H. C., Sakhivel S., Banunathi A. and Murugaan V. *Chemosphere*. 46, (2002) 1173.
4. Sun J., Wang X., Sun J., Sun S., Qiao L., *J Mol. Catal. A: chem.*, 265 (2007) 133.
5. W. Spiller, H. Kliesch, D. Wöhrle, S. Hackbarth, B. Röder, G.J. Schnurpfeil *J. Porphyrins Phthalocyanines*, 2 (1998) 145.
6. J. Deng, J. Jiang, Y. Zhang, X. Lin, C. Du, Y. Xiong, *Appl. Catal B.*, 84, (2006) 468.

# Chapter 6

## 6 General Conclusions

Zinc tetracarboxyphenoxy phthalocyanine (ZnTCPPc, **3**) was covalently attached to the surface of an amino functionalized silica-coated gadolinium oxide (Si-Gd<sub>2</sub>O<sub>3</sub>, **2**) nanoparticle through formation of an amide bond. Formation of the covalent link between the Si-Gd<sub>2</sub>O<sub>3</sub> NPs and ZnTCPPc to form the conjugate (**4**) was confirmed using FTIR spectroscopy. Spherical gadolinium oxide nanoparticles were synthesized as confirmed with TEM. TEM also revealed an increase in size after coating the surface of the nanoparticles with silica and furthermore after conjugation. Sizes for the nanoparticles obtained were from TEM studies. XPS studies clearly revealed the presence of the characteristic Gd peaks and further showed that the silica coating step had completely capped the NP, as no Gd peaks are observed. A steady rise from 600 to 400 nm was observed for the conjugate upon conjugation of the Pc to the nanoparticle, confirming the presence of the nanoparticle after conjugation. The ground state absorption, fluorescence excitation and emission spectra of ZnTCPPc after mixing with, and linking to, Si-Gd<sub>2</sub>O<sub>3</sub>NPs did not change significantly. The fluorescence quantum yields decreased in the presence of the nanoparticles.  $\Phi_{\Delta}$  and  $\tau_T$  of ZnTCPPc were found to increase upon conjugation.

The zinc phthalocyanines and the gadolinium oxide nanoparticle conjugates were successfully incorporated into electrospun polymer fibers and the photochemical and photophysical parameters evaluated. Improved singlet oxygen quantum yields were obtained for the fibers as compared to the Pc (**3**) and the conjugate (**4**) alone. The model pollutant Orange-G was easily degraded by these photocatalysts and the rate was high for PA-6/ZnTCPPC-Si-Gd<sub>2</sub>O<sub>3</sub>NP (mix) fiber due to its improved singlet oxygen quantum yield. These polymeric fiber materials, incorporating phthalocyanine and phthalocyanine-gadolinium oxide nanoparticle conjugates, were shown to be promising materials in developing multi-functional nanomaterials, which are easily recoverable, for application in photocatalysis.